Dynamics of liquid-liquid phase separation in protein solutions probed by coherent X-ray scattering
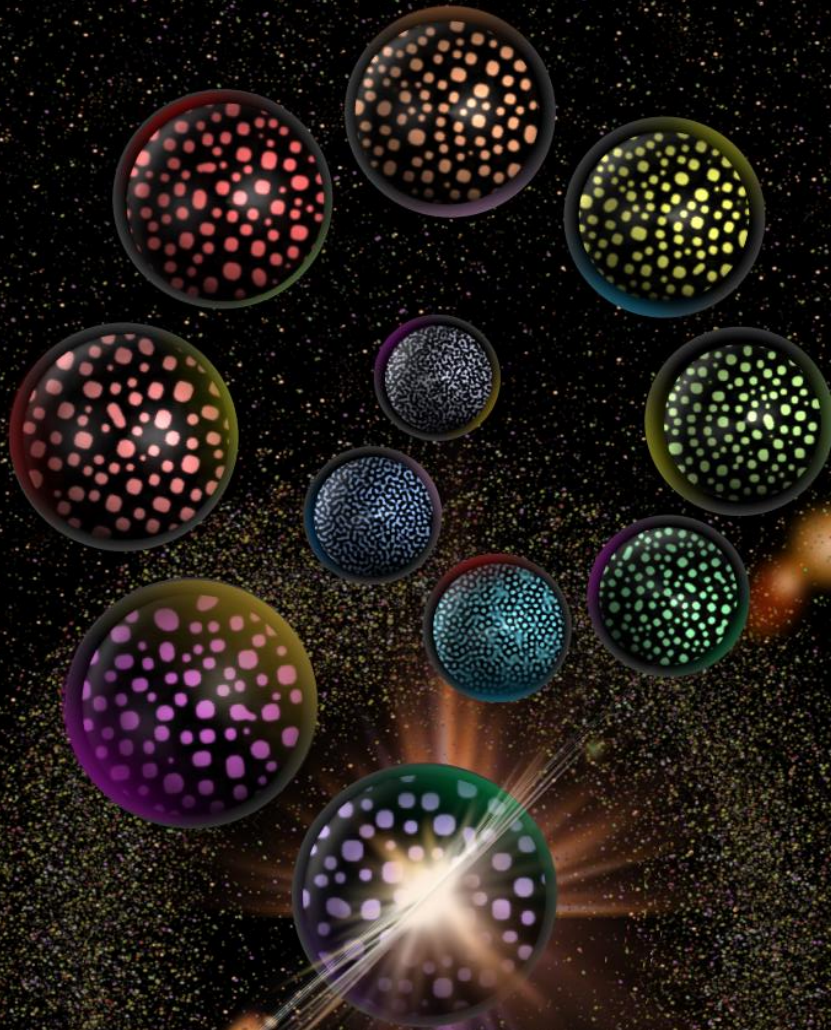
Anastasia Ragulskaya

Dynamics of liquid-liquid phase separation in protein solutions probed by coherent X-ray scattering

Dissertation

der Mathematisch-Naturwissenschaftlichen Fakultät

der Eberhard Karls Universität Tübingen

zur Erlangung des Grades eines

Doktors der Naturwissenschaften

(Dr. rer. nat.)

vorgelegt von

Anastasia Ragulskaya

aus Moskau, Russland

Tübingen

2022

Contents

Contents

Abstract

Understanding the fundamental process of liquid–liquid phase separation (LLPS) in biological systems is relevant to a range of diverse areas such as protein crystallization, bio-materials, self-organization of the biological cells, protein condensation-related diseases, and industrial food processing. LLPS is a complex process involving domain evolution of the new phases, microscopic dynamics of density fluctuation, the thermal fluctuation of domain interfaces, and global diffusive motion. This dynamics is strongly intertwined with the kinetics of structural evolution in the early stage of spinodal decomposition (SD) of LLPS. While both the kinetics of domain evolution and the microscopic dynamics are essential for the formation and properties of the various condensates, research so far has mainly focused on the domain growth kinetics. Meanwhile, the dynamics remain largely unknown due to the experimental difficulty in measuring slow dynamics on a micrometer length scale. X-ray photon correlation spectroscopy (XPCS) is a key technique that enables measurements at the corresponding scales. Moreover, it can simultaneously provide both information on the evolution of the structure as well as the dynamics. Nevertheless, until recently, such experiments were not carried out due to the radiation damage problem.

This thesis pursues two objectives. One is the study of the microscopic dynamics of LLPS in protein solutions probed by XPCS. The other is to advance the field of XPCS itself: from conducting an experiment on biological samples to interpreting data related to non-equilibrium dynamics. To achieve them, we first investigated the dynamics of the LLPS on the model system of BSA-YCl$_3$ by XPCS with the simultaneous study of growth kinetics by ultra-small angle X-ray scattering (USAXS). Then, to support the experimental results and extend some of the conclusions from phase separation of BSA-YCl$_3$ system to LLPS phenomena in general, Cahn-Hilliard (CH) simulations were performed.

In the first part of the results section, it is demonstrated that in the early stage of SD, the kinetics relaxation of BSA-YCl$_3$ is up to 40 times slower than the dy-

Abstract

namics and thus can be decoupled. The microscopic dynamics is well-described by hyper-diffusive ballistic motions with a relaxation time exponentially growing with time in the early stage, followed by a power-law increase with fluctuations. However, some unresolved issues remain. The classical analysis of XPCS data is insufficient to judge the presence of gelation in the studied sample. Additionally, the experimental results show rich side features in the two-time correlation map (TTC). The physics behind these features might be crucial for understanding the non-equilibrium dynamics; however, only the component along the diagonal is usually in focus, while the side features cannot be easily interpreted via classical analysis or simulation methods.

In the next chapter, we propose a Reverse-Engineering (RE) approach based on particle-based heuristic simulations that allows to predict and understand the kinetics and dynamics of systems undergoing non-equilibrium processes. This also addresses the issues that remained open in the previous section. For the microscopic length scale, the typical TTC for LLPS contains three characteristic features: "modulations" along the diagonal, a "square" feature, and "tails". It is demonstrated that the RE approach could go beyond CH theory and build the connection between these features in the TTC and the key parameters, such as relaxation time, concentration distribution, the size distribution of domains, viscosity, and mobility. Furthermore, using the RE approach, it is shown that the degree of visibility of a "square" feature is related to gelation. Based on this new result, as well as previous experimental confirmations, we can confirm the presence of gelation in the BSA-YCl$_3$ system at the investigated time scales identifying a nearby glass transition.

All of the results described so far are obtained during measurements near the end of the capillary. In the third results part, it is shown that the dynamics in the middle of the capillary is different. The corresponding changes in TTCs result in the appearance of a special "wing" feature. Based on the measurements supported by the simulations, it is demonstrated that the "wing" feature might result from the flow retraction caused by the volume change upon temperature jump. The shape of this feature is shown to contain information about the flow rates before and after the retraction. The state of the system at the time that the wing feature appears corresponds to a steady state with the minimum influence of flow. These effects of flow on dynamics do not influence the static structure factor.

Finally, new insights gained on the conditions to carry out bio-XPCS experiments are combined with the previous knowledge in this area to derive a sequence of steps for conducting an XPCS experiment on proteins. This optimized procedure is presented in the conclusions along with a summary of findings on the relationship between dynamics and features on TTCs.

In this thesis, we developed a comprehensive understanding of the procedure and data analysis of XPCS experiments on the protein systems, as well as microscopic dynamics and its interplay with the kinetics of LLPS. The results of this work and the established frameworks are relevant also for various soft-matter systems and phenomena essential for understanding the fundamentals of materials synthesis, processing, and phase transformation.

Abstract

Zusammenfassung in deutscher Sprache

Ein grundlegendes Verständnis der flüssig-flüssig-Phasentrennung (engl.: LLPS) in biologischen Systemen ist u.a. für die Kristallisation von Proteinen, mit Proteinkondensation verbundene Krankheiten, die Selbstorganisation biologischer Zellen und industrielle Lebensmittelverarbeitung von Bedeutung. LLPS ist ein komplexer Prozess, der die Domänenentwicklung der neuen Phasen, die mikroskopische Dynamik der Dichtefluktuation, die thermische Fluktuation der Domänengrenzflächen und die globale Diffusionsbewegung umfasst. Diese Dynamik ist eng mit der Kinetik der strukturellen Entwicklung in der frühen Phase der spinodalen Zersetzung (engl.: SD) der LLPS verwoben. Während sowohl die Kinetik der Domänenentwicklung als auch die mikroskopische Dynamik für die Bildung und die Eigenschaften der verschiedenen Kondensate von wesentlicher Bedeutung sind, hat sich die Forschung bisher hauptsächlich auf die Kinetik des Domänenwachstums konzentriert. Die Dynamik ist jedoch noch weitgehend unbekannt, da es schwierig ist, die langsame Dynamik auf einer Längenskala im Mikrometerbereich zu messen. Die Röntgenphotonen-Korrelationsspektroskopie (engl.: XPCS) ist eine entscheidende Technik, die Messungen auf den entsprechenden Skalen ermöglicht. Außerdem kann sie gleichzeitig Informationen über das strukturelle Wachstum und die sich entwickelnde Dynamik liefern. Bis vor kurzem wurden solche Experimente jedoch aufgrund der Strahlenschäden nicht durchgeführt.

In dieser Arbeit werden zwei Ziele verfolgt. Das Erste ist die Untersuchung der mikroskopischen Dynamik von LLPS in Proteinlösungen, die mit XPCS erforscht wird. Das Zweite besteht darin, das Gebiet der XPCS selbst voranzubringen: von der Durchführung eines Experiments an biologischen Proben bis hin zur Interpretation von Daten im Zusammenhang mit Nichtgleichgewichtsdynamiken. Um diese Ziele zu erreichen, wurde zunächst die Dynamik

der LLPS am Modellsystem BSA-YCl$_3$ mittels XPCS mit gleichzeitiger Untersuchung der Wachstumskinetik durch Ultrakleinwinkel-Röntgenstreuung (engl.: USAXS) untersucht. Um die experimentellen Ergebnisse zu untermauern und einige der Schlussfolgerungen von der Phasentrennung des BSA-YCl$_3$-Systems auf LLPS-Phänomene im Allgemeinen auszuweiten, wurden anschließend Cahn-Hilliard (CH)-Simulationen durchgeführt.

Im ersten Teil der Ergebnisse dieser Dissertation wurde gezeigt, dass die kinetische Relaxation von BSA-YCl$_3$ im Frühstadium der SD bis zu 40-mal langsamer ist als die Dynamik und daher entkoppelt werden kann. Die mikroskopische Dynamik konnte durch hyperdiffusive ballistische Bewegungen gut beschrieben werden, wobei die Relaxationszeit in der Anfangsphase exponentiell mit der Zeit ansteigt, gefolgt von einem potenzierten Anstieg bei Fluktuationen. Es sind jedoch einige Fragen offen geblieben. Die klassische Analyse der XPCS-Daten war nicht ausreichend, um das Vorhandensein einer Gelierung in der untersuchten Probe zu beurteilen. Darüber hinaus zeigten die experimentellen Ergebnisse zahlreiche Nebenmerkmale in der Zeit-Zeit-Korrelationsgrafik (engl.: TTC). Die Physik hinter diesen Merkmalen könnte für das Verständnis der Nichtgleichgewichtsdynamik von entscheidender Bedeutung sein. Allerdings steht in der Regel nur die Komponente entlang der Diagonale im Mittelpunkt, während die seitlichen Merkmale mit klassischen Analyse- oder Simulationsmethoden nicht leicht zu interpretieren sind.

Im nächsten Kapitel wird ein Reverse-Engineering (RE)-Ansatz vorgeschlagen, der auf partikelbasierten heuristischen Simulationen beruht und es ermöglicht, die Kinetik und Dynamik von Systemen, die Nichtgleichgewichtsprozessen unterliegen, vorherzusagen und zu verstehen. Auf der mikroskopischen Längenskala enthält die typische TTC für LLPS drei charakteristische Merkmale: "Modulationen" entlang der Diagonalen, "quadratische" Merkmale und "Schweife". Es wurde gezeigt, dass der RE-Ansatz über die CH-Theorie hinausgeht und die Verbindung zwischen diesen Merkmalen in der TTC und den Schlüsselparametern wie Relaxationszeit, Konzentrationsverteilung, Größenverteilung der Domänen, Viskosität und Mobilität herstellen kann. Außerdem wurde mit Hilfe des RE-Ansatzes gezeigt, dass der Grad der Sichtbarkeit eines "quadratischen" Merkmals mit der Gelierung zusammenhängt. Auf Grundlage dieses neuen Ergebnisses sowie früherer experimenteller Bestätigungen haben wir das Vorhandensein von Gelierung im BSA-YCl$_3$-System auf den

untersuchten Zeitskalen bestätigt und einen Glasübergang identifiziert.

Alle bisher beschriebenen Ergebnisse wurden in Messungen nahe des Endes der Kapillare erzielt. Im dritten Teil der Ergebnisse wird gezeigt, dass die Dynamik in der Mitte der Kapillare anders ist. Die entsprechenden Änderungen in den TTCs führen zum Auftreten eines speziellen "Flügelmerkmals". Auf Grundlage simulationsgestützter Messungen konnte gezeigt werden, dass die Flügelmerkmale von einem durch temperaturbedingte Volumenänderung verursachten Kontraktionsfluss stammen könnten. Es wurde gezeigt, dass die Form dieses Merkmals Informationen über die Strömungsgeschwindigkeiten vor und nach der Kontraktion enthält. Der Zustand des Systems zu dem Zeitpunkt, an dem das Flügelmerkmal auftritt, entspricht einem stationären Zustand mit minimalem Einfluss der Strömung. Diese Auswirkungen der Strömung auf die Dynamik haben keinen Einfluss auf den statischen Strukturfaktor.

Schließlich wurden die neu gewonnenen Erkenntnisse über die Durchführung von Bio-XPCS-Experimenten mit dem bisherigen Wissen auf diesem Gebiet kombiniert, um die nötigen Schritte zur Durchführung eines XPCS-Experiments an Proteinen abzuleiten. Dieses optimierte Verfahren wurde in den Schlussfolgerungen zusammen mit den Ergebnissen über die Beziehung zwischen Dynamik und Merkmalen der TTCs dargestellt. Daher haben wir in dieser Dissertation ein umfassendes Verständnis der Vorgehensweise und der Datenanalyse von XPCS-Experimenten an Proteinsystemen sowie der mikroskopischen Dynamik und ihrer Wechselwirkung mit der Kinetik der LLPS entwickelt. Die Ergebnisse dieser Arbeit und die geschaffenen Rahmenbedingungen gelten für verschiedene Systeme weicher Materie und Phänomene, die für das Verständnis der Grundlagen der Materialsynthese, -verarbeitung und -umwandlung von hoher Bedeutung sind.

(Korrekturleser: Ingrid Dax und Alessandro Greco)

Part I

Introduction

A crucial issue in cell science is how to organize the cellular space to empower control over complex biochemical responses in space and time [1, 2]. One of the possible solutions is the localization of reaction components by creating cell compartments or organelles, which are distinct chemical environments.

In addition to membrane-bound compartments, where separation is ensured by a physical barrier [3, 4], the cell is comprised of many membraneless organelles (MLOs), also known as biomolecular condensates [1]. Examples include nucleoli [5], germ granules, centrosomes [6], p-bodies [7], stress granules [7, 8] as well as Cajal bodies [9]. Why do they not mix with the surroundings, and what phenomena does the cell use to organize membraneless compartments? The answers remained elusive for many years. However, recent observations indicate that many non-membrane-bound compartments likely will have the properties of liquid drops and their formation is explained by the liquid-liquid phase separation phenomenon (LLPS) [1, 2, 10–13]. The LLPS in a cell can be modulated by the change in multivalent interactions caused by the modification of environmental factors (pH, salt), the concentration of key components and compositions, as well as mutations in key molecules [1, 13, 14].

The regular functions of MLOs [1, 13, 15–19] include the stress response, regulation of gene expressions, and signal transaction. They are also important for bacterial division and viral replication. The LLPS mediates the MLOs with distinct material properties, which are altered in case of aberrant LLPS (e.g., gelation) [10]. The material properties of MLOs are fundamental for their distinct cellular functions [20]. The aberrant phase transition leads to the dysfunction in the formation, maintenance, and clearance of MLOs. This results in pathological aggregation and may lead to many associated diseases [21, 22]: eye cataract [23], sickle cell anemia [24], cancer [25, 26] or neurological disorders like Alzheimer's and Parkinson's diseases [27, 28] and amyotrophic lateral sclerosis [29]. Thus, the evolution of the kinetics and dynamics of the LLPS relates to the material properties and function or dysfunction of MLOs. In the last decade, around 3000 scientific articles have contributed to the pathological importance of LLPS [16].

Along with the formation of MLOs, phase separation is now considered as an underlying phenomenon in various biological processes like nucleocytoplasmic transport [30], the heterochromatin formation [31], processes in the origin and evolution of life [2, 32, 33], and many others, the list of which is growing rapidly

[9, 11, 15, 17, 34–37]. Thus, the investigation of LLPS in biological systems is of great importance for pharmacy [38], food industry [39], biomaterials [40], and protein crystallization [41].

It was shown that addition and subsequent change of concentration of multivalent ions are very efficient in tuning protein-protein interactions [42, 43] and result in rich phase diagrams that feature a re-entrant condensation phase behavior. The salt concentration can be used as the control parameter of protein phase diagrams, simplifying the achievement of LLPS for experiments under lab conditions for many protein solutions. For this thesis, bovine serum albumin (BSA) with YCl_3 in concentrated aqueous solution [44] is used as the model system.

LLPS is a complex process involving domain evolution of the new phases, microscopic dynamics of density fluctuation, and the thermal fluctuation of domain interfaces, as well as global diffusive motion. While both the kinetics of domain evolution and the microscopic dynamics are important for the formation and properties of the various condensates, research so far mainly focused on the domain growth kinetics [45–52] and the dynamics remains largely unknown. The information on the dynamics of LLPS is incomplete due to experimental difficulties in measuring slow dynamics on a micrometer length scale.

This dynamics displays rich non-equilibrium behavior on the length scales ranging from micrometer to single-protein size on the time scale from hundred seconds down to microseconds [46, 52, 53]. These scales are impossible to achieve simultaneously with standard techniques, such as Inelastic Neutron Scattering (INS), Inelastic X-ray Scattering (IXS), Spin-Echo, and others [54]. Dynamic Light Scattering (DLS) can be used for this range, but it misses the spatial resolution and is plagued by multiple scattering in dense and opaque solutions [55]. The high brilliance of third-generation light sources has made it possible to carry out X-ray photon correlation spectroscopy (XPCS) experiments. This enables the investigation of dynamics with time scales ranging from microseconds to thousands of seconds and length scales ranging from microns down to nanometers which is consisting of the time/length scales window that is important in the protein studies [54]. XPCS has been used in different soft condensed matter research areas for studying the dynamics of colloids [56], liquids [57], polymers [58] and clays [59]. However, due to experimental difficulties in working with beam-sensitive samples [60–62], only initial steps were made for

the investigation of protein systems with XPCS [63, 64].

The following more detailed introduction of this thesis consists of two chapters. Chapter 1 focuses on the general description of the physics of the LLPS phenomenon and its formalization with the Cahn-Hilliard equation (Section 1.3). It also provides information on the BSA-YCl$_3$ system (Section 1.4.2). While Chapter 2 discusses the fundamentals of X-ray scattering techniques for study of kinetics (USAXS, Section 2.2) and dynamics (XPCS, Section 2.4). Furthermore, the radiation damage issue is addressed, which is crucial for biological samples (Section 2.5). At the end of the chapter, the realization of low dose XPCS experiments is discussed in Section 2.5.2.

Chapter 1

Liquid-liquid phase separation

1.1 Inter-particle interactions in bulk solutions

A good approach to describe an interaction potential (V_{pp}) between two charged biological macromolecules (e.g., proteins) is Derjaguin–Landau–Verwey–Overbeck (DLVO) theory [65–67]. According to this theory, V_{pp} is a combination of competing contributions: attractive van der Waals interaction [68] and electrostatic repulsion between two charged particles [65, 69]. Despite the simplicity of the model, it is successful in the description of the relations between phase diagrams and interactions ranges of different systems [70, 71]. A purely repulsive system has been shown to exhibit only the fluid-crystal coexistence [72]. Eventually, additional attractive interactions are introduced to explain other condensed phases [70]. Attraction leads to the appearance of a gas-liquid coexistence region, which is stable in case of long-range interactions and metastable with respect to the gas-crystal coexistence for short-ranged attraction [71].

The DLVO theory was originally derived for colloidal dispersions. It is in good agreement with the experimental observations on some solution of globular (essentially spherical) proteins and remains valid after the addition of salt in low concentrations [73, 74]. However, it is crucial to bear in mind that DLVO fails to account for higher salt concentrations, properties of the salt type used, hydrophobic repulsion, depletion interactions, and protein-specific processes [67, 73]. This is especially important for systems with multivalent salts. Their presence may induce novel effects, going far beyond the mean-field theory, e.g., counterion condensation and ion-ion correlations [75]. Nevertheless, in many cases, DLVO theory provides approximate theoretical predictions which are in good agreement with the experimental results [76, 77], while a complete description of the system may be not possible even with costly computer simulations.

Thus, the phase transition phenomena can be studied by utilizing intermolecular potentials or interactions. However, this approach may still be complex. Alternatively, it is possible to hold the description using classic thermodynamics.

1.2 Thermodynamics of phase transitions

1.2.1 Stability of the system

In this section, the correlation between the Helmholtz free energy density, F, and phase transitions is described using basic thermodynamics [78]. By definition:

$$F = U - TS,$$

where U is the internal energy and S is the entropy. A phase transition occurs when the phase becomes unstable. It is possible to show that this corresponds to the minimum of F. If the system is characterized by variables (T, V), its stability can be described by the Gibbs-Duhem stability criterion:

$$\Delta U + p\Delta V - T\Delta S \geq 0,$$

where p is the pressure, T is the temperature, V is the volume, and Δ corresponds to the virtual variations of the variable from equilibrium. With constant T and V, the stable phase is characterized by a minimum of potential F. The difference in the free energy in the vicinity of equilibrium can be expanded into a series:

$$\Delta F = \delta F + 1/2\delta^2 F + 1/3!\,\delta^3 F + ...$$

Here, terms $\delta F, \delta^2 F, \delta^3 F, ...$ are first-, second- and third-order differentials with respect to the state variables.

Thus, from the general description, we can distinguish the following situations:

- For $\delta F = 0$ and $\delta^2 F, \delta^3 F, ... > 0$ the equilibrium is **stable**.

- If $\delta F = 0$ and $\delta^2 F > 0$, but the condition $\Delta F > 0$ is violated for certain perturbations, the equilibrium is **metastable**. This case is possible when some higher-order differentials $\delta^3 F, ... < 0$.

- For $\delta^2 F < 0$ the equilibrium is **unstable**.

1.2.2 Free energy of a single-component system

How does the theory discussed above correlate with the phase diagram? To understand that, we first consider a single-component system.

The macroscopic thermodynamic parameters of pressure p, volume V, and temperature T describe the physical state of a phase. For example, for an ideal (noninteracting) gas, the equation of state is given by [79]:

$$p = k_B T \cdot \frac{N}{V},$$

where k_B is the Boltzmann constant, and N is the number of particles. In order to account for the long-range attraction and short-range repulsion, the ideal gas equation of state should be modified. The available volume is reduced by Nv_p, where v_p is the exclusion volume of the particles. The pressure is reduced by $\alpha \cdot (N/V)^2$, where α is the strength of the attractive long-range potential. The final equation of state is called the van der Waals equation and is defined by [79–81]:

$$p = k_B T \cdot \frac{N}{V - Nv_p} - \alpha \cdot \left(\frac{N}{V}\right)^2. \tag{1.1}$$

The Helmholz free energy of the system is related to the pressure via [82]:

$$F = - \int p \, dV. \tag{1.2}$$

Now, we can apply the understanding of the relation between the stability of the system and the free energy from the previous section. For $T > T_c = (8\alpha)/(27v_p k_B)$, where p is a unique function of V and the state is stable. Below T_c for a given pressure, the system is metastable or unstable. The system splits into two phases in the unstable region: liquid and gas. The metastable regions consist of an overexpanded liquid and a supersaturated vapor. If a sufficient disturbance occurs, these phases convert to the two-phase system [83]. In comparison to the unstable region, which is characterized by an immediate phase separation, the system has to overcome an energy barrier to achieve the phase separation in the metastable region [84]. The unstable region is confined by the spinodal line, while the metastable regions lie between the spinodal and binodal (solubility)

lines [78].

The van der Waals equation is one of the earliest and most straightforward approaches to describing phase separation. However, the downside of this simplicity is the impossibility of describing complex phase transitions such as LLPS. Thus, to describe a real system, a more sophisticated approach may be required, e.g., an investigation of the free energy of a binary mixture.

1.2.3 Free energy of a binary mixture

In contrast to a single-component system, the interactions in a multi-component system arise from chemically different species of particles. This section presents theoretical considerations of such a binary mixture containing two species of particles, A and B. Depending on their self- and cross-interactions at various temperatures, they can either be in a mixed or a demixed state. For example, let us consider an aqueous protein solution where protein and solvent molecules can be identified as A and B [85].

For simplification, it is assumed that the system is incompressible and the composition is conserved. The mole fraction c of component A is equal to $c = n_A/(n_A + n_B) = n_A/N_A$, while the mole fraction of component B is $(1-c) = n_B/N_A$. Here, n_A and n_B are numbers of particles of type A and B, respectively and N_A is the Avogadro's number equals to $N_A = 6.022 \cdot 10^{23}$ mol^{-1}.

The Helmholtz free energy difference upon mixing is:

$$\Delta F_{mix} = F_{mix} - F^0_{unmix} = \Delta U_{mix} - T\Delta S_{mix},$$

where, F_{mix} and F^0_{unmix} are the free energies of mixed and demixed state. ΔU_{mix} and ΔS_{mix} are the changes in internal energy and entropy upon mixing. According to the Boltzmann-Planck equation:

$$\Delta S_{mix} = k_B \ln W_{mix} - k_B \ln W^0.$$

Here, k_B is the Boltzmann constant. The number of ways the particle can be arranged before mixing and after random mixing is W^0 and W_{mix}, respectively. Before mixing, there is only one configuration as the particles are indistinguishable. This leads to $W^0 = 1$. W_{mix} can be calculated as a multinomial coefficient:
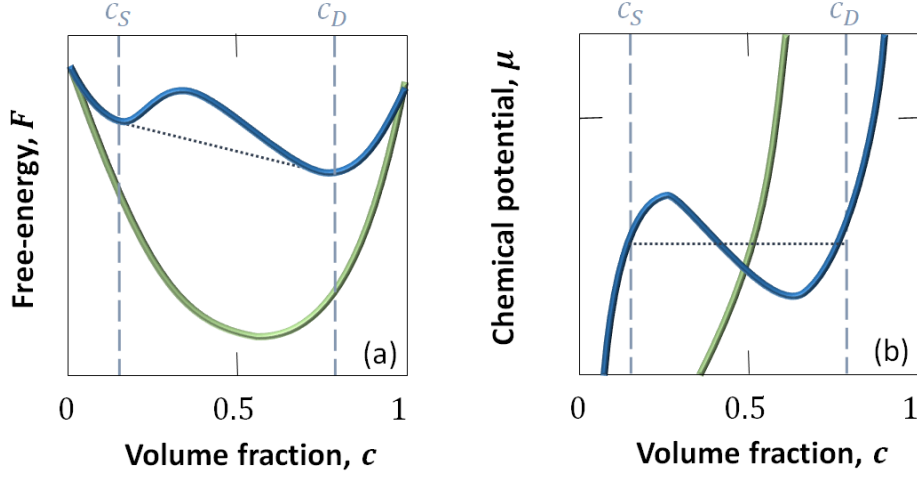
Figure 1.1: The Helmholz free energy F (a) and the corresponding chemical potential μ (b) as functions of volume fraction for different temperatures. Blue curves correspond to $T > T_c$. In this case, the demixing occurs in the interval $[c_S, c_D]$ with energy F^* of the demixed state indicated by the dotted line. The dashed vertical lines correspond to the equilibrium compositions of the stable phase-separated system [86]. In this case, the chemical potential is equal for two different compositions. Green curves correspond to $T < T_c$. The system is mixed, and each value of the chemical potential corresponds to a different composition.

$W_{\mathrm{mix}} = (N_A! / n_A! n_B!)$. Thus, applying Stirling's approximation:

$$\Delta S_{mix} = k_B \ln \frac{N_A!}{n_A! n_B!} \approx k_B \left(N_A \ln N_A - n_A \ln n_A - n_B \ln n_B \right) =$$

$$= -R[c \ln c + (1 - c) \ln(1 - c)],$$

where $R = k_B N_A$ is the universal gas constant. It is noted that for a given mixture ΔS_{mix} is always positive. If only one type of particles is present, the ΔS_{mix} becomes zero, since $c = 0$ (pure A) or $c = 1$ (pure B). The internal energy U_{mix} can be calculated as the pairwirse sum of interparticle potentials for each particle in the solution. For simplicity, only the interaction among the nearest neighboring atoms is considered. The self-interaction potentials are indicated as ϵ_{AA} and ϵ_{BB}, while the cross-interaction energy is ϵ_{AB}. Then, U can be expressed as:

$$U = P_{AA}\epsilon_{AA} + P_{BB}\epsilon_{BB} + P_{AB}\epsilon_{AB},$$

where, P_{AA}, P_{BB} and P_{AB} are the numbers of $A-A$, $B-B$, and $A-B$ interactions,

1.2.3. Free energy of a binary mixture

respectively. They can be expressed as:

$$P_{AA} = \frac{1}{2}\left(zn_A - P_{AB}\right) \text{ and } P_{BB} = \frac{1}{2}\left(zn_B - P_{AB}\right).$$

Here z is the number of nearest neighbors, and the $1/2$ factor is to avoid counting the pairwise interactions twice. Therefore, the internal energy of the mixed state can be written as:

$$U_{mix} = \left[\frac{zn_A}{2}\epsilon_{AA} + \frac{zn_B}{2}\epsilon_{BB}\right] + P_{AB}\left[\epsilon_{AB} - \frac{1}{2}\left(\epsilon_{AA} + \epsilon_{BB}\right)\right],$$

and the energy of the unmixed state as:

$$U^0_{\text{unmix}} = \left[\frac{zn_A}{2}\epsilon_{AA} + \frac{zn_B}{2}\epsilon_{BB}\right].$$

The expression of the number of cross interactions as a function of the mole fractions ($P_{AB} = zN_A c(1-c)$) leads to the following equation for the internal energy change upon mixing:

$$\Delta U_{mix} = U_{mix} - U^0_{\text{unmix}} = P_{AB}\left[\epsilon_{AB} - \frac{1}{2}\left(\epsilon_{AA} + \epsilon_{BB}\right)\right] = \Omega c(1-c).$$

$$\text{with } \Omega = zN_A\left[\epsilon_{AB} - \frac{1}{2}\left(\epsilon_{AA} + \epsilon_{BB}\right)\right].$$

Here, Ω is the regular solution constant. When the self-interaction overcomes the cross-interaction, Ω becomes positive. Considering both energetic and entropic contributions, we can express the Helmholtz free energy density per molecule as a function of T and c:

$$f(T, c) = \frac{\Delta F_{\text{mix}}}{N_A} = \frac{1}{N_A}\{\Omega c(1-c) + RT[c\ln c + (1-c)\ln(1-c)]\}. \qquad (1.3)$$

The investigation of Equation (1.3) enables predicting which state (mixed or demixed) will be thermodynamically favored under given conditions. The volume fraction dependence of the Helmholz free energy at different temperatures is presented in Figure 1.1 (a). For $T \geq T_c$, where $T_c = \Omega/2R$, the free energy is a convex function, which implies that the binary phase separation would

increase in free energy. Thus, the single-phase is stable against any compositional separation in the entire range of composition. However, at $T < T_c$, the free energy has a more complex shape - the area between the compositions is concave ($c = [c_S, c_D]$). When the free energy of a homogeneous solution is located in this part of the curve, any small composition fluctuation leads to lower free energy. Thus, the phase separation occurs, for which the compositions, c_S and c_D, are set by the local minima of the free energy, F^* (dotted line in Figure 1.1 (a)).

Why are these resulting phases stable? Usually, diffusive flux driven by chemical potential gradients compensates the concentration differences. In case of the described phase separation, the chemical potential is equal for two different compositions c_S and c_D (see Figure 1.1 (b)). Thus, there is no chemical potential difference across the phase boundaries. Nevertheless, there is diffusion across the boundary: equal numbers of molecules go in and out. Therefore, if there is a rise in the chemical potential of one phase (e.g., by synthesis or by chemical reactions), the diffusion into the other phase will compensate this and balance the chemical potential again [87].

The concentrations of the obtained phases have a temperature dependency. The values of c_S and c_D at different temperatures define the so-called LLPS binodal line as indicated in Figure 1.2. Under the binodal, the system is demixed. Outside the binodal, the system is in a stable single-phase regime.

1.2.4 Phase diagram and kinetic regimes

The previous section discussed the correlation between different behaviors of free energy and the phase states. The obtained results can be accumulated for the discussion of phase diagrams.

For a system with dominating short-range attractions in the temperature – concentration plane (e.g., proteins), only two stable phases exist, i.e., crystal and gas [90]. The phase diagram is shown in Figure 1.2 (a). The crystal and gas phases are defined by the solidus and solubility lines, respectively. The gas-crystal phase exists in between these lines. As a result, the phase diagram consists of four prominent phase boundaries: the liquid-liquid binodal, the glass line [91], the solidus line, and the solubility line. The area between the solubility line and the gas-crystal spinodal confines a metastable region, where the crystal and gas phases coexist. The metastable liquid-liquid phase separation region is

defined by the liquid-liquid binodal below the critical point. Therefore, below the spinodal, the phase separation is thermodynamically favorable, and the single-phased system separates into a dense and a dilute phase.

Based on the discussions about the shape of the $F(c)$ curves at different temperatures and a general description of the stability of the system, the distinction between different kinetic regimes of liquid-liquid phase separation can be anticipated (Figure 1.2(b)). As was shown previously, for $T < T_c$, $F(c)$ takes double-well form. Therefore, there is a sign change of the second derivative of c. For parts of the curve with $\frac{d^2F}{dc^2} < 0$, the system is fully unstable. There is no transient increase in the free energy when the system evolves to the two-phase state. This is a spinodal regime: in order to reach the equilibrium state, the amplitude of the non-local composition fluctuations increases. For systems located inside the spinodal, the phase separation starts immediately. The corresponding process is referred to as spinodal decomposition. For $\frac{d^2F}{dc^2} > 0$ the system is metastable. In this case, the phase separation requires a transient increase in the free energy and proceeds the nucleation and the growth of the minority phase [22, 84, 92]. The limit of the metastability is marked by $\frac{d^2F}{dc^2} = 0$. The temperature dependency of the corresponding concentrations is referred to as the LLPS spinodal line. In most of the actual phase separating systems, this line is not well-defined, which leads to a smooth transition between the nucleation and spinodal decomposition regimes [70, 93, 94]. At the critical point, the spinodal and the binodal lines meet. There, $T = T_c$ and $\frac{d^3F}{dc^3} = 0$ [84].

In the last decade, the interplay between the binodal and the glass transition has been a subject of intense research [45–47, 95]. It is reasonable to expect that the glass line may appear at sufficiently high volume fractions and inter-particle attraction. However, its relation with the binodal could interfere with the phase separation process. If the glass line crosses the binodal, it may slow down mobility. This leads to the interruption of the LLPS and ends up by creating an arrested state of the dense phase (Figure 1.2 (a)). This phenomenon is described in the literature as an arrested spinodal decomposition [50, 95–97].
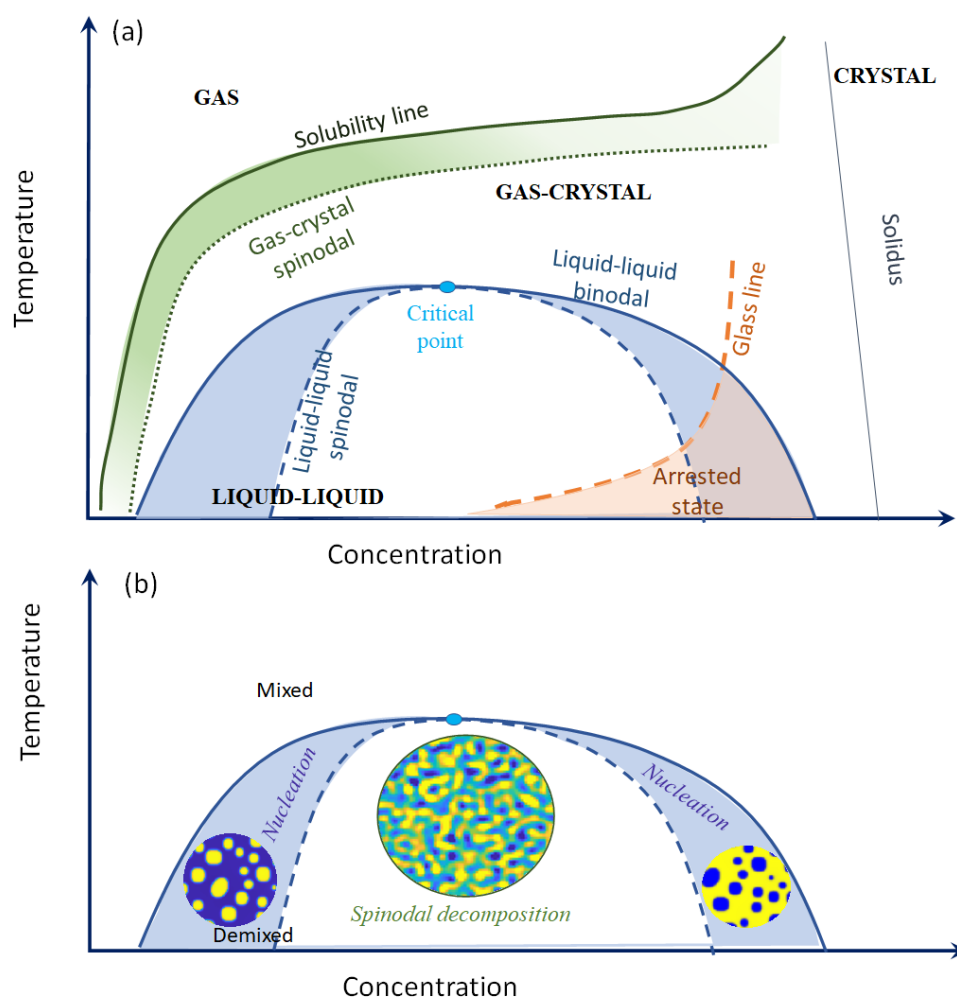
Figure 1.2: Protein phase diagrams: (a) in detail to describe different states and (b) only the liquid-liquid phase separation to describe different kinetic regimes. (a) The crystal and gas phases are defined by the solidus and solubility line, respectively, and, due to dominating attractive short-range forces, these are the only stable phases. The system is metastable below the liquid-liquid binodal and forms two liquid phases. Below the glass line, an arrested state is formed by the dense phase. (b) The spinodal decomposition forms the two phases below the liquid-liquid spinodal. If the system is located between the liquid-liquid binodal and spinodal, the kinetic regime is the nucleation. The system sketches in different kinetic regimes are shown in circles in the corresponding area of the phase diagram. (a) Modified from [88] and (b) from [89].

1.3 Spinodal decomposition and Cahn-Hilliard equation

The spinodal decomposition regime of LLPS can be described by the Cahn-Hilliard theory [98–100]. It answers the questions of how the composition field of the concentration $c(\vec{r}, t)$ evolves with time. This subsection discusses the classical Cahn-Hilliard theory.

1.3.1 The model

The purpose of the Cahn-Hilliard theory is to provide an equation of motion of the composition field $c(\vec{r}, t)$. As the first step, the chemical potential is derived. Then, it is used to obtain the mass flux along its gradient. Combined with a continuity equation for the mass conservation, this yields the Cahn-Hilliard equation for the composition field.

For the binary system described in the previous section, the net flux of one of the two kinds of particles can be determined as:

$$\mathbf{J} = -M\nabla\mu,$$

where M is the mobility, and μ is the chemical potential of the mixture. According to classical thermodynamics, chemical potential can be expressed in terms of the variation of free energy potential as $\mu = \frac{\partial F}{\partial c}$.

Based on the assumption of mass conservation, the Cahn-Hilliard equation can be determined:

$$\frac{\partial c(\vec{r}, t)}{\partial t} = -\nabla \cdot \mathbf{J} = \nabla \cdot M\nabla\frac{\delta F(c)}{\delta c}. \tag{1.4}$$

A typical choice for the free energy is the Ginzburg-Landau functional:

$$F = \int dV \left[\frac{K}{2}(\nabla c)^2 + f(c)\right], \tag{1.5}$$

where, K is the gradient energy coefficient [84]. It takes into account the role of the diffused interfaces of the composition fluctuations, with a role analogous to that of an interfacial free energy.

The functional derivative of $F(c)$ is given by

$$\delta F = \int \left[\frac{\partial f}{\partial c} \delta c + \frac{1}{2} K \nabla_r \delta c \nabla_r c + \frac{1}{2} K \nabla_r c \nabla_r \delta c \right] d\vec{r}.$$

With the use of equations of a partial integration $\left(\int \nabla_r \delta c \nabla_r c = \delta c \nabla_r c - \int \delta c \nabla^2 c \right)$ on the integration surface and $\nabla_r c = 0$ the formula can be modified:

$$\delta F = \int \left[\frac{\partial f}{\partial c} - K \nabla^2 c \right] \delta c d\vec{r},$$

and

$$\frac{\delta F(c)}{\delta c} = \frac{\partial f}{\partial c} - K \nabla^2 c. \tag{1.6}$$

Finally, the time-dependent evolution of the concentration can be described by inserting equation Equation (1.6) in equation Equation (1.4):

$$\frac{\partial c(\vec{r}, t)}{\partial t} = \nabla \left[M(c) \nabla \left[\frac{\partial f}{\partial c} - K \nabla^2 c(\vec{r}, t) \right] \right]. \tag{1.7}$$

The free energy density in the homogeneous phases, $f(c)$, can be described by a double-well potential:

$$f(c) = -\frac{a}{2} \left(c - c_{crit} \right)^2 + \frac{b}{4} \left(c - c_{crit} \right)^4, \tag{1.8}$$

where $b = const > 0$. The unstable region corresponds to $a > 0$ so that $f(c)$ has a double-well structure. The equilibrium concentrations, c_S and c_D, are determined by the minima of the double-well: $c_{crit} \pm \sqrt{a/b}$, where c_{crit} is the concentration at the critical point (Figure 1.2). It is worth noting, that, here, we do not use the Flory-Huggs-de Gennes free energy functional, introduced earlier (Equation (1.3)). The corresponding derivation can be found in [101]. The Ginzburg-Landau model was shown to produce reasonable results, being much simpler in operation [102]. Therefore, for presentation of the Cahn-Hilliard theory we will stick to this description of the system. Inserting equation Equation (1.8) to Equation (1.7) results in:

$$\frac{\partial c(\vec{r}, t)}{\partial t} = \nabla \left[M(c) \nabla \left(-a \left(c - c_{crit} \right) + b \left(c - c_{crit} \right)^3 - K \nabla^2 c \right) \right]. \tag{1.9}$$

1.3.1. The model

The Equation (1.9) can be renormalized, using transformations:

$$\vec{r} \to \sqrt{\frac{K}{a}}\vec{r},$$

$$t \to \frac{K}{M_0 a^2}t,$$

$$c(\vec{r}, t) \to \sqrt{\frac{a}{b}}u(\vec{r}, t) + c_{crit},$$

where M_0 is the arbitrary prefactor of the mobility functions. It includes the physical unity of mobility.

Thus, the Cahn-Hilliard equation may be rewritten as:

$$\frac{\partial u(\vec{r}, t)}{\partial t} = \nabla \left[m(u)\nabla \left(-u + u^3 - \nabla^2 u \right) \right], \tag{1.10}$$

for which the equilibrium values of the rescaled time-dependent concentration variable (u_S and u_D as an analogy for c_S and c_D) are equal to ± 1. The critical point is renormalized to $u_c = 0$ and $T_c = 1$.

To include the information about the current temperature T, Equation (4.4) can be modified [103, 104]:

$$\frac{\partial u(\vec{r}, t)}{\partial t} = \nabla \left[m(u)\nabla \left(-\frac{T_c - T}{T_c}u + u^3 - \nabla^2 u \right) \right], \tag{1.11}$$

where $\frac{T_c - T}{T_c}$ is the reduced temperature. For classical LLPS the mobility function $m(u)$ is constant.

What is the long-term behavior of the system which follows the Cahn-Hilliard equation? Over time the free energy can only decrease:

$$\frac{d}{dt}F(c) = \int \frac{\delta F}{\delta c}\frac{\partial c}{\partial t}d\vec{r} \overset{\text{CH eq.}}{=} \int \frac{\delta F}{\delta c}\nabla \cdot M\nabla \frac{\delta F(c)}{\delta c}d\vec{r} = -\int \underbrace{M}_{>0} \underbrace{\left(\nabla \frac{\delta F(c)}{\delta c} \right)^2}_{\geq 0} d\vec{r} \leq 0.$$

The minimization of F can be achieved by the minimization of $f(c)$ or $\frac{K}{2}(\nabla c)^2$ (see Equation (1.5)). In the first case, the concentration will tend to reach the values of c_S or c_D after a short time because the $f(c)$ is minimal there. In the second case, the $(\nabla c)^2$ is an energetic penalty for gradients of c. Thus, the dynamics tends to reduce the boundaries between regions with $c = c_S$ or $c = c_D$, which leads to coarsening dynamics: the regions with equal concentration merge

with larger regions to form less boundaries.

In the context of the later stages of spinodal decomposition, two coarsening mechanisms are usually discussed: evaporation-condensation [105–107] and Brownian-coagulation due to collision between droplets, caused by their thermal diffusion without any interaction [105, 108, 109]. The first one is known as Liftshitz-Slyozv-Wagner (LSW), and the second mechanism is Binder-Stauffer (BS). The LSW mechanism proceeds with condensation of the material dissolved from the domains with higher curvature (small droplets) on domains with smaller curvature (large domains). This mechanism is the general form of Ostwald ripening [110, 111] and its growth rate follows the equation [112]:

$$\frac{\partial \xi}{\partial t} \sim \frac{\sigma}{\xi^2},$$

where ξ is the characteristic length of LLPS and σ is the interface tension. The resulting growth law is $\xi \sim t^{1/3}$. For the BS mechanism the growth rate depends on the dimensionality d of the system:

$$\frac{\partial \xi}{\partial t} \sim \frac{1}{\xi^{d-1}}.$$

For the three-dimensional system ($d = 3$) it also results in $\xi \sim t^{1/3}$. This power law is frequently observed for the classical spinodal decomposition.

1.3.2 Numerical simulation

The Cahn-Hilliard equation, in general, cannot be solved analytically. Thus, numerical simulation is required for the detailed comparison of the experiment with the theoretical behavior.

In this thesis, the 2D Cahn-Hilliard simulation is used. In order to solve Equation (4.4), it is discretized on a square lattice of $N_x \times N_y$ points [102]. The boundary conditions are periodic. Considering lattice spacing as h, the space vector $\vec{r}$ can be rewritten as $\vec{r} = h \cdot (i, j)$, where $i \in [1, N_x]$ and $j \in [1, N_y]$. Thus, $u(\vec{r_{i,j}}) \equiv u_{i,j}$ and the chemical potential $\mu_{i,j} = \mu\left(u\left(\mathbf{r}_{i,j}\right)\right)$, $\mu(u) = -\frac{T_c - T}{T_c} u + u^3 - \nabla^2 u$. The $\nabla m \nabla \mu$ can be rewritten via a second-order finite-difference formula

[113]:

$$\nabla m \nabla \mu \sim \frac{1}{h^2} \left[m_{i+\frac{1}{2},j} \left(\mu_{i+1,j} - \mu_{i,j} \right) + m_{i-\frac{1}{2},j} \left(\mu_{i-1,j} - \mu_{i,j} \right) \right.$$
$$\left. + m_{i,j+\frac{1}{2}} \left(\mu_{i,j+1} - \mu_{i,j} \right) + m_{i,j-\frac{1}{2}} \left(\mu_{i,j-1} - \mu_{i,j} \right) \right].$$

The Laplacians, e.g. $\nabla^2 u_{i,j}$, which appear in $\mu(u)$ can be approximated by the five-point formula:

$$\nabla^2 u_{i,j} \sim \frac{1}{h^2} \delta^2 u_{i,j} = \frac{u_{i+1,j} + u_{i-1,j} + u_{i,j-1} + u_{i,j+1} - 4u_{i,j}}{h^2}.$$

The values of the mobility at the interstitial lattice points $\left(i \pm \frac{1}{2}, j \right)$ and $\left(i, j \pm \frac{1}{2} \right)$ can be approximated by linear interpolation:

$$m_{i\pm1/2,j} = m \left[\frac{1}{2} \left(u_{i,j} + u_{i\pm1,j} \right) \right], \quad \text{and} \quad m_{i,j\pm1/2} = m \left[\frac{1}{2} \left(u_{i,j} + u_{i,j\pm1} \right) \right].$$

After the discretization in space, the Equation (4.4) transforms into a system of $N_x \cdot N_y$ nonlinear differential equations:

$$\frac{d\mathbf{u}(t)}{dt} = \mathbf{F}[\mathbf{u}(t)].$$

Here, $\mathbf{F}$ is the difference operator, representing the right-hand side of Equation (4.4) and $\mathbf{u}(t) = \left(u_{1,1}(t), u_{2,1}(t), \ldots, u_{N_x,N_y}(t) \right)^\top$ is the vector of the normalized concentration values at the lattice points. The system can be integrated numerically using different schemes. For this thesis, the Euler solver was used [114]:

$$\mathbf{u}(t + \tau) = \mathbf{u}(t) + \frac{1}{2} \tau \mathbf{F}[\mathbf{u}(t)],$$

where τ is the time step. For the convergence of the solution, the stability of a consistent finite-difference scheme is required. To avoid the instability, we should observe the following inequality [102]:

$$\tau < \frac{h^4}{8\gamma \left(8 - \beta h^2 \right)},$$

where $\gamma = m(u_0)$, $\beta = 1 - 3u_0^2$ and u_0 is the initial concentration.

The Cahn-Hilliard modeling is widely used for the description of phase separating systems such as alloys [115], or polymer blends [116–118] and is an intense area of research. In addition, it is encountered in the literature for many

other applications, such as planet formation [119] and cancer growth [120].

In this thesis, the classical Cahn-Hilliard simulation is used for modeling the behavior of the LLPS of the BSA-YCl$_3$ model system in response to a temperature jump (see Section 4.3.2 for details). After the simulation of the real-space evolution of the concentration field, the scattering intensity is calculated via the Fourier transform. Later, this data is used to mimic the XPCS measurements and their comparison with the actual experimental results.

1.4 Salt mediated protein-protein interactions
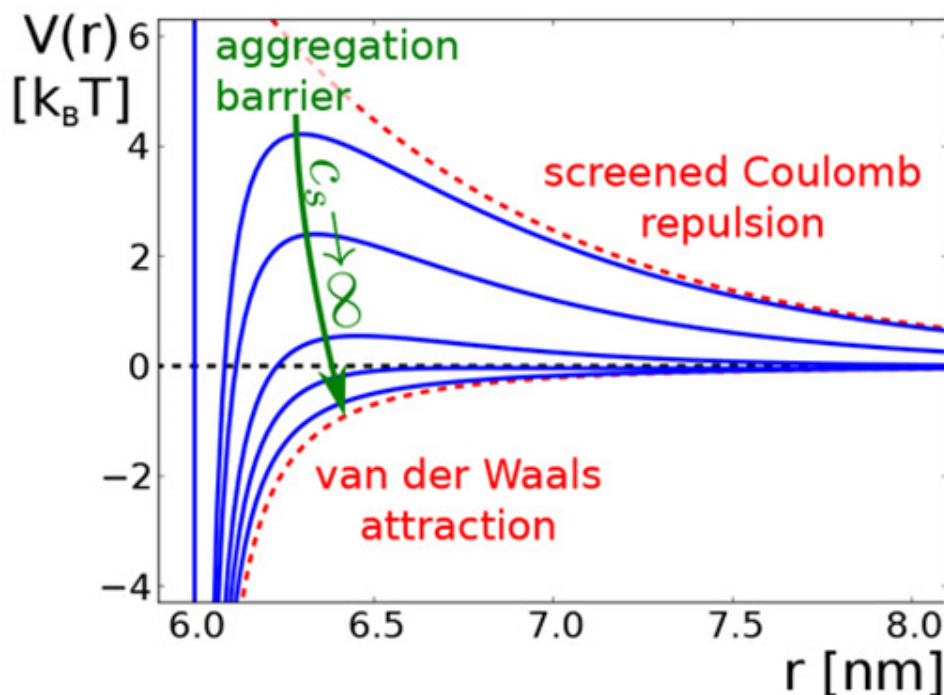
Figure 1.3: DLVO potential for varying salt concentration c_s. With increasing c_s, the potential changes from repulsive to attractive. The aggregation barrier reflects the weaker charge stabilization behavior due to charge screening. Adapted from [75].

The protein-protein interaction potential, V_{pp}, discussed in Section 1.1, can be manipulated through the addition of salt. According to the DLVO theory, an increase in the salt concentration in a (given) protein-salt solution leads to a decrease in electrostatic repulsion between charged proteins at short distances due to charge shielding (Figure 1.3). Finally, the van der Waals attraction

may cause aggregation and precipitation [75, 121]. The DLVO theory may be successfully applied to predict parameters such as the pH and ionic strength trends of protein-protein interaction [122–124]. Nevertheless, as was mentioned in Section 1.1, there are some limitations to this approach. Due to the use of Poisson-Boltzmann theory [125], the DLVO considers salt ions as point charges. Thus, the ion-ion interactions, properties of the salt (e.g., valency), non-electrostatic interactions, or inhomogeneity of charge distribution are out of scope [73, 124, 126]. Therefore, it is not surprising that many observed ion effects cannot be explained by DLVO [127–129].

This section will briefly discuss the effects of salts on protein phase behavior, such as re-entrant condensation and liquid-liquid phase separation. The emphasis is placed on the BSA-YCl_3 system, given that it was directly investigated in this work. A more detailed discussion of this topic can be found in the following reviews [75, 122, 130, 131], and is beyond the scope of this work.

1.4.1 Protein phase behavior induced by multivalent cations
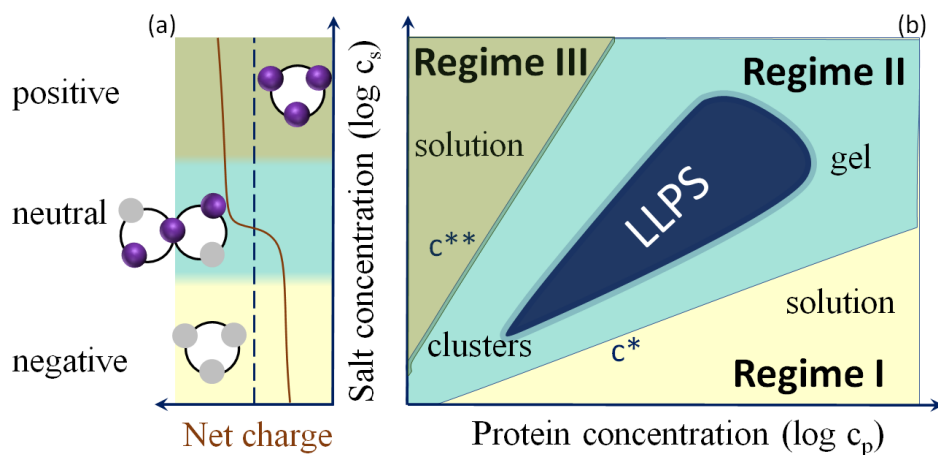
Figure 1.4: Scheme of the evolution in the net charge with the increase of the salt concentration (a) and corresponding phase diagram, showing regimes I, II, and III, re-entrant condensation, and LLPS (b). Modified from [75].

For many proteins, such as the investigated BSA, there is no complex phase behavior unless salts are added, allowing overcoming the electrostatic repulsion between negatively charged proteins. Presence of high valent salts, such as YCl_3, $LaCl_3$, $HoCl_3$, $CeCl_3$, $La(NO_3)_3$, $FeCl_3$, and $AlCl_3$, leads to the so-called re-entrant condensation (RC) phenomenon [42, 43, 75, 132–136]. The salt concentration

can be used as a control parameter for protein phase diagrams, which facilitates the formation of LLPS for experiments under laboratory conditions for many protein solutions (Figure 1.4). The induced phase behavior may be divided into three regimes. Regime I corresponds to the system in a homogeneous liquid state at a certain protein concentration c_p and a low salt concentration c_s. An increase in c_s at constant c_p decreases the negative surface charge of the protein due to the ion binding. At a certain critical salt concentration, c^*, the protein molecules start to condense into cluster-like structures due to the ion bridging. This state is referred to as regime II. Under certain conditions, LLPS may occur at this stage. A further increase of c_s leads to a charge inversion of the protein surface and a non-monotonous reduction in attraction between proteins. Upon surpassing a second critical salt concentration, c^{**}, the clusters redissolve, and the system may be again described as a homogeneous liquid (regime III).

1.4.2 BSA-YCl$_3$ model system

In this thesis, the investigation of the dynamics of liquid-liquid phase separation by coherent X-ray scattering is performed on the model system of the bovine serum albumin (BSA) in the presence of Yttrium chloride (YCl$_3$).

BSA is a compact globular protein with a molecular weight of 67 kDa [137–139] and a radius of gyration close to 3nm [140]. At neutral pH, BSA is negatively charged as its isoelectric point (pI) is pH 4.7 (acidic protein) [141]. BSA is abundant in the blood of mammals and has a physiological role as a transport protein for fatty acids, cations, and other small molecules. Furthermore, it is responsible for maintaining the osmotic pressure of the blood and has the role of physiological buffer [138, 142, 143]. In biochemical laboratories, BSA is commonly used as a blocker (e.g., for ELISA-test), a molecular weight standard, and a concentration standard [144, 145].

The phase behavior of bulk systems composed of BSA and multivalent cations has been extensively investigated over the past decade [44, 45, 49, 130, 131, 135, 146–149]. The re-entrant condensation has been established with LLPS, and the phase behavior was rationalized in terms of ion-activated patchy interactions [44, 75, 150–155]. The phase diagram for BSA-YCl$_3$ is established in the axes of salt concentration, protein concentration, and temperature. The LLPS occurs upon temperature increase, which is referred to as a lower critical solution
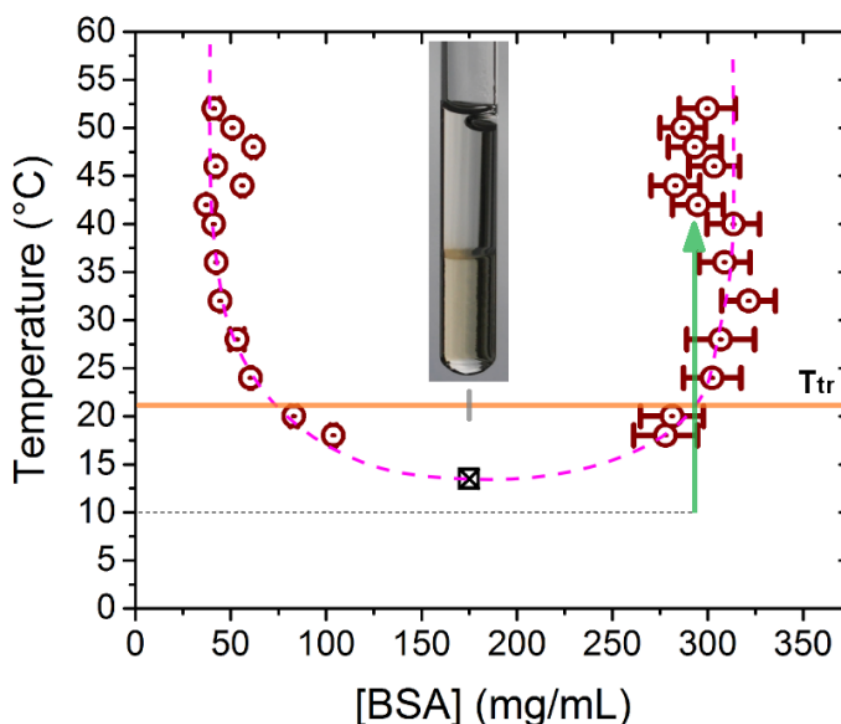
Figure 1.5: Binodal of the LLPS for BSA-YCl$_3$ system with an initial protein concentration of 175 mg mL^{-1} and salt concentration of 42 mM. The orange line marks the temperature of the sample preparation of the parent solution. The critical temperature is marked with a black square. After the phase separation, the dense phase is taken for further experiments. Its concentration can be found at the intersection of the green arrow and the orange line. The green arrow represents a typical temperature jump. The inset shows a photo of a sample tube after LLPS and sedimentation. The yellowish part corresponds to the dense phase, while the transparent one – to the dilute phase. The figure is adapted from [46].

temperature (LCST) behavior [44, 131]. The phase diagram for BSA-YCl$_3$ with an initial protein concentration of 175 mg mL^{-1} and salt concentration of 42 mM is presented in Figure 1.5. The kinetics of the system was well established by USAXS and VSANS [45, 46].

Chapter 2

X-ray scattering techniques

This chapter aims to introduce the concepts of X-ray scattering theory. First, it describes the basics of ultra-small angle X-ray scattering (USAXS), which is widely used for kinetical studies. Then, the overview focuses on the coherent scattering and X-ray photon correlation spectroscopy (XPCS) technique for the dynamical studies.

2.1 Fundamentals of X-ray scattering

This section describes the basic principles and introduces the necessary scattering physics terms. It is mainly based on the books "Elements of Modern X-Ray Physics" by J. Als-Nielsen and D. McMorrow [156] and "Neutrons, X-rays and Light Scattering Method Applied to Soft Condensed Matter" edited by P. Lindner and Th. Zemb [157].

In order to discuss the core techniques used for this thesis, the basic geometry of a scattering experiment should be recalled. It is represented in Figure 2.1 and is general for different radiation types (X-rays, neutrons, light).

The incident radiation can be considered as a plane monochromatic wave with the wavevector $\vec{k_i}$ along the direction of propagation. The magnitude of k_i can be described as $k_i = \frac{2\pi}{\lambda}$, where λ is the wavelength of light in the medium. The wave is scattered by a sample at the angle 2θ to the detector in the far field. The scattered wave can be described by the wavevector $\vec{k_f}$. We assume that there is no multiple scattering, the incident beam has not received significant distortion by the medium, and the scattering process is elastic, implying there is no change in the frequency. Thus, the magnitude k_f is equal to k_i and is also $\frac{2\pi}{\lambda}$.

The scattering wavevector $\vec{q}$ is defined as the difference between the wave-
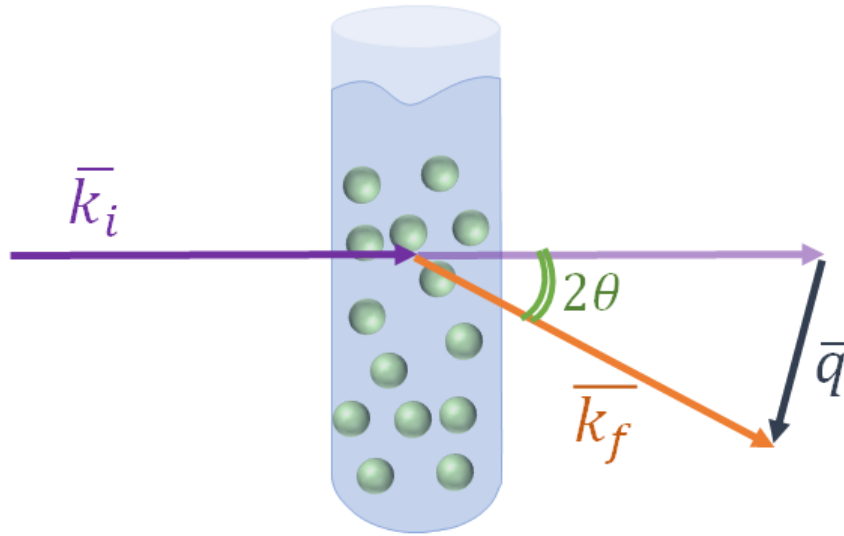
Figure 2.1: Schematic representation of the scattering experimental setup in case of elastic scattering. The incoming beam exposes the sample with the wavevector $\vec{k_i}$ (violet arrow). The wave, scattered at the angle 2θ, can be described by wavevector $\vec{k_f}$ (orange arrow). The scattering vector $\vec{q} = \vec{k_f} - \vec{k_i}$ is represented by the grey arrow.

vectors of the scattered and incident light:

$$\vec{q} = \vec{k_i} - \vec{k_f}.$$

By simple trigonometric considerations, its magnitude can be calculated as:

$$q = |\vec{q}| = \frac{4\pi \sin\theta}{\lambda}.$$

For further description, we will consider a particulate system, where distinct particles are suspended in a medium. This approach is valid for protein solutions at high values of q (corresponding to a sufficiently small length scale). Each atom in a particle may be associated with a so-called scattering length b that expresses the efficiency of scattering by the atom. Then, the scattering length density of a particle of volume V_P is given by:

$$\rho(\vec{r}) = \frac{1}{V_P} \sum_j b_j(\vec{r}).$$

The scattering amplitude of one single particle in a solution can be described as the Fourier transform of the scattering density distribution:

$$F(\vec{q}) = \int_{V_P} \Delta\rho(\vec{r})e^{-i\vec{q}\vec{r}}d\vec{r},$$

where $\Delta\rho(\vec{r})$ is the difference between the scattering densities of the particle and the solvent.

The scattering intensity of an individual particle is proportional to the orientational averaged squared scattering amplitude. It is known as the isotropic form factor $P(\vec{q})$ and contains information about the shape of the particle:

$$P(\vec{q}) = \left\langle |F(\vec{q})|^2 \right\rangle = \left\langle \left| \int_{V_P} \Delta\rho(\vec{r})e^{-i\vec{q}\vec{r}}d\vec{r} \right|^2 \right\rangle.$$

The scattering pattern, $I(\vec{q})$, from the system with multiple particles is more complicated. It depends not only on the shape of particles but also on their relative positions. The contribution of the particle shape to the scattering pattern is the form factor described above, which should be additionally averaged over different particles. The contribution of the interference between waves scattered by different particles is known as the structure factor $S(\vec{q})$. For N identical particles in a homogeneous solution it can be derived as the following [158, 159]:

$$S(\vec{q}) = \frac{1}{N} \sum_{i=1}^{N} \sum_{j=1}^{N} e^{-i\vec{q}(\vec{r}_i - \vec{r}_j)}. \tag{2.1}$$

For the concentrated protein solutions, it can be rewritten in terms of the pair correlation function between the particles [83]:

$$S(\vec{q}) = 1 + \frac{N-1}{V} \int_V g(\vec{r})e^{-i\vec{q}\vec{r}}d\vec{r}, \tag{2.2}$$

where $g(\vec{r})$ is the pair correlation function, V is the volume and r is the center-to-center distance between the particles.

Thus, kinetic changes of the sample will be reflected in the changes in the scattering intensity. Furthermore, as the scattering process is described by a Fourier transform, it may be shown that the real space features of a typical size $\sim d$ contribute to the scattered radiation at the scattering vector $q = 2\pi/d$. Therefore,

depending on the area of research interest, various scattering techniques are available (SAXS, WAXS, USAXS), with different q-range. In this thesis, we focus on the USAXS experiments of LLPS.

2.2 Ultra-small angle X-ray scattering for studying kinetics

Protein solutions under phase separation display large-scale structures of the order of hundreds of nanometers to tens of micrometers which corresponds to the q values in the range from 0.1 to 60 μm^{-1}. A special experimental setup is required to follow the kinetic evolution of these domains. Once the sample enters the two-phase regime, it becomes opaque. This puts limitations on the visible light techniques, such as microscopy or small-angle light scattering, which can be easily overcome by employing X-rays instead. The q-range of interest corresponds to the ultra-small angle X-ray scattering technique (USAXS). The high brilliance of synchrotron X-ray sources makes it possible to perform time-resolved measurements. The information can be obtained over a comparatively large volume of the solution allowing to catch the average kinetics of the sample.

In the USAXS range, the form factor of the proteins is not visible, and the structure factor mainly determines the scattering profile. According to the Cahn-Hilliard theory (Section 1.3.1), there is an amplification of concentration fluctuations during LLPS. Its characteristic length is determined by the diffusion balance along the chemical potential gradient and interface tension. The coarsening of domains is reflected by the change in the position of the characteristic peak of the structure factor, q_{peak}. The evolution of this peak gives information about the kinetics of the sample by calculating the characteristic length: $\xi = 2\pi/q_{peak}$.

2.3 Coherence and speckles

In Section 2.1, it was mentioned that the scattering intensity includes information about the relative positions of the particles. This property leads us to the idea that changing these positions may lead to a corresponding change in the scattering pattern. Is there a way to extract not only the kinetics but also the dynamical information of the sample? In this chapter, we will describe how

coherent radiation helps in the study of dynamics.

When a coherent beam of light illuminates an object with any type of disorder (static or dynamic), the scattered light is broken up into bright and dark regions that can be seen by a 2D detector. This phenomenon results from the irregular phase differences and hence irregular interference between the waves scattered from different parts of the object. The observed apparently random array of bright spots is known as a speckle pattern [160, 161]. A detailed overview of the speckle phenomenon can be found in [162, 163].

For illustration consider the scattering scheme discussed in Section 2.1 (Figure 2.1). If the scattering occurred at the points (r_1, t_1) and (r_2, t_2), the electric filed, $\vec{E}$, created by two scattering waves, $\vec{E}_1(\vec{r}, t)$ and $\vec{E}_2(\vec{r}, t)$, may be written as:

$$\vec{E} = \vec{E}_1 + \vec{E}_2.$$

Then, the intensity of the resulted field:

$$
\begin{aligned}
I = \left\langle |\vec{E}|^2 \right\rangle = \left\langle \vec{E}\vec{E}^* \right\rangle = \left\langle \left(\vec{E}_1 + \vec{E}_2\right)\left(\vec{E}_1^* + \vec{E}_2^*\right) \right\rangle = \\
= \left\langle \vec{E}_1\vec{E}_1^* \right\rangle + \left\langle \vec{E}_2\vec{E}_2^* \right\rangle + \left\langle \vec{E}_1\vec{E}_2^* + \vec{E}_2\vec{E}_1^* \right\rangle = \\
= I_1 + I_2 + 2\left\langle \mathrm{Re}\left\{\vec{E}_1\vec{E}_2^*\right\} \right\rangle,
\end{aligned}
\tag{2.3}
$$

where $*$ means complex conjugation and $\langle\rangle$ is the ensemble average.

Thus, if the phase difference between the points (r_1, t_1) and (r_2, t_2) is not random, i.e. $< \vec{E}_1\vec{E}_2 >! = 0$, the interference will occur. The visibility of the interference phenomena depends on the coherence of the light source. To describe the correlation between $\vec{E}_1(\vec{r}, t)$ and $\vec{E}_2(\vec{r}, t)$ the mutual coherence function can be introduced:

$$\Gamma\left(\vec{r_1}, \vec{r_2}; t_1, t_2\right) = \left\langle \vec{E}_1^*(\vec{r_1}, t_1))\vec{E}_2(\vec{r_2}, t_2)) \right\rangle.$$

The complex degree of coherence is the normalized mutual coherence function:

$$\gamma\left(\vec{r_1}, \vec{r_2}; t_1, t_2\right) = \frac{\Gamma\left(\vec{r_1}, \vec{r_2}; t_1, t_2\right)}{\sqrt{I_1}\sqrt{I_2}}.
\tag{2.4}$$

Applying the Cauchy–Schwarz inequality to Equation (2.4), it can be derived that:

$$0 \leq \left|\gamma\left(\vec{r_1}, \vec{r_2}; t_1, t_2\right)\right| \leq 1.$$

Finally, Equation (2.3) can be rewritten as:

$$I = I_1 + I_2 + 2\sqrt{I_1 I_2} \, \mathrm{Re}\left[\gamma\left(\vec{r}_1, \vec{r}_2; t_1, t_2\right)\right].$$

Suppose the intensities I_1 and I_2 are equal. In that case, the absolute value of the complex degree of coherence with no pathlength difference can be obtained experimentally via the visibility of interference fringes in a Michelson interferometer, which is also called the contrast of the interference pattern:

$$\beta_0 = \frac{I_{\max} - I_{\min}}{I_{\max} + I_{\min}} = |\gamma\left(\vec{r}_1 = \vec{r}_2; t_1, t_2\right)|.$$

Here, $I_{\max}$ and $I_{\min}$ are the maximum and minimum intensity of the interference pattern. Two extreme cases, when $|\gamma\left(\vec{r}_1 = \vec{r}_2; t_1, t_2\right)| = 1$ and $|\gamma\left(\vec{r}_1 = \vec{r}_2; t_1, t_2\right)| = 0$, correspond to the fully coherent and completely incoherent beam, respectively. Intermediate values describe a partially coherent source. For a same point ($\vec{r}_1 = \vec{r}_2 = \vec{r}$ and $t_1 = t_2 = t$), the degree of coherence is equal to unity and the field is always coherent with itself ($|\gamma\left(\vec{r}, \vec{r}; t, t\right)| = 1$). With increase of spatial separation, $\vec{r}_1 - \vec{r}_2$ and time delay, $t_1 - t_2$, the magnitude of the correlation function $|\gamma\left(\vec{r}_1 = \vec{r}_2; t_1, t_2\right)|$ decays. The region where the electromagnetic field is highly correlated is called the coherence volume. Inside the coherence volume photons are not distinguishable from each other - they have the same spatial coordinate and momentum with the precision allowed by quantum mechanics. The spatial and temporal dimensions of the coherence volume are called transverse, l_t, and longitudinal coherence lengths, l_l, respectively.

The transverse (spatial) coherence is the ability of the wave to interfere at different spatial points of the wavefront. Two source points transversely separated up to a distance l_t will have phases still correlated within π. The transverse coherence length l_t is determined by the collimation and is inversely proportional to the angular size of the source, Ω_S. Thus, l_t at a distance L from the source can be determined by the source size σ and wavelength λ:

$$l_{t_{h,v}} = \frac{\lambda}{2} \frac{1}{\Delta\Omega_{S_{hv}}} = \frac{\lambda}{2} \frac{L}{\sigma_{h,v}}, \tag{2.5}$$

where h and v indicate horizontal and vertical components. The formula comes from the Van Cittert-Zernike theorem [164]. According to this formula, all sources are fully transversely coherent if L is sufficiently large (e.g., stars).

The transverse coherence increases by decreasing the emittance of a source. The degree of transverse coherence can be measured in Young's double-slit experiment. The visibility of fringes significantly decreases once the two slits are separated by more than l_t [165].

Longitudinal (temporal) coherence defines the ability of the wave to interfere with the delayed version of itself. Two waves with (slightly) different wavelengths will have phases still correlated within π after traveling over the path l_l. The longitudinal coherence is related to the monochromaticity of the wave, i.e., the spectral bandwidth of the source $\frac{\delta\lambda}{\lambda}$. The corresponding coherence length can be defined from the Wiener-Khintchine theorem [164]:

$$l_l = \frac{\lambda^2}{2\delta\lambda}.$$

(2.6)

An increase in the longitudinal coherence is achieved by narrowing the bandwidth with a monochromator. The longitudinal coherence can be observed with a Michelson interferometer [166].

Together longitudinal and transverse coherence lengths determine a coherence volume, where the scattering can be considered to be fully coherent. A necessary condition for performing coherent scattering measurements is that the scattering volume of the sample does not greatly exceed the coherence volume.

A comparison of the scattering patterns by the incoherent and coherent beams is presented in Figure 2.2. For incoherent diffraction, the scattering is featureless apart from time-averaged correlations in the sample, related to the kinetics. For example, the radius of the scattering ring corresponds to the average interparticle distance $\xi \sim \frac{2\pi}{q_{ring}}$. For coherent diffraction, the speckle pattern can be resolved. The intensities $I(q, t)$ in a speckle pattern encode the exact spatial arrangement $r_n(t)$ of the scatters in disordered system. The speckle size, s, is determined by the sample-to-detector distance, R, and the beam size d: $s = \frac{\lambda R}{d}$. To resolve speckles, the pixel size of the detector should be equal to or less than the speckle size.

Thus, potentially the coherent diffraction contains much more information than incoherent scattering. However, an advanced analysis is required to extract this information. If positions $\vec{r_n}$ of particles change with time, the fluctuation of speckles will show dynamics of the spatial frequency probed by the q-vector. Obtaining dynamic information from speckle fluctuations is the goal of X-ray Photon Correlation Spectroscopy (XPCS).
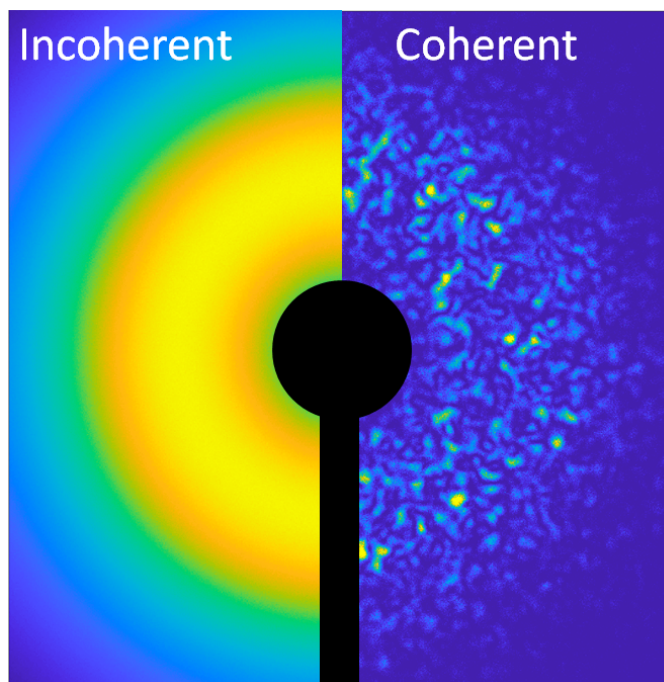
Figure 2.2: Representation of the Ultra-small angle scattering signal of the domains of LLPS sample measured with incoherent (left) and coherent (right) beam. The radius of the scattering ring corresponds to the average interparticle distance $\xi \sim 2\pi/q_{ring}$. Courtesy of Ivan Zaluzhnyy.

2.4 X-ray photon correlation spectroscopy for study of dynamics

X-ray Photon Correlation Spectroscopy (XPCS) is a coherent X-ray scattering technique that is used to investigate dynamics by measuring the fluctuations of the speckles.

The history of experimental Photon Correlation Spectroscopy begins with the advent of the laser. In 1964 Pecora demonstrated the use of the coherent light of the laser for extraction of the diffusion coefficients of macromolecules [167]. The established technique is currently known as Dynamic Light Scattering (DLS) [168–170]. XPCS technique was introduced as an analog to DLS, extending to smaller length scales. First XPCS experiments were demonstrated in 1994 [171] as a result of the advent of third-generation synchrotron radiation sources. Further development of synchrotrons and subsequent free-electron lasers (e.g. European XFEL, LCLS, PAL, SACLA) along with boosted creation of a new type of detectors in the following 20 years have advanced XPCS technique and made
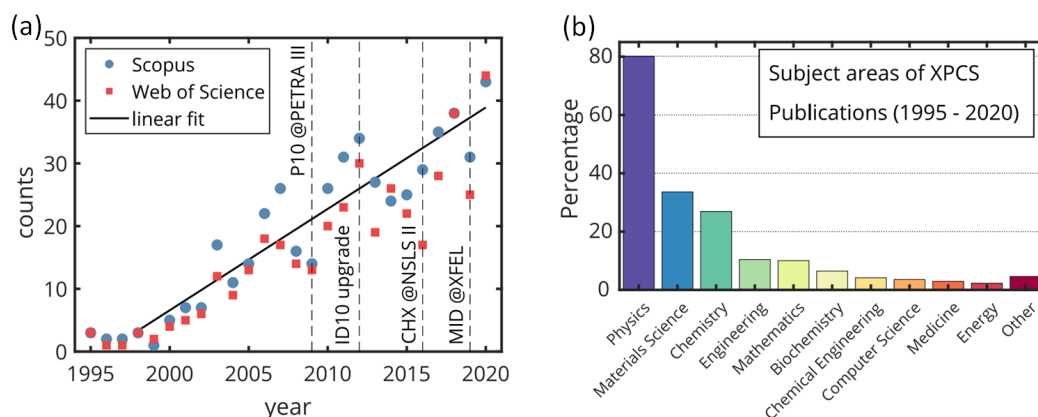
Figure 2.3: (a) A number of XPCS publications per year. Dash line marks the starting dates of new XPCS-relevant beamlines or updates for the existing ones. (b) Percentage of XPCS publications by subject areas in the year range from 1995 to 2020 (multiple areas are possible for each publication). The figure is adapted from [172].

it possible to measure dynamics over 18 orders of magnitude with coherent X-rays [172]. The development of XPCS is presented in Figure 2.3 which is adapted from [172]. Since the late 1990s, there is a linear growth in the number of XPCS publications, resulting in more than 40 publications per year nowadays.

Current state of XPCS and light sources enables to investigate dynamics with time scales range from femtoseconds to hours and length scales ranging from microns down to angstroms [54, 172] (Figure 2.4). XPCS is used in different areas of soft condensed matter research areas (see Figure 2.3 (b)) for studying the dynamics of colloids [56, 173–195], liquids and liquid crystals [57, 97, 196, 197], polymers [58, 198–210] as well as metallic and molecular glasses [211–214], magnetic systems [54, 178, 215–217] and clays [59]. In these systems a variety of important dynamical phenomena have been studied with XPCS: aging of the colloidal gel and colloidal glass transition [192], polymerization and gelation of polymers [218], phase transitions and phase separations [219, 220], diffusion [221], jamming transition [185, 193] and many others. XPCS is perfect for the investigation of mesoscale dynamics of biomaterials, which scales are impossible to achieve with usual methods, such as Inelastic Neutron Scattering (INS), Inelastic X-ray Scattering (IXS), Spin-Echo and others (Figure 2.4). DLS can be used for this range, but it misses the spatial resolution and is plagued by multiple scattering in dense and opaque solutions. Nevertheless, despite the obvious advantages of bio-XPCS, only initial steps were made for the investigation of
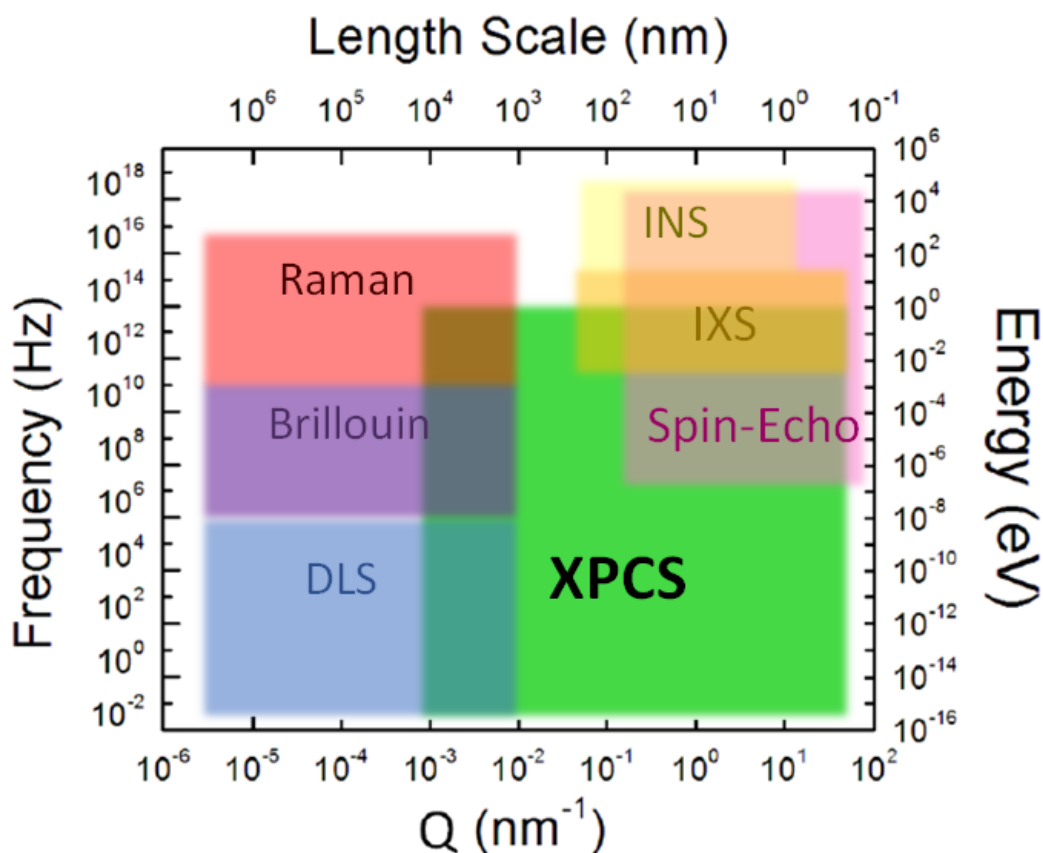
Figure 2.4: Energy and length scales covered by XPCS and other spectroscopy techniques. XPCS covers a broad range of length and time scales relevant for bio-materials. It is partially overlapping with the DLS, but unlike it, XPCS remains valid for opaque systems [54]. The figure is modified from [54, 172].

protein systems with this technique [63, 64] due to experimental difficulties in working with beam-sensitive samples [60–62]. This thesis, along with other papers published over the past few years [222–224], demonstrate some of the first XPCS experiments on proteins and expand knowledge in this area.

An exhaustive summary of XPCS research studies and its future perspectives can be found in several reviews by Shpyrko [54], Grübel [225], Sutton [226] and Lehmkühler [172].

2.4.1 Autocorrelation function

The information on the ensemble-averaged dynamical properties can be extracted from the speckle fluctuations by constructing the normalized time-

averaged intensity autocorrelation function [162, 225, 227]:

$$g_2(\vec{q}, \Delta t) = \frac{\langle\langle I(\vec{q}, t) I(\vec{q}, t + \Delta t)\rangle_p\rangle_t}{\langle\langle I(\vec{q}, t)\rangle_p\rangle_t^2}, \tag{2.7}$$

where $\langle\cdots\rangle_p$ denotes pixel averaging for the investigated q-ring and $\langle\cdots\rangle_t$ is the averaging over the total time of the measurement. This quantity compares the signal $I(\vec{q}, t)$ with a time-delayed signal $I(\vec{q}, t + \Delta t)$ for all starting (t) and delay (Δt) times. With increase of the delay time, the correlation between these intensities decreases. If the delay time is much greater than the typical fluctuation time of the speckles τ (relaxation time of the system), the intensities $I(\vec{q}, t)$ and $I(\vec{q}, t + \Delta t)$ are uncorrelated. Therefore:

$$\lim_{\Delta t \to \infty} \langle I(\vec{q}, t) I(\vec{q}, t + \Delta t)\rangle = \langle I(\vec{q}, t)\rangle\langle I(\vec{q}, t + \Delta t)\rangle = \langle I(\vec{q}, t)\rangle^2,$$

and $\lim_{\Delta t \to \infty} g_2(\vec{q}, \Delta t) = 1$. If the scattered intensity obeys Gaussian statistics, the Siegert relation can be employed [168, 228]. Thus, the $g_2(\vec{q}, \Delta t)$ function can be connected to the first order correlation function $g_1(\vec{q}, \Delta t)$:

$$g_2(\vec{q}, \Delta t) = 1 + |g_1(\vec{q}, \Delta t))|^2. \tag{2.8}$$

The described equation is valid only for a fully coherent source. In a typical XPCS experiment the source is partially coherent and Equation (2.8) should be modified to:

$$g_2(\vec{q}, \Delta t) = 1 + \beta(\vec{q}) |g_1(\vec{q}, \Delta t))|^2, \tag{2.9}$$

where $\beta(\vec{q})$ is the speckle contrast which is determined by the set-up [225]. The g_1 function is also known as the intermediate scattering function. It can be expressed by the normalized structure factor [172, 225]:

$$g_1(\vec{q}, \Delta t) = S(\vec{q}, \Delta t)/S(\vec{q}, 0) = \frac{1}{N}\left\langle\sum_{k=1}^{N}\sum_{j=1}^{N}\exp\left(i\vec{q}\cdot[\vec{r}_j(\Delta t) - \vec{r}_k(0)]\right)\right\rangle \tag{2.10}$$

Therefore, it contains the sample dynamics via information about the trajectories r_j of all N scatters.

2.4.2 Dynamical models

Depending on the sample dynamics, the g_1 functions may have different forms. Nevertheless, the standard approach which is valid for the majority of the systems is a Kohlrausch-Williams-Watts relation:

$$g_1(\vec{q}, \Delta t) = \exp\left(-(\Gamma(\vec{q})\Delta t)^{\gamma(\vec{q})}\right), \tag{2.11}$$

where Γ is the relaxation rate of the system, and γ is the so-called Kohlrausch-Williams-Watts exponent (KWW) or shape parameter, which is a measure of the distribution of microscopic relaxation processes. The characteristic relaxation time of the system τ can be obtained via $\tau = 1/\Gamma$. It contains information on the mechanism of particle motion on a scale $2\pi/q$. Depending on the value and dependence of these parameters, it is possible to distinguish different particle motions:

- $\gamma = 1$ and $\tau \propto q^2$ corresponds to Brownian motion.

- $\gamma < 1$ and $\tau \propto q$ typically describes hopping of cage particles, sub-diffusive motion and stretched relaxation.

- $\gamma > 1$ and $\tau \propto q$ corresponds to super-diffusion, ballistic-like motion and stress relaxation.

The correlation between the parameters of the Kohlrausch-Williams-Watts equation and the dynamics of the sample is established in the literature for colloidal systems. For sub-diffusive motion ($\gamma < 1$) [177, 179, 207, 209] different regions in the sample can be described by a single exponential decay with different relaxation times τ_i (see Figure 2.5 (a)). The ensemble averaging leads to the stretched behavior [230].

The compressed exponential behavior ($\gamma > 1$) is usually an indicator of the hyper-diffusive non-equilibrium dynamics [179, 182, 209, 211, 213, 214]. The sample can be divided into the regions with spatially cooperative motion of the particles (Figure 2.5 (b)).

By substituting Equation (2.11) into Equation (2.9), the intensity autocorrelation function can be rewritten as:

$$g_2(\vec{q}, \Delta t) = 1 + \beta(\vec{q}) \exp\left(-2(\Delta t/\tau)^{\gamma}\right). \tag{2.12}$$
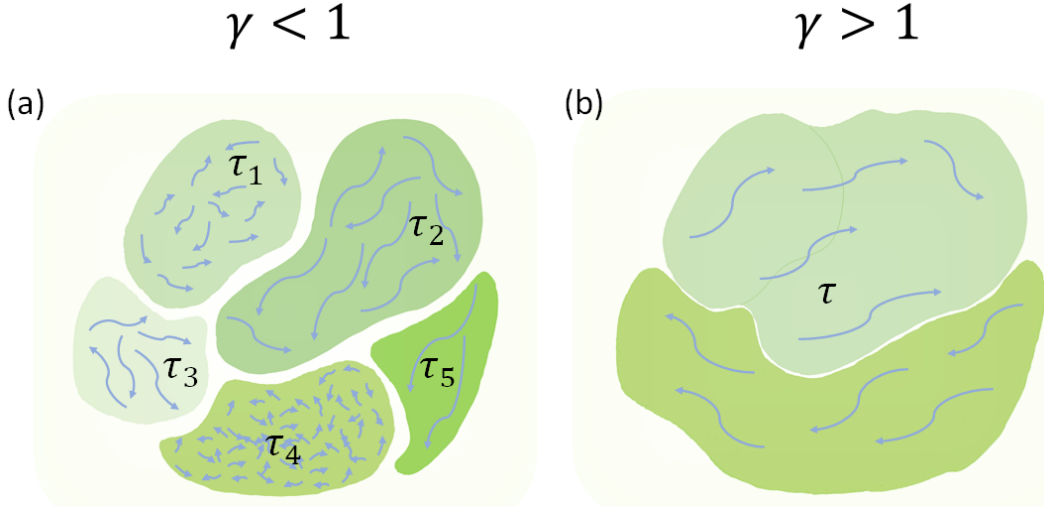
Figure 2.5: Schematic representation of the diffusion behavior of particles in the case of $\gamma < 1$ (a) and $\gamma > 1$ (b). For both cases, τ is the relaxation time of the whole system. Nevertheless, for (a), it results from the ensemble averaging over regions with different relaxation times τ_i. The figure is modified from [229].

2.4.3 Two-time correlation function and its analysis

The method described above with Equation (2.7) has been successfully applied to investigate the dynamics when the system is ergodic (i.e., time average equals ensemble average) and in the equilibrium state. As the temperature changes, the structure of the system changes accordingly to reach a new equilibrium state. When the time required for such structural relaxation is small compared to the experimental time scale, the system could reach the new equilibrium state and remains ergodic. Nevertheless, when the system approaches an arrested state, the relaxation time gradually gets longer compared to the experimental time scale leading to a phenomenon where the system falls out of equilibrium. The process here reflects the transition from an ergodic to a non-ergodic state. In such cases, the dynamics could evolve and strongly depend on the observation time. Moreover, the system could exhibit heterogeneous or non-equilibrium dynamics (e.g., aging), and thus the time averaging becomes invalid. To follow such dynamical evolution, it is reasonable to use the two-time correlation function [231–233]:

$$Corr(\vec{q}, t_1, t_2) = \frac{\langle I(\vec{q}, t_1) I(\vec{q}, t_2) \rangle_p}{\langle I(\vec{q}, t_1) \rangle_p \langle I(\vec{q}, t_2) \rangle_p}. \tag{2.13}$$

2.4.3. Two-time correlation function and its analysis

It calculates the correlation between intensities at times t_1 and t_2 averaged over all pixels at the same q-ring. It can be seen that $Corr(\vec{q}, t_1, t_2) = Corr(\vec{q}, t_2, t_1)$. For this formula the normalization is performed by the mean intensity.

Another possibility for calculation of the two-time correlation function is the autocovariance of the intensity normalized by its standard deviation [232, 234]:

$$G(\vec{q}, t_1, t_2) = \frac{\overline{I(t_1)I(t_2)} - \overline{I(t_1)} \cdot \overline{I(t_2)}}{[\overline{I^2(t_1)} - \overline{I(t_1)}^2]^{\frac{1}{2}} \cdot [\overline{I^2(t_2)} - \overline{I(t_2)}^2]^{\frac{1}{2}}}, \tag{2.14}$$

where $\overline{I} = \langle I \rangle_p$.

For fully coherent light, the speckle pattern follows exponential distribution [235]. In this case, assuming Gaussian statistics of the joint probability density function [236], it can be shown that the average intensity equals the standard deviation [234, 237]. Thus, $G(\vec{q}, t_1, t_2) = Corr(\vec{q}, t_1, t_2) - 1$ and the use of different correlation functions is equivalent. Nevertheless, in the general case, this equality is not true. For partially coherent light intensity follows more general gamma distribution [225]. For typical XPCS experiments on biological samples, which is relevant for this thesis, there are low count intensity rates to avoid beam damage to the sample. In this case, the Poisson distribution of photon detection may affect speckle statistics and lead to the negative-binomial distribution [172]. In addition, the LLPS phenomenon is accompanied by significant changes in the scattering intensity with time. In such a case, using a particular correlation function becomes task-dependent.

For this thesis, the $G(\vec{q}, t_1, t_2)$ function will be used for calculation of TTCs. The standard deviation normalization is less sensitive to the intensity evolution than the normalization to the mean. Furthermore, the Equation (2.14) has both upper ($G(\vec{q}, t_1, t_2) = 1$) and lower bounds ($G(\vec{q}, t_1, t_2) = 0$), regardless of the speckle statistics, while Equation (2.13) limited only from below ($Corr(\vec{q}, t_1, t_2) = 1$).

The use of two-time correlation function for XPCS was first introduced by Brown *et al.* in study of statistical speckle properties for [234] (the $G(\vec{q}, t_1, t_2)$ version). The two-time correlation function is usually represented as a 2D graph known as two-time correlation map (TTC). It demonstrates values of $G(\vec{q}, t_1, t_2)$ (or $Corr(\vec{q}, t_1, t_2)$) for a fixed q-value with axis t_1 and t_2. The TTC is mirror symmetric along the $t_1 = t_2$ axis. There are two ways for extraction of g_2 functions which can be later analyzed with Equation (2.12): horizontal cuts and diagonal cuts. The horizontal cuts at different waiting time t_w are

also known as conventional coordinate system [232] and are performed by extraction of line with $t_1 = constant$ (or $t_2 = constant$) and delay time defined as $\Delta t := |t_2 - t_1|$. The diagonal cuts were also introduced by Brown *et al.* [234] and can be found in the literature as an alternative coordinate system [232]. In this case, the g_2 at different sample age $t_{age} = (t_1 + t_2)/2$ is extracted by taking the line perpendicular to the $t_1 = t_2$ diagonal with the delay time $\bar{t}$ given by $|t_2 - t_1|$.

Historically, the diagonal cuts were introduced earlier and were subsequently widely used [213, 233, 238–244]. However, in 2017, Bikondoa published a paper on the use of two-time correlation functions for XPCS data analysis [232]. He introduced the horizontal cuts and suggested that such a way may be more compatible with the general calculation of autocorrelation functions (e.g., in DLS). Furthermore, he argued that employing diagonal cuts may sometimes pose interpretation problems. Since then, the conventional coordinate system has been gaining popularity and can be encountered relatively often [172, 223, 245]. Nevertheless, diagonal cuts are still widely used today. This method is more convenient for comparison to previous XPCS studies, while horizontal cuts give a better numerical convergence with other techniques (DLS). The author of the dissertation also believes that it is too early to close the discussion about the use of different coordinate systems. In this thesis, diagonal cuts will be used, and some examples with a preference for using diagonal cuts not previously described in the literature will be shown in Chapter 4 and Chapter 6.

2.4.4 Signal-to-noise ratio of XPCS experiments

The quality of the obtained TTCs depends on the signal-to-noise ratio (SNR) for the autocorrelation function g_2 [63]. It can be calculated via [246]:

$$\text{SNR} = \beta \cdot I_{\text{pix}} \cdot \sqrt{N}, \tag{2.15}$$

with

$$N = N_{pix} \cdot N_{\text{Image}} \cdot N_{rep}. \tag{2.16}$$

Here, I_{pix} is the average intensity per pixel, β is the contrast, N_{pix} is the number of pixels, N_{Image} is the total number of frames taken during the XPCS experiment and N_{rep} is the number of repetitions of the experiment. The dependence of the SNR on the experimental parameters was established in [63] and Equation (2.15)

can be modified as:

$$\text{SNR} = \beta(a, \lambda, R) \times I_{\text{pix}}(\lambda, R) \times [N_{\text{fr}}(a, \lambda) \times N_{\text{pix}}(\lambda, R) \times N_{rep}]^{1/2}, \qquad (2.17)$$

where a is the beamsize, R is the sample-to-detector distance, and λ is the wavelength. The I_{pix} is proportional to the incoming coherent flux, Φ_c, which can be defined as:

$$\Phi_c = B\frac{\lambda^2}{4}, \quad \text{where} \quad B = \frac{\Phi_0}{4\pi^2 \epsilon_x \epsilon_y}. \qquad (2.18)$$

Here, B is the source brilliance, Φ_0 is the total incoming flux, and ϵ_x and ϵ_y are the emittance in horizontal and vertical beam direction, respectively.

Therefore, one of the simplest routes to increase the SNR is the increase in the incoming coherent flux, Φ_c. Unfortunately, if the sample is radiation-sensitive, this approach may lead to degradation or denaturation of the system due to exceeding the critical dose D_c (see Section 2.5). In order to use the increased coherent flux for bio-XPCS experiments, the experimental setup should be adapted in terms of focusing, photon energy, and sample-to-detector distance. The detailed information about this procedure can be found in [63]. The main conclusions are presented in Section 2.5.2.

2.5 Radiation damage

The previous sections showed that X-ray scattering is a powerful tool for accessing information about the kinetics and dynamics of the sample. Nevertheless, for many techniques, highly-brilliant X-rays sources are required. Unfortunately, the extremely high X-ray doses may cause significant degradation of the sample, known as radiation damage. This effect alters and subsequently destroys the sample. Biological samples, which are of interest to the current thesis, are particularly susceptible to radiation damage.

This section provides a basic overview of the radiation damage issue. At first, the interaction of X-rays with matter is discussed. Then, this knowledge is applied to the possible processes which lead to radiation damage in biological samples. Next, it is shown how to calculate the applied X-ray dose during the experiment. Finally, the possible procedure for bio-XPCS experiments is

discussed.

2.5.1 Interaction of X-rays with matter

The X-ray beam exposed to the sample may be absorbed, scattered, or pass through the material without interaction. The interaction of X-rays with matter has five components: photoelectric effect, elastic scattering, Compton scattering, pair production, and nuclear interactions. The signal we are studying during XPCS-USAXS experiments refers to elastic scattering, which was discussed in Section 2.1. A detailed overview of other phenomena with the information about corresponding cross-sections can be found in [247]. For attenuation of photons in the XPCS energy range, the photoelectric effect and Compton scattering are the most critical interactions.

The X-ray photon is totally absorbed during the photoelectric effect, and a lower level core electron is ejected from the atom. The frequency of radiation should exceed the binding energy of a given shell, which is specific to the type of material. Then, the ionized atom can emit a characteristic X-ray or an Auger electron. The photoelectron absorption may be dominant for energies of up to 500 keV and atoms of high atomic numbers.

During the Compton effect, the incoming photon is scattered incoherently on an electron, passing a small amount of energy to it. This effect also leads to the ionization of atoms. The Compton scattering is important for low atomic numbers and energies in the range of 100 keV - 10 MeV.

The probability of the described effects is related to their cross-section. Figure 2.6 shows the energy dependence of the cross-section for the different X-ray interactions with water [248]. XPCS-USAXS experiments, which are discussed in this thesis, were performed at an energy of 8.54 keV and 12.48 keV. It can be seen that the photoelectric effect is dominant in this energy range, while the probability of elastic scattering is one order of magnitude smaller. The high probability of the photoelectric effect or Compton scattering may result in the occurrence of radiation damage. In addition to the production of high-speed electrons, these types of interactions may lead to a generation of ions, secondary ionization events, and free radicals. Thus, they can significantly damage the molecular structure of soft-matter materials.

Radiation damage is one of the remaining bottlenecks for investigations of
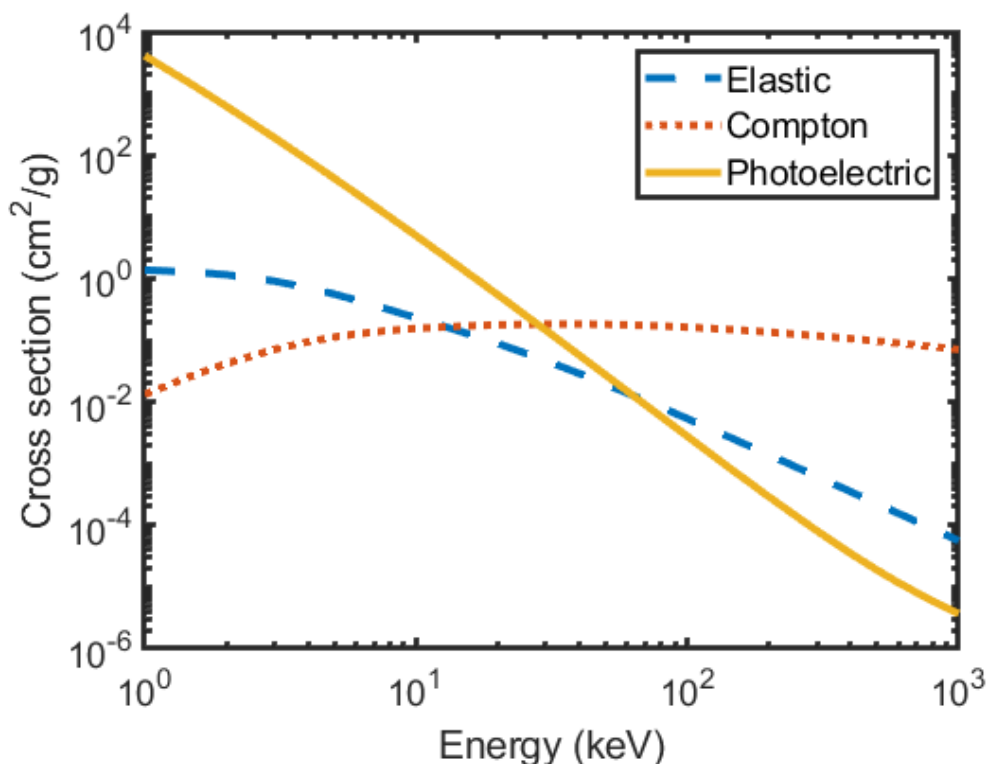
Figure 2.6: Cross-sections of the photoelectric effect (yellow), elastic (blue), and Compton (red) scatterings for different energies. The dependency is calculated for water; data is taken from [248].

kinetics and dynamics of biological objects [249, 250]. Under the extreme beam, the primary damage to the biological sample happens in the femtosecond time range after the exposure. In the picosecond timescale, there is a breakage of S-H, O-H, N-H, and C-H bonds and the formation of reactive species (solvated electrons, hydrogen, and hydroxyl radicals within the spur). In the microsecond to millisecond time range after the exposure, the breaking of bonds within a macromolecule and the formation of further radicals occur. With the exception of rare techniques for structural studies with FELs [251, 252], more than a few femtoseconds of sample exposure are required. In this case, the possible radiation damage should be taken into account.

To quantify the beam damage effects, the X-ray dose D can be calculated [63, 253]:

$$D = \frac{E}{m},$$

where E is the energy absorbed by the sample, and m is the mass of the sample. The unit the for dose is Gray: $[D]$=Gy=J/kg. For USAXS-XPCS experiments, it can be rewritten as:

$$D = \frac{\Phi_0 \cdot E_{ph} \cdot A(E_{ph}, d) \cdot \phi \cdot t_{\text{total}}}{V_{irr} \cdot \rho}. \tag{2.19}$$

Therefore, the absorbed dose can be presented as a function of the incident photon flux Φ_0, photon energy E_{ph} of the incident beam, the sample absorption A (at this energy and sample thickness d), volume fraction ϕ of the protein, its density ρ, total accumulated exposure time t_{total}, and the exposed sample volume V_{irr}.

2.5.2 Realization of low-dose XPCS experiments

Until recently, the XPCS experiments with protein solutions seemed to be impossible because of the radiation damage problem. The required X-ray dose for XPCS experiments is in the order of MGy and beyond [250], which affects the dynamics even in hard condensed matter samples [62]. The typical critical X-ray dose for protein solutions ranges from 7-10 kGy (for BSA) to 0.3 kGy (for Rnase). Exceeding this dose leads to a visible degradation of the USAXS (SAXS) patterns [60, 64], indicating an increase in the radius of gyration mostly due to aggregation. In order to avoid beam damage in protein crystallography, cryogenic cooling is used, but this approach is impossible for studying the dynamics when proteins are in solutions.

The issue of radiation damage in bio-XPCS experiments is addressed in [63, 224]. To avoid radiation damage, the sample should be exposed for a shorter time than the beam damage threshold (Equation (2.19)). The resulting challenges of the experiment can be divided into three components.

1. In order to be able to analyze the resulting TTCs, the SNR should be sufficient (Equation (2.15)).

2. In the case of LLPS phenomena, we want to investigate long processes.

3. For non-equilibrium systems, there should be enough shots (number of frames N_{Image}) to calculate TTCs. Usually, the order of this parameter is set to several thousand.

Taking into account typical critical doses for proteins and the dependency of SNR on the coherence, beam size, sample-to-detector distance, and photon energy, it was proved that with the modern updates of the experimental setups, it is possible to perform bio-XPCS experiments below the beam damage [63]. For example, the beamlines P10 at DESY in Hamburg and ID02 at ESRF in Grenoble have sufficient beam coherence for XPCS-USAXS experiments. In the SAXS range, the SNR of one image is too small for further investigation. In this case, to increase the SNR, the repetition of the experiments is performed (increase in N_{rep}). Typically, the maximum experimentally achievable beam damage threshold for these beamlines in USAXS mode is a few seconds (calculation details will be discussed later). Thus, to obtain enough points in TTC (equal to N_{frames}), the exposure for one shot should be of μs order. Then, for the investigation of long processes, the delay time between shots is added. Such an experimental procedure requires fast detectors and shutters.

Therefore, despite the almost 30-year-old history of XPCS, the experiments on biological samples became possible only a few years ago with the improvement in the experimental setup.

Chapter 3

Experimental

3.1 Materials and sample preparation

In this chapter, the materials used for the preparation of the investigated samples are discussed, and the sample preparation procedure is explained. The samples were prepared following the protocols established in earlier studies [46, 49, 147].

The protein used in this thesis work is bovine serum albumin (BSA). BSA is a globular protein derived from cows with molecular weight of 66 kDa. It consists of 583 amino acid residues and reflects an ellipsoid form factor with hydrodynamic dimensions of 140x40x40 Å, as reported in the literature [254–256]. BSA contains about 55% helix and 45% disordered structure as reported by [257]. Albumin plays a major role in maintaining plasma pressure. Due to the structural similarity with human serum albumin (HSA), BSA has been studied to a great degree as a model protein.

For the present study, BSA was purchased from Sigma-Aldrich (Product no. A7906, declared purity $\geq 98\%$). To prepare the protein stock solution, the required mass of BSA was dissolved in ultrapure degassed Milli-Q water (Merck Millipore, the resistivity of 18.2 MΩ·cm). The mass protein concentration of the stock solution was usually in the range of 300-400 mg/mL. The exact concentration value was measured using UV absorption spectroscopy at the wavelength of 280 nm using Varian Inc. Cary 50 UV-Vis spectrophotometer [46, 144], now Agilent Technologies, California, USA. The extinction coefficient of BSA used to determine the concentration from the absorption is 0.667 mg^{-1}mlcm^{-1}.

To induce short-range attractive interactions among the protein molecules, yttrium chloride (YCl$_3$) salt was introduced to the aqueous solution of protein. BSA in the presence of YCl$_3$ has been shown to exhibit LCST via LLPS. The

yttrium cations are found to bind with the proteins via endothermic entropy-driven process resulting in the LCST behavior due to the entropy-drive attraction [44].

YCl$_3$ was purchased from Sigma-Aldrich (Product no. 451363, declared purity $99.9 - 99.99\%$). The salt stock solution was prepared by weighing the required amount of salt and mixing it with the ultrapure degassed Milli-Q water (Merck Millipore, the resistivity of 18.2 MΩ·cm) according to the desired concentration (typically 200 mM). Preparation of the stock solutions of salt and protein was performed at room temperature. The protein solution was homogenized for 1 day at 4°C.

For this thesis work, the stock solutions of protein and salt were mixed at 21 °C by adjusting the concentrations of protein and salt with pure Milli-Q water so that the final protein concentration was 175 mg mL^{-1} and salt concentration was 42 mM (two-phase regime of the phase diagram [46, 49]). During the LLPS, the protein solution phase separates into a dense and a dilute phase. The phase diagram of this model system was shown in Section 1.4.2 in Figure 1.5 indicating two critical concentrations of YCl$_3$, c* and c**, within which such a phase transition occurs. Macroscopic phase separation and the following sedimentation process may take up to several days. During this process, the phase separated solution should be strictly kept at the desired temperature (21 °C) for the purpose of the completion of phase separation. After the complete phase separation of the solution, the dense phase was taken for further investigation.

Further details on the system as well as the sample preparation for other conditions of the phase diagram can be found in [44, 46, 49, 147, 258, 259].

3.2 Experimental setup

XPCS experiments discussed in this thesis have been conducted at the P10 beamline at PETRA III in DESY and the ID02 beamline at ESRF. This section provides information about the experimental setups of these beamlines. Furthermore, the experimental parameters and procedure of XPCS-USAXS experiments on LLPS systems are discussed.
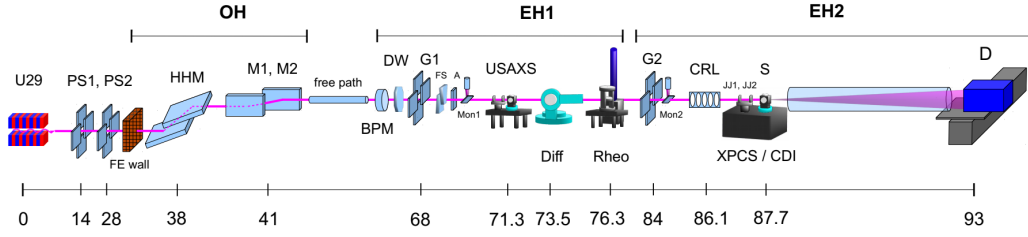
Figure 3.1: The layout of the Coherence Applications Beamline, PETRA III, DESY. The beamline is divided into three parts: optical hutch (OH), first (EH1), and second (EH2) experimental hutches. The main components of the beamline are the undulator (U29), power slits (PS1 and PS2), a high heat load monochromator (HHM), mirrors M1 and M2, guard slits G1 and G2, fast shutter (FS), the sample chamber, and the detector. The figure is adapted from [260], where further information can be found.

3.2.1 Instruments for coherent X-ray scattering experiments

The previous sections mentioned that performing XPCS experiments on biological samples requires an advanced experimental setup. Since all experiments discussed in the thesis are performed in the USAXS geometry, the P10 beamline will be used as an example to explain the basic concept of the XPCS beamline.

The principal scheme of the *P10 - Coherence Applications Beamline* at PETRA III (DESY) is presented in Figure 3.1. The beamline starts with the undulator (U29). It provides the synchrotron radiation at the beamline with a brilliance of:

$$B = 4 \cdot 10^{20} \frac{\text{Photons}}{\text{smm}^2\text{mrad}^2 0.1\%\text{BW}} \quad \text{at} \quad E = 8\text{keV}.$$

The beam shape after the undulator is defined by two power slits (PS1 and PS2). The beamline contains three sections: the optical hutch (OH), the first (EH1), and the second (EH2) experimental hutches.

In the optical hutch, there are two grazing incidence mirrors (M1 and M2) and a two-bounce Si(111) high heat load monochromator (HHM). The monochromator HHM reduces the bandwidth to $\Delta\lambda/\lambda \approx 10^{-4}$, which leads to the corresponding increase in the longitudinal coherence length (Equation (2.6)). The mirrors M1 and M2 are installed in order to suppress higher harmonics of the undulator spectrum.

In the first and the second experimental hutches, there are guard slits G1 and G2, respectively, which block parasitic scattering. To focus the beam and reduce the beam size on the sample, compound refractive lenses are used (CRLs). For
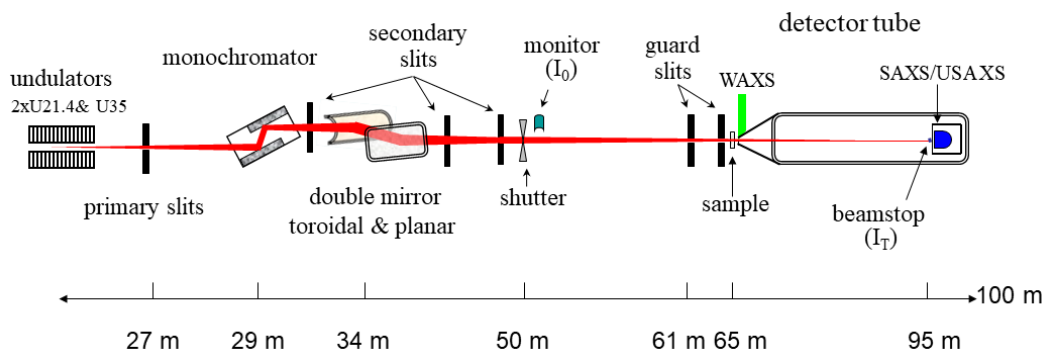
Figure 3.2: The layout of the Time-Resolved Ultra Small-Angle X-ray Scattering Beamline, ESRF [261].

the USAXS geometry, the sample chamber was installed in the EH1. To perform experiments with the delay times in the microsecond range, special fast detectors are required. The XPCS measurements discussed in this thesis were conducted with an EIGER 4M detector located in the EH2. To block the direct beam and prevent overexposure of the detector, a beamstop was installed.

The temperature control of the sample is performed by the Linkam stage. The sample of 1.5 mm diameter is mounted inside of the Linkam. The stage is able to change the temperature of the sample with the heating (cooling) rate up to 150 °C/min. The heating is provided by electronic heating, while for cooling liquid nitrogen is used.

Another beamline used for the XPCS experiments is *ID02 - Time-Resolved Ultra Small-Angle X-ray Scattering Beamline* at ESRF. Its principal layout is shown in Figure 3.2. The basic concept of the beamline is similar to the described P10 example. The detailed information can be found in [261]. The Linkam stage at ID02 has a 1 mm slot for the sample capillaries, and the heating rate has its maximum at 110 °C/min. The measurements were performed using an EIGER 500k detector [262].

3.2.2 Experimental parameters and procedure

The primary parameters of the experiment were chosen according to the most advantageous combination of the SNR, the q-range of interest, and the estimated beam damage threshold (D = several kGy). Then, the sample-to-detector distance and the energy were fixed, and the beam damage test was performed to adjust the rest of the parameters.

Table 3.1: Beamline parameters for XPCS experiments. R is the sample-to-detector distance, E is the photon energy, a is the beamsize, and Φ_c is the final X-ray flux.

beamline	R (m)	E (keV)	a (µm)	Φ_c (10^{10}phs^{-1})	detector
P10	21.2	8.54	100×100	0.3	EIGER 4M
ID02[1]	30.7	12.46	35×35	3.2	EIGER 500k
ID02[2]	30.7	12.28	22×25	0.12	EIGER 500k

For the beam damage test, the sample was equilibrated at $10\,°C$. Subsequently, the study of X-ray-induced changes to the static USAXS pattern of the homogeneous sample was performed to define the threshold of maximum photon density and of exposure time. The sample was continuously exposed, and the changes in the intensity profile $I(q)$ were monitored. The starting time of the changes in the scattering pattern was considered as the maximum exposure time, $t_{threshold}$, at the current setup. Assuming that for an accurate TTC, at least 600 frames are required, the exposure time t_{exp} per frame was calculated:

$$t_{exp} = t_{threshold}/N_{frames}.$$

Taking into account the total time of interest for the experiment T_{total}, the required delay time t_{delay} was defined using the equation:

$$T_{total} = (t_{exp} + t_{delay}) \times N_{frames}.$$

If t_{exp} or t_{delay} are less than the time required for the fast shutter or the readout time of the detector, the beam damage test should be repeated under the setup with a decreased flux. For example, the fastest frequency to collect images by the EIGER 4M detector is 750 kHz. Its readout time is 10 μs. In P10, the reduction of flux is achieved by the installation of silicon wavers as absorbers to attenuate the incident beam [260]. In ID02, the change in the beam size is used for this purpose [261].

The final beamline parameters used for XPCS experiments are presented in Table 3.1. Labels ID02[1] and ID02[2] correspond to different beamtimes at the ID02 beamline. Information about the delay and exposure times and the total number of frames for each specific measurement will be given when describing them in Part II.

Part II

Results and discussions

Chapter 4

Interplay between kinetics and dynamics of LLPS in a protein solution revealed by XPCS

The following chapter is based on [220]. The experiment was conducted in collaboration with the group of Prof. Dr. Christian Gutt of Siegen University. Reprinted with permission from J. Phys. Chem. Lett. 2021, 12, 30, 7085–7090 . Copyright 2021 American Chemical Society.

4.1 Introduction

LIQUID-LIQUID phase separation (LLPS) is a fundamental process that has significant consequences in many biological studies, e.g., investigations of protein crystallization [41], bio-materials, and diseases [40], as well as for food [39] or pharmaceutical industry [38]. In cells, LLPS can play a crucial role in driving functional compartmentalization without the need for a membrane and as a ubiquitous cellular organization principle implicated in many biological processes ranging from gene expression to cell division [12, 15, 263]. LLPS is a complex process involving domain evolution of the new phases, microscopic dynamics of density fluctuation, and the thermal fluctuation of domain interfaces, as well as global diffusive motion. While both the kinetics of domain evolution and the microscopic dynamics are important for the formation and properties of the various condensates, research so far mainly focused on the domain growth kinetics and the dynamics remains largely unknown.

Dynamics of a system in equilibrium can be described using the fluctuation of the static structure factor, $S(q)$, where the average density is constant and $\rho(t)$ fluctuates around this mean value. In this case, $\overline{S(q)}$ is constant and dynamics can be directly extracted. For a system undergoing phase separation, the interplay between dynamics and kinetics may lead to a more complex scenario, i.e., the temporal average density (and accordingly, $\overline{S(q)}$) changes and fluctuates at the same time. At the late stage of LLPS via SD, theoretical studies have shown that the domain coarsening follows dynamic scaling, i.e., during domain evolution, the domains remain essentially statistically self-similar at all times [264]. As a result, $\overline{S(q)}$ does not change if the measurements are performed at length scales corresponding to the average domain size [234, 239]. Thus, in principle, the time-dependent fluctuations of $S(q)$ can be described by the two-time intensity covariance, which equals the square of the two-time structure factor under the "Gaussian decoupling approximation" [234, 239]. Therefore, domain coarsening dynamics can be accessed by calculating the speckle-intensity covariance [234, 239].

However, the early stage of LLPS is much more complex because the time-dependent $S(q, t)$ cannot be described by dynamic scaling. The interplay between kinetics and dynamics makes a quantitative description of the microscopic dynamics challenging. So far, despite the substantial process in kinetic growth studies [112, 265], such a theory to predict or an experimental method to probe the dynamics in the early stage of SD is missing. Nevertheless, the dynamic property of LLPS is a vital input to predict the dynamic properties of the resulting condensates in biological systems. Studies of LLPS in cells have shown that the exact biological function of the resulting condensates strongly depends on their dynamic properties, such as a dense liquid, a gel, or a glassy state [12]. Therefore, detection in the early stage of the condensates is needed, which requires a characterization of the dynamics of LLPS. Furthermore, as LLPS in cells is generally triggered by a gradient of constituents instead of a temperature quench, the dynamic properties of LLPS also reflect the material transport in the crowded environment of a multi-component system.

Despite the recent progress in the field of phase separation [12, 89], the interplay between the kinetics and dynamics at the early stage remains elusive. What is the influence of the change of $S(q)$ with time on dynamics? Whether one can distinguish the kinetic and dynamic contribution experimentally? What are the

main features of dynamics in the early stage of LLPS? In principle, both domain growth kinetics and microscopic dynamics of fluctuations of the interface of the domains of LLPS can be simultaneously accessed experimentally using X-ray photon correlation spectroscopy (XPCS). The XPCS investigation of the fluctuations during the late, domain coarsening, stage was demonstrated vividly by the work of Malik et al. in a sodium borosilicate glass [238]. Microscopic dynamics of systems undergoing phase transition displays rich non-equilibrium behavior on length scales ranging from micrometer to single-protein size and on time scales from hundred of seconds down to microseconds [266]. XPCS has been used in different soft condensed matter systems [56, 58, 59, 219]. However, due to experimental difficulties in working with beam-sensitive samples [60–62], XPCS of protein-based systems became possible only recently with a special experimental procedure design [63, 64, 222, 223].

In this chapter, we focus on the dynamics during the early stage of the spinodal decomposition. The observed dynamics come from the large-scale density fluctuation and the movement of the interface of the domains [239]. Consequently, the dynamics from the equilibrium mixed or demixed bulk phases do not contribute much due to the low contrast and signal-to-noise ratio [224]. We apply state-of-the-art XPCS in the ultra-small angle scattering (USAXS) geometry to investigate the domain evolution and microscopic dynamics during LLPS in aqueous protein solutions. The system consists of the globular protein bovine serum albumin (BSA) in the presence of trivalent salt yttrium chloride (YCl$_3$) [44, 46]. The phase behavior of this system has been established to exhibit a lower critical solution temperature (LCST) phase behavior [44, 46, 135]. The phase diagram of the LLPS binodal has been established [44, 46] and the kinetics of LLPS of this system has been well studied using USAXS [45, 46]. Here we aim to explore both the growth kinetics and the microscopic dynamics in order to distinguish their roles in the early stage of LLPS and the domain coarsening using XPCS in the USAXS geometry. Combined with 2D Cahn-Hilliard simulations, we demonstrate that the dynamic information can be distinguished from the growth kinetics with a factor of ~ 40 difference in time scales. The method established in this work can be used to access the dynamics during phase transitions in a broad range of soft matter and biological systems.

4.2 Experimental parameters

XPCS experiments were performed in USAXS mode at PETRA III beamline P10 (DESY, Hamburg, Germany) at an incident X-ray energy of 8.54 keV (λ = 1.452 Å) and beam size of $100~\mu m \times 100~\mu m$. The sample-to-detector distance was 21.2 m, which corresponds to a q range of 3.2×10^{-3} nm^{-1} to 3.35×10^{-2} nm^{-1}, where $q = 4\pi/\lambda \cdot \sin\theta$ and 2θ is the scattering angle. Taking signal to noise ratio and beamstop into account, the q range for the XPCS data analysis is from 3.5 to $11.2~\mu m^{-1}$. The data were collected by an EIGER X 4M detector from Dectris with $75~\mu m \times 75~\mu m$ pixel size.

The BSA and YCl$_3$ sample was prepared according to Section 3.1. The solution was filled into capillaries of 1.5 mm in diameter and first equilibrated at 10 °C for 10 minutes. Then, it was heated with a Linkam heating stage to 40 °C with a rate of 150 °C/min. The system was followed from the beginning of the temperature change. The measurement was performed twice, once with high temporal resolution and a total measurement time of 60 s, and a second time with lower temporal resolution but longer total measurement time, for a total of 312 s. After each measurement, the solution was cooled back to 10 °C. This condition corresponds to a spinodal decomposition based on the kinetic studies [46]. Each measurement was taken on a fresh sample spot separated by a larger than the beam size distance from the previous one to avoid the beam damage due to the long exposures. The number of frames, exposure time, and delay time (Table 4.1) were calculated based on the beam damage test, which was done preliminary to all measurements. The sample was measured with different attenuators at 10 °C, so we checked the behavior of the sample under the beam in the one-phase regime. The time of survival of the sample was considered as time with no change in USAXS profile and simultaneous noise in TTC and equaled to 60 s under the flux 1.42×10^9 ph/s, which was taken into account for all further measurements. The temperature of the sample was recorded every 2 seconds. First 60 s and 312 s experiments were done under different exposure parameters (while under the beam damage threshold). However, the overlapping period demonstrated the same kinetics and dynamics, which is additional evidence for selecting the beam parameters that do not affect the sample.

A series of 2D speckle patterns were obtained, which contains the dynamic information of the investigated sample. The same 2D scattering patterns were

Table 4.1: Experimental parameters

Duration (s)	Number of frames	Exposure (s)	Delay (s)	~ Time of average (s)
60	7500	0.008	0	0.08
312	3000	0.004	0.1	1

used for the investigation of kinetics. To obtain the USAXS profile $I(q)$ for each frame (time), the scattering intensity was azimuthally averaged for different radii and the profile collected before the heat was used as the background.

4.3 Results and discussions
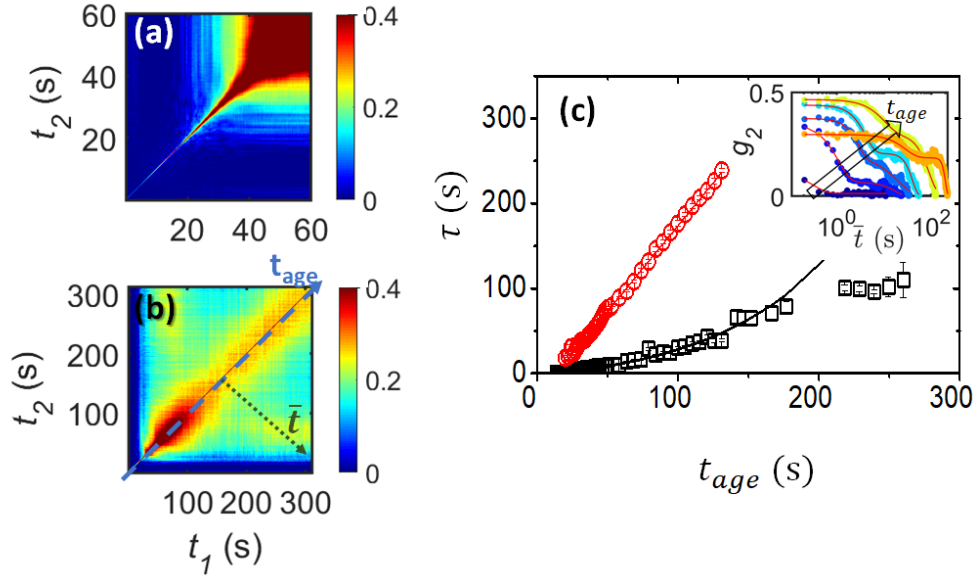
4.3.1 Experiment

The time-resolved 2D speckle patterns collected in XPCS measurements are analyzed using a two-time correlation function (TTC) $G(q, t_1, t_2)$ [225]:

$$G(q, t_1, t_2) = \frac{\overline{I(t_1)I(t_2)} - \overline{I(t_1)} \cdot \overline{I(t_2)}}{[\overline{I^2(t_1)} - \overline{I(t_1)}^2]^{\frac{1}{2}} \cdot [\overline{I^2(t_2)} - \overline{I(t_2)}^2]^{\frac{1}{2}}}, \qquad (4.1)$$

where the average is over pixels with the same momentum transfer $q \pm \Delta q$ (calculated for q from 3.5 to 11.2 μm^{-1}). Here t_1 and t_2 are the times at which the intensity correlation is calculated.

Typical results of TTC are presented in Figure 4.1. In the TTC of the system in the first 60 s after the start of the temperature change, a relaxation signal appears a few seconds after the temperature jump, initially with a fast decay rate, but quickly broadening with t_{age}. The TTC of the first 312 s shows that the main relaxation along the diagonal turns into a steady state after the quick broadening. A new slow relaxation mode gradually appears (Figure 4.1 (a)), and its correlation shows a decay, leading to a square-like feature in the TTC. This feature is most likely caused due to the formation of the domains. The physical phenomena underlying TTC features are outside the focus of this chapter and will be discussed in details in the Chapter 5.

Figure 4.1: Two relaxation modes revealed by XPCS. **(a)** TTC for the first 60s and **(b)** 312s after a temperature jump from $10\,^\circ$C to $40\,^\circ$C for 312 s experiment at $q=4.4\mu m^{-1}$. The colorbar corresponds to the $G(q, t_1, t_2)$ values. The slow mode describes the sudden decay in correlation in **(b)** around 20-30s, exhibiting a square feature in TTC. Blue long-dash line shows the direction of the increase of experimental time t_{age}, and the short-dash line displays the direction of the g_2-cuts. The inset of **(c)** shows g_2 obtained from **(b)**. **(c)** Relaxation time τ evolution as a function of t_{age} for fast (black squares) and slow (red circles) modes at $q=4.4\mu m^{-1}$. τ of the fast mode follows an exponential growth (black solid line) before 200s, whereas τ for the slow mode grows linearly with time (red solid line).

The correlation function, $g_2(q, t_{age})$, can be determined by both horizontal and diagonal cuts from the TTC [232]. Here we focus on the diagonal ones to resolve all interesting features of TTC including the "square". For comparison, the results of horizontal cuts are shown in (Figure 4.2). $g_2(q, t_{age})$ functions can be fitted using the Kohlrausch-Williams-Watts (KWW) relation to determine the characteristic relaxation time (τ) and the shape parameter (γ) [267] as functions of q and t_{age}. As we can see in the inset of Figure 4.1 (c), the $g_2(q, t_{age}, \bar{t})$ functions display two-decay relaxations - a fast and a slow mode, which can be modelled using two exponential decay functions:

$$g_2 = \beta_1 \exp(-2\left(\frac{\bar{t}}{\tau_1}\right)^{\gamma_1}) + \beta_2 \exp(-2\left(\frac{\bar{t}}{\tau_2}\right)^{\gamma_2}), \tag{4.2}$$

where the index 1 corresponds to the fast component and the index 2 to the slow component of the relaxation. The parameters τ and γ are functions of both q and
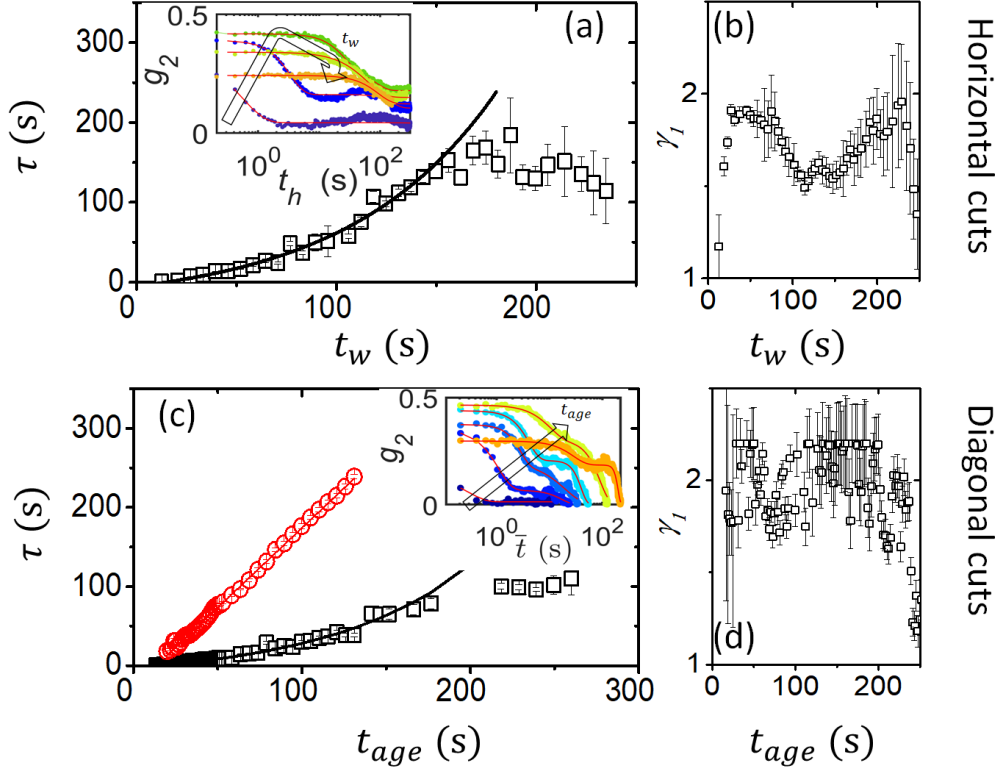
Figure 4.2: Horizontal (a, b) and diagonal (c,d) cuts of TTC map at $q=4.4\mu m^{-1}$. Relaxation time temporal evolution is demonstrated in (a) for horizontal cuts and in (c) for diagonal cuts with the g_2 in the insets. The fast component (black squares) show an exponential growth (black solid line) followed by the modulation around constant value independently from the coordinate system type. However, the diagonal cuts also include the information about the slow mode, which relaxation time is plotted with red circles on (c). The shape parameter γ_1 of fast mode is shown in (b) and (d) and demonstrates the fluctuation around 2. Due to the difference in the coordinate system type, the time notions used for horizontal and diagonal cuts are different. For horizontal cuts the g_2 at different waiting time t_w is extracted by taking the line along t_1 or $t_2 = constant$ with the delay time t_h given by $|t_2 - t_1|$. For diagonal cuts the g_2 at different sample age $t_{age} = (t_1 + t_2)/2$ is extracted by taking the line perpendicular to the $t_1 = t_2$ with the delay time $\bar{t}$ given by $|t_2 - t_1|$ [232].

t_{age}. Here $\bar{t} = t_2 - t_1$ is a delay time, t_{age} is the time that passed from the start of the heating, $\beta(q)$ is the speckle contrast, which can vary from 0 (incoherent scattering) to 1 (fully coherent scattering) for ergodic processes. The g_2 functions were averaged over a small range of time t_{age} to increase the signal-to-noise ratio (Table 4.1).

Relaxation times, τ_1 and τ_2, extracted from the KWW fits are shown in Figure 4.1 (c). The fast mode exhibits two distinct stages of the evolution of relax-
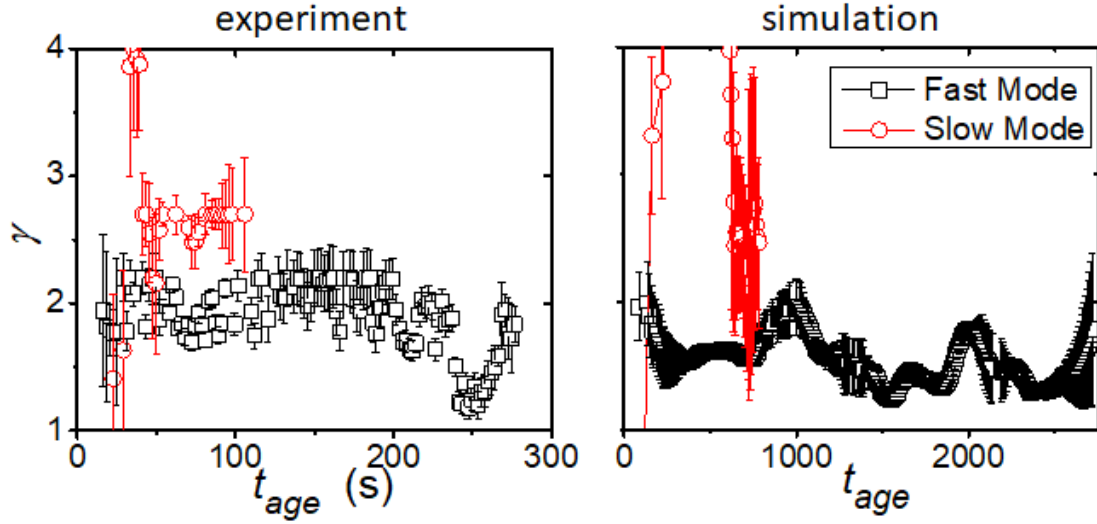
Figure 4.3: Shape parameter γ evolution with t_{age} for fast (black squares) and slow modes (red circles) of dynamics for experiment and Cahn-Hilliard simulation.

ation time: initially ($t_{age} < 150$ s), the value τ_1 increases exponentially, followed by fluctuations around $\tau_1 \sim 100$ s in the later stage of the experiment (Figure 4.1 (c)). Similar two-stage behavior has been reported in XPCS investigations of Wigner glasses [193], glassy ferrofluids [268], and egg-white [222] and has been suggested as a general feature near the glass transition as well as gelation. The results of the horizontal cuts are consistent (Figure 4.2). It is important to note that the behavior of the fast component does not show the dynamic arrest that is typically characteristic of the glass transition [97, 269]. Thus, the observation of two-stage behavior is not sufficient evidence for the presence of gelation in the sample, and others must be sought. We will return to this issue in the Section 5.2.4.

The slow mode corresponds to the broad square-like feature observed in the TTC in Figure 4.1 (b). The relaxation time of the slow mode linearly increases as a function of t_{age}. The shape parameter γ_2 of the slow mode shows a jump in the early stage from values less than 2 to higher ones and then fluctuates at values around 2.7 (Figure 4.3 (a)). Such high values indicate that there are different phenomena taking place in the early and later stages, and these stages hardly correlate with each other. Based on a comparison of the behavior of the $\overline{S(q)}$ for the experiment and simulation and matching with the real-space picture (presented later in Section 4.3.2), it seems that the appearance of the slow mode correlates with the transition from the density fluctuation to the coarsening.
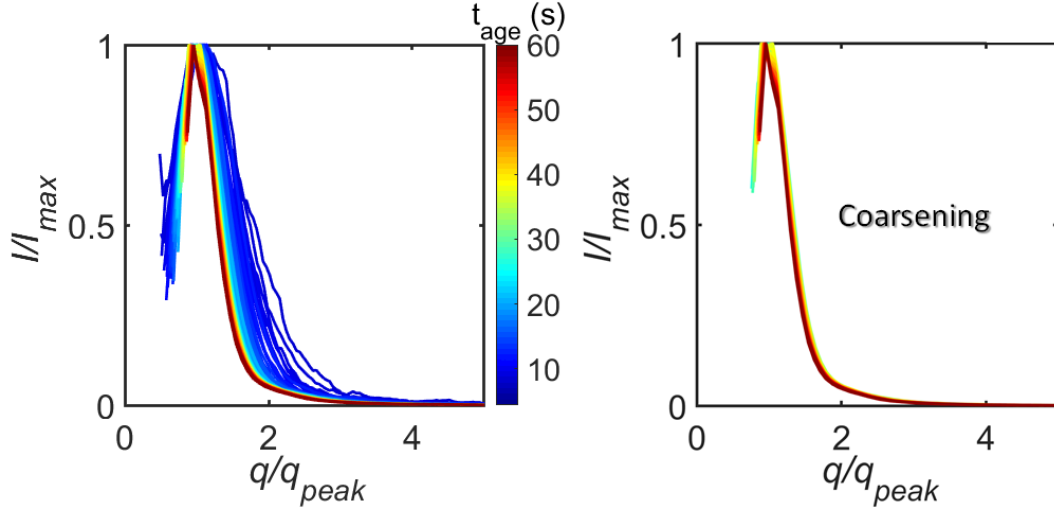
Figure 4.4: Application of scaling to the scattered intensity curve for different experimental times t_{age}. The scaling law is not valid for the early stage of SD (~ 24 s): the normalized curves do not lie one on another (blue curves on the left graph). In comparison, the coarsening stage demonstrates compliance with the scaling law (right graph).

However, the study of TTC features is outside the scope of this chapter and will be presented in Chapter 5.

In the early stage of LLPS, due to the strong coupling between domain growth and interface fluctuation, the resulting relaxation rates (Figure 4.1 (c)) may have both contributions. Dynamical scaling cannot describe the time-dependent scattering profiles in the early stage as expected (Figure 4.4). In order to distinguish or decouple the contributions, we determine and compare the kinetic relaxation rate with the XPCS results.

The evolution of a kinetic rate $\Gamma_{kinetic}$ at a specific q can be calculated through the changes in the scattering intensity $I(q, t_{age})$ [270]:

$$\Gamma_{kinetic}(q, t_{age}) = \frac{1}{2I(q, t_{age})} \frac{dI(q, t_{age})}{dt_{age}}. \tag{4.3}$$

The scattering intensity $I(q, t_{age})$ was calculated for each value of t_{age} based on USAXS experiments as the mean intensity $I(q \pm \Delta q, t_{age})$ of all pixels inside the ring $q \pm \Delta q$ (Figure 4.5 (a)), but only the absolute values of dI/dt_{age} are used for comparison. For the investigated q-region the temporal evolution of the scattering intensity is caused by the spinodal peak position shifting from high to low q-values (Figure 4.9 (a)) [45, 46].
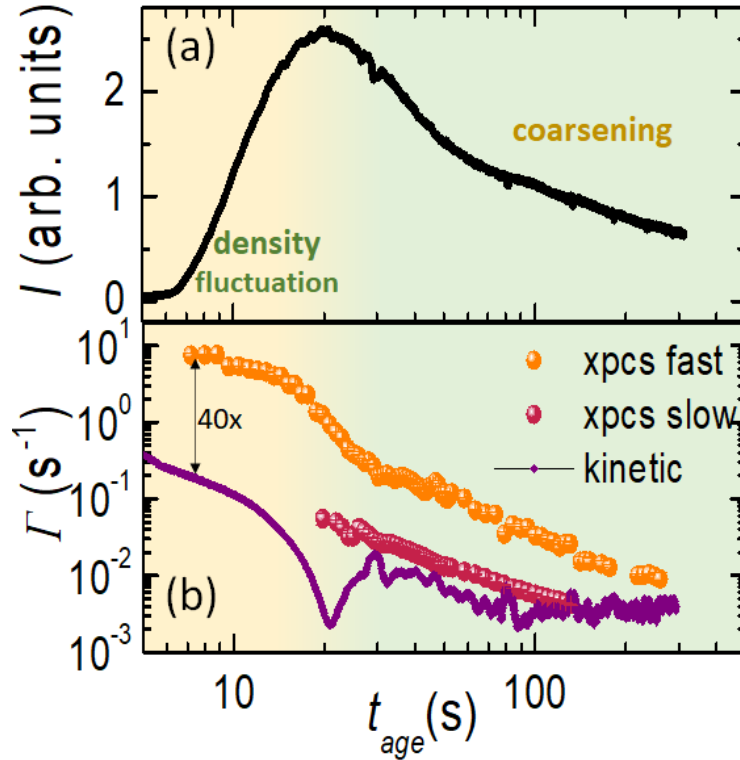
Figure 4.5: Decoupling between kinetics and dynamics. **(a)** Representative structure factor evolution with t_{age} at $q=4.4\mu m^{-1}$. **(b)** Comparison of relaxation rate for fast mode of XPCS (orange), for slow mode of XPCS (coral red) with kinetic relaxation rate (purple, obtained from USAXS) for $q=4.4\mu m^{-1}$. Yellow and green regions in **(a)** and **(b)** correspond to the density fluctuation and domain coarsening stages of LLPS, respectively.

Corresponding typical temporal evolution of $S(q)$ is shown in Figure 4.5 (a). The kinetic decay rate calculated using Equation (4.3) shown in Figure 4.5 (b) exhibits a quick decrease with aging time initially and becomes nearly a constant after about 100 s. For comparison, the decay rates of both slow and fast modes from XPCS measurements are also shown in Figure 4.5. It is interesting to see that the slow-mode decay rate is similar to the kinetics during the early stage of coarsening.

The fast mode starts at $t_{age} \sim 7$ s, before which the dynamics is too fast to be detected with the current XPCS measurements (limited by values of exposure and delay times). The decay rate is up to 40 times higher than the kinetic relaxation in the early stage and about one order of magnitude faster in most of the coarsening stage (up to $\sim 150s$). Thus, these two effects are decoupled, and the fast mode corresponds to the microscopic dynamics of the movement of
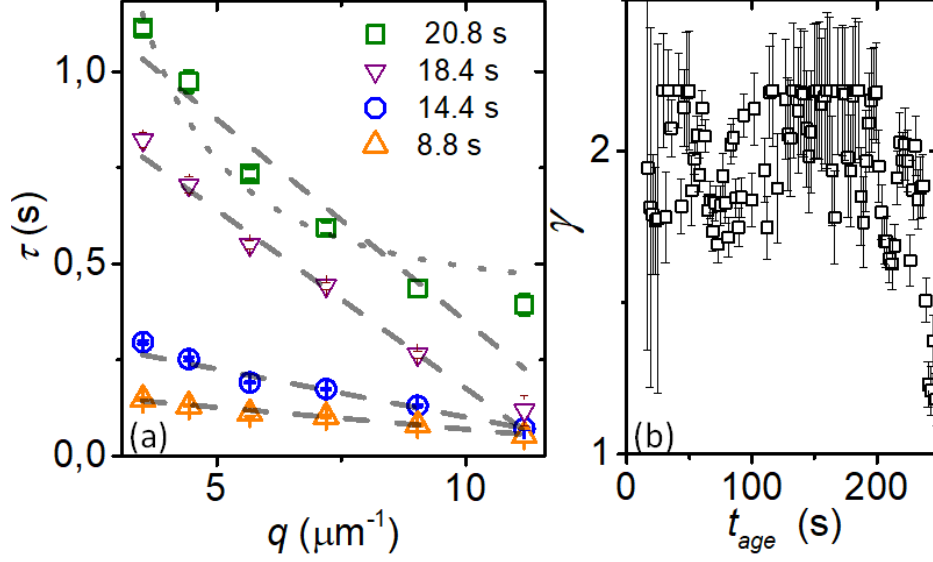
Figure 4.6: Hyper-diffusive dynamics revealed by XPCS: **(a)** q-dependent of τ and **(b)** shape parameter γ as a function of t_{age} for the fast mode dynamics of XPCS. Grey lines represent fit with $\tau \sim q^{-1}$ (dashed) and $\sim q^{-2}$ (dotted).

the interface of the domains and large-scale density fluctuations. The results are similar for other q-values in the [3.5, 11.2] μm^{-1} range.

Now we can interpret the fast mode as a reflection of the principal dynamics of the system during LLPS. The q-dependency of its relaxation time is shown in Figure 4.6 (a). In the early stage, $t_{age} < 20$ s, τ follows an inverse linear relationship with q, $\tau \sim q^{-1}$. With increasing time, it becomes non-linear with $\tau \sim$ between q^{-1} and q^{-2}. In the mean time, the shape parameter $\gamma > 1$ (Figure 4.6 (b). These results demonstrate the domain fluctuation dynamics to follow the hyper-diffusive ballistic motion in the early stage. The hyper-diffusive dynamics seems to be a rather universal behavior for systems in the non-equilibrium state ([193, 222, 268, 271]).

4.3.2 Cahn-Hilliard simulation

As discussed in the Section 4.1, during the domain coarsening step, due to the dynamic scaling effect, the covariance of the TTC is directly connected with the fluctuation of $S(q)$, i.e., the dynamics of domain fluctuation. Here we perform simulations to verify if the kinetic relaxation rate can be decoupled with the
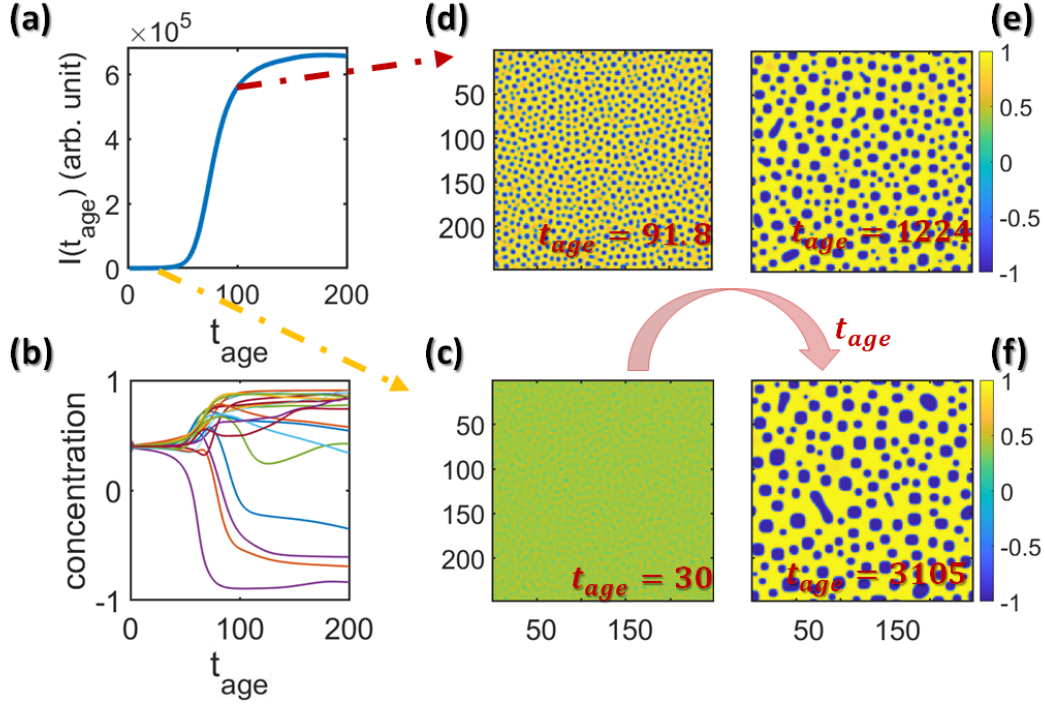
Figure 4.7: (a) Behavior of scattered intensity with t_{age} for the early stage of LLPS ($t_{age} <$200) for $T = 0.05T_c$ for simulated data for the same $q = 22 pixel$ for which Fig. 3 in the manuscript was presented. (b) Change of concentration for different random points (one point - one line) in the real space with time t_{age} during the early stage of LLPS. Time of significant change in concentration functions has a similar value to the time of jump of structure factor on (a). (c)- (f) Simulated real space pictures of the LLPS process for different t_{age} in the 256×256 pixels square. Colormap represents normalized concentration u(m,n, t_{age}) values. Yellow and Red dash-dot lines show the correspondence of the structure factor value and state of the system in the real space at the same time t_{age}.

dynamics in this stage as well. A system undergoing spinodal decomposition can be described by the Cahn-Hilliard equation (CH) [98, 99] (discussed in Section 1.3), which gives the concentration at each point of the simulated map with time. After rescaling of parameters [102] and adding a temperature jump [104], we can write:

$$\frac{\partial u(\mathbf{r}, t)}{\partial t} = \nabla \left[m(u)\nabla \left(-\frac{T_c - T}{T_c}u + u^3 - \nabla^2 u \right) \right], \qquad (4.4)$$

where $u(\mathbf{r}, t)$ - rescaled time-dependent local concentration, $m(u)$ - mobility function, T_c - critical temperature. The $u(\mathbf{r}, t)$ can take values from -1 to 1. Positive values correspond to the dense phase and negative values to the diluted
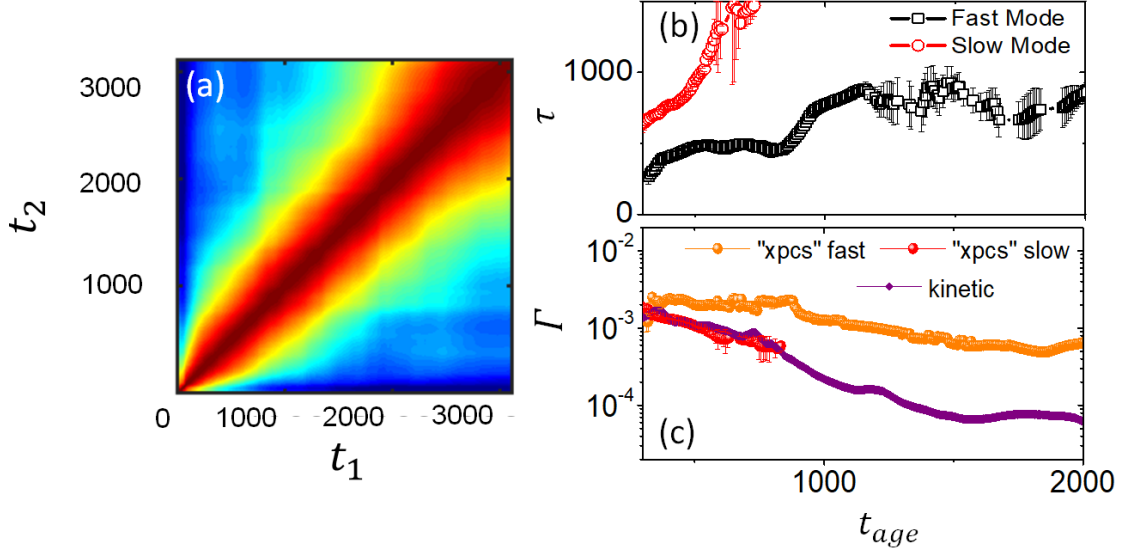
Figure 4.8: Kinetics and dynamics of LLPS simulated using CH equation: **(a)** Representative TTC for $T = 0.05T_c$ with a total simulation time of $t_{age} = 3105$. **(b)** Relaxation times of the two modes as a function of t_{age}. **(c)** Comparison of decay rates for the slow (coral red) and fast (orange) modes of dynamics with kinetics (purple) for simulated LLPS. Here $q_{simulation}$=22 pixel which is similar to the experimental $q = 4.4\mu m^{-1}$ (see Figure 4.9 **(a)** and **(c)**).

phase. For classical SD, the mobility function $m(u)$ is constant with time (set to 1).

Equation 4.4 was solved numerically [272] in 2D as described in Section 1.3.2. Space was divided in a matrix with size $N \times N$=256 × 256 pixels. The initial concentration for each point in the space was defined as random noise fluctuations with amplitude 0.05 around $u_0 = 0.4$, which corresponds to the dense phase (similar to the experiment) so that these noise fluctuations have a uniform distribution. The time step was 0.09, the total number of steps was 34500, and T was set to $0.05T_c$.

This model is coarse-grained and intentionally simplified. The goal of the simulation is to generalize the results from the specific sample. Full large-scale simulations [112, 273] are beyond the scope of this study.

Based on the simulations, the evolution of the 2D field of concentration was calculated (Figure 4.7 (c)-(f)). The speckle pattern (i.e., image in reciprocal space $I(\mathbf{q}, t_{age})$) can be determined for each time step as a "square" of the magnitude

4.3.2. Cahn-Hilliard simulation
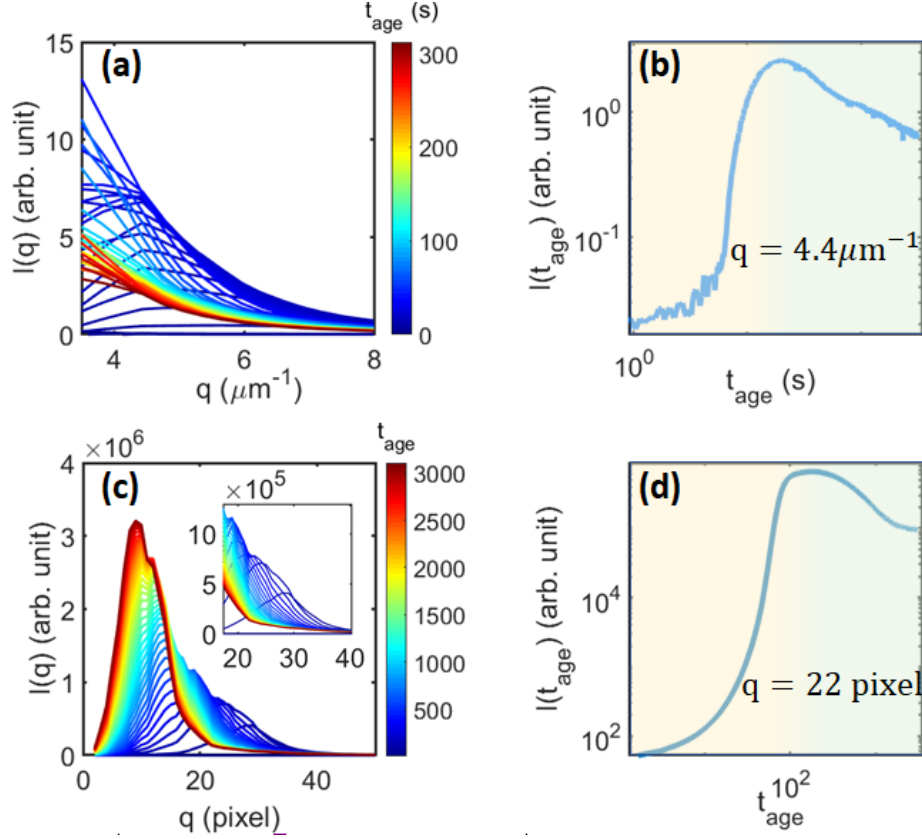
Figure 4.9: (a) Intensity profiles obtained by USAXS experiment at different experimental times t_{age} for $T = 40°C$. **(b)** Intensity at $q = 4.4\mu m^{-1}$ for $T = 40°C$. **(c)** Simulated intensity profiles obtained from Fourier transform of the real space image for $T = 0.05T_c$. In the right corner there is a zoom for $q = [20, 40]pixel$ range. **(d)** Intensity for simulated data for $T = 0.05T_c$ at $q = 22pixel$. It is clearly seen that $q = 22pixel$ of the simulated intensity profile and $q = 4.4\mu m^{-1}$ of the experimental profile have the same behavior (compare (d) with (b)) and these q-values are similar relative to the peak position of scattered intensity in the beginning (compare picture in the right corner of (c) with (a)).

of the 2D fast Fourier transform of the fluctuations of the concentration [101]:

$$I(\mathbf{q}, t_{age}) = \left| \sum_{m=0}^{N-1} \sum_{n=0}^{N-1} (u(m, n, t_{age}) - u_0) \exp\left(\frac{2\pi i}{N}(mq_x + nq_y)\right) \right|^2. \quad (4.5)$$

The outcome is similar to the 2D scattering pattern obtained via XPCS-USAXS experiments. The dynamics of the simulated LLPS process was further characterized using Section 4.3.1. The results were averaged over three simulations with different initial conditions.

The main results of the simulations are presented in Figure 4.8. They are highly dependent on the q-value. In order to qualitatively compare the simulation with

experimental data, we focus on the similar q-region in comparison to the q value of the early stage peak position of scattered intensity (Figure 4.9). The total time of the simulation was estimated from the behavior of the scattering intensity for the chosen q with time t_{age}. For the described parameters, the simulated TTC reproduces the main features of the experimental TTC (compare Figure 4.8 (a) and Figure 4.1 (b)). TTCs from the simulation also show a square feature as observed in the experimental TTC. The origin of the side features in TTCs cannot be resolved with the standard XPCS data analysis presented here. These features are outside the focus of this chapter and will be discussed in Chapter 5.

The g_2 functions from simulations also contain two relaxations, which demonstrate the existence of the two modes of dynamics in a general case. The relaxation time for the slow mode linearly increases with time (Figure 4.8 (b)). For the fast mode, it increases with a modulation before reaching a steady state. The shape parameters $\gamma > 1$ show behavior similar to the experimental results (Figure 4.3 (b)). Figure 4.8 (c) compares the relaxation rates. The relaxation rate of the slow mode obtained from correlation analysis exhibits behavior similar to the kinetics. Importantly, a simple classical model used for the current simulation of the phase transition demonstrates that the dynamics is much faster than the kinetics. This generalizes the result of time scale separation and widens its application from the specific one to a broad range of LLPS systems.

It is worth noting that the simulation does not consider thermal motion, the limited heating rate, and the viscoelastic properties of the real system. Furthermore, the classical Cahn-Hilliard simulation does not consider the gelation process. These may be the reasons for differences between experimental and simulated TTCs. This issue will be discussed in detail in Chapter 5. Nevertheless, looking ahead, it is worth speculating about the reasons for the lack of exponential growth of τ in the early stage of simulation. The early stage of LLPS is sensitive to the thermal motion [274]. According to Chapter 5, it may result in the loss of the spatial correlations, which influences the visibility of the kinetic relaxation rate (being much slower than thermal motion effects) in the TTC. Thus, the dynamics dominates in the experimental TTC. In the simulated TTC, this effect is not included, and the kinetic relaxation rate can be seen in the early stage. The influence of the thermal motion decreases with the increase of the domain sizes, resulting in the appearance of the kinetic relaxation rate in the TTC ("square" feature) and finally becomes negligible in the coarsening stage.

4.4 Conclusions

In summary, we have studied the non-equilibrium dynamics and kinetics of a protein solution undergoing a liquid-liquid phase separation using USAXS-XPCS. The results show that microscopic dynamics is up to 40 times faster in the early stage and still at least one magnitude faster in the late coarsening stage than the kinetic relaxation rate. Thus, these two components could be decoupled. In the early stage, the microscopic dynamics is not Brownian dynamics of the proteins, which would have required relaxation time $\propto q^{-2}$ and shape parameter $\gamma \sim 1$. Instead, this dynamics can be well described using a hyper-diffusive ballistic motion, i.e., the relaxation time $\propto q^{-1}$ and shape parameter $\gamma \sim 2$. Furthermore, the relaxation time of the dynamics exponentially increases with time in this early stage. In the late stage, where the domain coarsening is the main process, the relaxation time increase with time following a power law.

Cahn-Hilliard simulations support the experimental results and broaden the conclusions to LLPS phenomena in general, making our results applicable to other soft matter and biological systems undergoing a phase transition, where kinetics and dynamics are intertwined [40]. For example, LLPS in living cells leads to various types of condensates with distinct dynamic properties, such as dense liquid, gel, and glass-like states [12]. These distinct dynamic properties influence not only the kinetics of LLPS but also the material transport and their biological functions in the crowded cellular environment. Finally, we emphasize that this work can be extended to different length and time scales using XPCS in SAXS mode and the fast development of X-ray free-electron laser (XFEL) facilities, so the dynamic behavior ranging from single protein to the domain coarsening could be covered.

Chapter 5

Reverse-engineering method for XPCS studies of non-equilibrium dynamics

The following chapter is based on [275]. The experiment was conducted in collaboration with the group of Prof. Dr. Christian Gutt of Siegen University.

5.1 Introduction

SIMULATIONS can be considered the third pillar alongside theory and experiment in modern physics [276, 277] and simulations based on theoretical equations are often used to compare and rationalize the experimental results. However, this approach has limitations related to the assumptions used to derive the theory. In particular, when more complex phenomena are involved, for which a comprehensive theory is not available. In view of this, a different approach is needed, which focuses on the relation between the phenomenon and the key control parameters instead of a specific theory. For example, understanding the dynamics of proteins in solutions is extremely important for their complex phase transitions including liquid-liquid phase separation (LLPS) [278], protein crystallization [41], glass transition [95], bio-materialization [40], and as well as in food and pharmaceutical industry. The dynamic behavior of these non-equilibrium processes covers length scales ranging from single-protein size to micrometer phase domains and time scales from microseconds to hundreds of seconds [46, 52, 53]. To date, a theory describing these dynamics does not exist.

Experimentally, high brilliance 3rd and 4th generation synchrotron light sources have made it possible to carry out X-ray photon correlation spectroscopy studies (XPCS) to cover a broad range of dynamics. Nowadays, XPCS has been widely used in different areas of soft condensed matter research, e.g. for studying the dynamics of colloids [56], liquids [57], polymers [58] and clays [59]. Recent progress in the experimental and conceptual frameworks are allowed to overcome the difficulties in working with beam-sensitive samples [60–62, 279] and often called bio-XPCS [63, 64, 220, 222, 223, 280].

Time-dependent dynamics of XPCS studies for non-equilibrium processes are frequently presented using two-time correlation functions (TTCs) [179, 197, 208, 209, 231, 281–283]. The rich features of TTCs are closely related to the non-equilibrium dynamics; however, interpretation of the TTCs often focuses only on the component along the diagonal of TTCs [179, 197, 208, 209, 282] and further extraction of its relaxation time and Kohlrausch exponent for the description of the investigated dynamics [267]. A recent study of thin-film growth on polycrystalline surfaces [281] has demonstrated that the observed "side" features in the TTC are related to the step-edge velocity. An XPCS study of layer-by-layer crystal growth [283] show that additional features in the TTC are connected to the memory effect in the arrangement of islands formed on successive crystal layers. In both studies, equation-based numerical modeling was used to rationalize the experimental results. Such a simulation of complex, multi-component processes may confirm the existence of certain features but cannot unambiguously pinpoint their physical origin. In this case, another simulation approach, i.e., controlled variation of the key parameters in the equations to study the dependence of TTC features on these parameters, but not directly its dependence on the dynamical phenomena. For a more detailed investigation of the connection between the dynamics and the obtained TTC features, it is desirable to decouple the complex dynamics of the system into sub-phenomena. This approach can be realized via simulations based on the Reverse-Engineering (RE) technique [284–286]. In essence, RE is the deconvolution of a complex system into simple components followed by the analysis of how these components work independently and how they interact. The RE approach has been applied in different research areas, such as the design of soft materials with the desired properties and functions [287–289].

This work proposes a Reverse-Engineering approach based on particle-based

heuristic simulations to understand the complex dynamic features of TTCs obtained from XPCS measurements. The system studied is of bovine serum albumin (BSA) solution in the presence of trivalent salt YCl_3 [44]. The kinetics of LLPS has been studied previously, and a tendency to a kinetically arrested state is reached [45, 46]. Furthermore, the non-equilibrium dynamics of this system has been presented in the Chapter 4 and in [220]. However, some unresolved issues has remained. The classical analysis of XPCS data was insufficient to judge the presence of gelation in the studied sample. Additionally, the experimental results show rich side features in the two-time correlation map (TTC). This work is a step forward for the investigation of the dynamics of LLPS [2, 22, 220, 223, 290] on the micrometer scale of phase separating domains. The main objective of this chapter is to advance the field of XPCS analysis and improve the knowledge of the features displayed on TTCs, their possible explanation and the connection between them, and the key control parameters of the non-equilibrium dynamics. The RE approach may be successful in going beyond the existing theory if there is no theoretical formalism for the investigated phenomenon or if the experiment cannot be fully described by theory.

5.2 Results and discussion

5.2.1 Dynamic map from XPCS measurements

A typical experimental TTC for LLPS on a micrometer length scale was presented in Section 4.3.1 and is reproduced in this section in Figure 5.1 (a). The measurement details can be found in Section 4.2. A relaxation signal appears a few seconds after the temperature jump, initially with a fast decay rate, but quickly broadening. After the quick broadening, the main relaxation along the diagonal turns into a steady state. A new slow relaxation mode gradually appears, and its correlation shows a decay around 20-30 s, leading to a "square" feature in the TTC.

The typical TTC discussed here contains three characteristic features: modulation along with diagonal, "square" feature, and "tail" (follow labels in Figure 5.1 (a)). The modulation represents the main component of the dynamics. The "square" feature is presented as the frozen-in component that is visible as a square-like background (Figure 5.2). "Tails" are oscillations of the $G(q, t_1, t_2)$
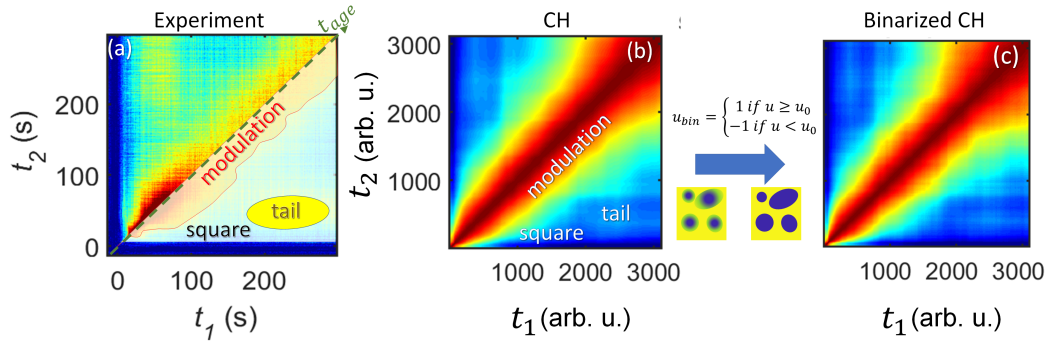
Figure 5.1: Two-time correlation functions for temperature jump from $10\,°C$ to $40\,°C$ for 312 s for BSA-YCl$_3$ sample at $q = 4.4\mu m^{-1}$ **(a)**. Shaded patches on **(a)** mark the regions of features of the TTC. White shade for "square", red for "modulation", and yellow for "tail". The green dashed line shows a direction of increase of experimental time t_{age}. The result of the CH simulation is presented on **(b)** and represent similar to **(a)** features (marked only with text). **(c)** The TTC of the CH simulation with the binary modification of the 2D concentration field. Jet color bars of TTCs correspond to $G(q, t_1, t_2)$ values. Above the blue arrow, there is an equation used for binary modification, and below, there are schemes of the real space 2D concentration field $u(\mathbf{r}, t)$ before and after binary modification. Parula color bars of the schemes correspond to the concentration distribution (from blue (-1) to yellow (1) color). The time of CH simulations is in the arbitrary units (arb. u.). The presented range of time in arb. u. of CH simulation corresponds to the experimental time (see Figure 4.9).
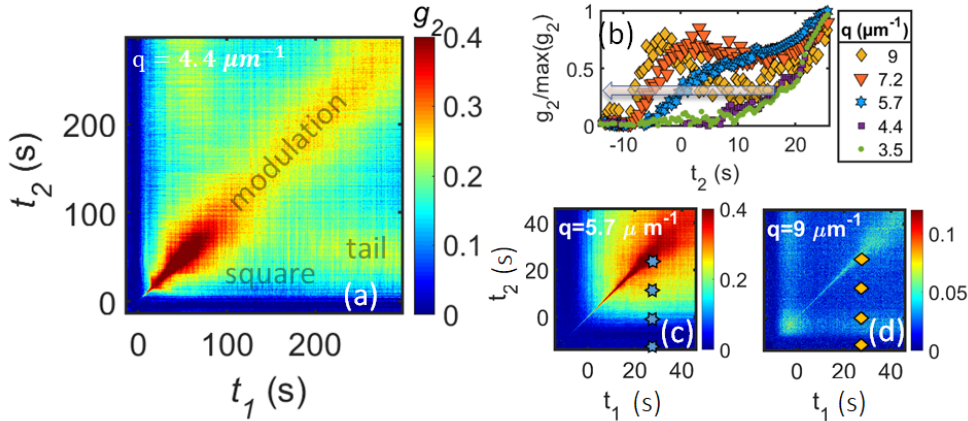
Figure 5.2: Two-time correlation functions for temperature jump from $10\,°C$ to $40\,°C$ for 312 s (a) and for 60 s experiments (c-d) for different q-values. Color bars correspond to $G(q, t_1, t_2)$ values. On (a), features of the TTC ("modulation", "square", and "tail") are displayed with a half-transparent grey text. (b) "Square" feature dependency can be caught by the normalized vertical cuts of TTC at $t_2 = 30s$ (follow blue stars on (c) and orange diamonds on (d)) for different q. A rapid increase in the values corresponds to the beginning of the "square" feature at the TTC. It is shifting to earlier t_2 with an increase of q (grey arrow).

values along t_1-axis. In Figure 5.1 (a) these "tails" are areas of high contrast around $t_1 \sim$230s, $t_2 \sim$50s and symmetrical to the diagonal one. Both "square" and "tail" features exhibit strong q-dependency. They move to earlier times t_{age} with increasing q, which means that processes corresponding to these features are size-sensitive and detectable earlier for smaller sizes on the microscopic length scale (follow Figure 5.2 (a)-(d)). Another important feature of experimental TTCs is the fluctuation of the contrast near the diagonal with time t_{age}: initially, there is a rapid increase followed by a moderate, gradual decline. The classical analysis of the TTC for the LLPS systems with the extraction of the relaxation times and Kohlrausch exponents evolution can be found in [220, 223] and Section 4.3.1.

Here, we would like to investigate the relationship between the observed TTC features and the studied dynamical processes. In the following, we show that these features also appear in the classical CH simulations and are related to specific dynamical processes of the studied system.

5.2.2 Cahn-Hilliard simulations

Classical Cahn-Hilliard theory

The Cahn-Hilliard equation can describe the evolution of the spinodal decomposition in real space (see Section 1.3.2). The 2D CH simulations which are used here for the investigation of TTC features were already presented and described in the Section 4.3.2. In addition to those details, in Appendix Section 5.4.1 one can find a discussion on the use of the 2D simulations to describe the experimental results which probe dynamics in a volume. To conclude, despite the quantitative difference between 2D and 3D simulations [291, 292], the 2D CH simulations are sufficient for the qualitative analysis of the bulk dynamics of the system. The employed 2D Cahn-Hilliard model is considered to be a minimal model that captures the essence of the physical behavior [293].

The main results of the simulations are presented in Figure 5.1 (b) (were previously shown in Figure 4.8). The simulated TTC reproduces the main features in the experimental TTC, i.e., modulation, "square" and "tail". We note, though, that there are some obvious discrepancies between simulated and experimental TTCs. The "square" and "tail" features are significantly less pronounced in the simulation than in the experiment (compare Figure 5.1 (a)

and (b)). Furthermore, there is no change in the contrast along the diagonal of the simulated TTC. Importantly, the early stage of phase separation (~ 30 s) is not reproduced by the simulation.

The typical strategy to overcome the discrepancies between the simulations and the experimental TTCs is to introduce a more sophisticated model with more parameters to optimize (e.g., Cahn–Hilliard with varying mobility, Navier—Stokes–Cahn–Hilliard). Unfortunately, this approach has many disadvantages. The CH equation-based models provide a simulated evolution of the real space behavior. However, there are multiple sub-phenomena that can affect the resulting correlation maps: the emergence and disappearance of domains, their growth or dissolution, merging, changing the shape, variation of concentration at each point of the simulated pattern, etc. These sub-phenomena of LLPS may co-occur and depend on each other (e.g., the evolution of concentrations and domain sizes). The only way we can investigate these processes is via changing the parameters of the model. However, the parameters affect the dynamics in a complex nonlinear way, making it challenging to study how different dynamical sub-phenomena influence TTCs independently. To overcome this difficulty, we perform a direct modification in the simulated patterns.

Binarization of Cahn-Hilliard simulations

As the first step, we simplify the CH model via binarization of the simulated real space patterns:

$$u_{bin}(\mathbf{r}, t) = \begin{cases} 1 & \text{if } u(\mathbf{r}, t) \geq u_0 \\ -1 & \text{if } u(\mathbf{r}, t) < u_0 \end{cases} \tag{5.1}$$

Surprisingly, despite the seemingly drastic changes, the resulting TTCs from a binary real space are virtually the same as from an initial CH simulation (Figure 5.1). The only difference is the slightly less prominent "square" feature, which nevertheless appears at the same position. The fact that TTCs are nearly not affected by the binarization procedure is already a remarkable observation. It inspires to proceed with further simplifications of the model in order to study different aspects of the dynamics in an isolated and controllable fashion.

In this way, we can now consider a simplified simulation of the evolution of the binary domains evolution and study how a TTC depends on different

dynamical processes such as growth and dissolution rates, domain sizes, and so forth. Thereby, in the following, we introduce a domain-based simulation with "manual" control over all these dynamical processes of domains. We note that such an approach can be applied to various dynamical systems.

5.2.3 Reverse-Engineering approach based on particle–based simulation

In order to simulate different phenomena such as growth, dissolution, merging, random-walk motion, shape/size/concentration distribution, as well as any combination of them with manual manipulation of all of the dynamical parameters, we model the simulated domains as spherical particles on a 2D map (256×256 map). Similar to the binarization approach described above, the concentration is constant inside the domains ($u_{dilute} = -1$ if not stated otherwise) and outside the domains ($u_{dense} = 1$). For each domain, we specify its radius and position as functions of time (see below).

As a result, we obtain a 2D concentration map, representing our sample in real space and its evolution with time. The corresponding TTC is calculated in the same way as for CH simulation (Section 4.3.2): at first, the scattering intensity is determined, and then Equation 6.1 is used. The RE approach will allow us to connect the various features in TTCs to the key control parameters of the phase separation process.

"Modulation" and "Tail"– Features of Growth

One of the main sub-phenomena taking place during the LLPS is the change in the size of the domains. To study how the domain growth influences the TTC, we simulated a set of spherical particles at random fixed positions and linearly growing radii with time (see Figure 5.3). It is clear that there is a modulation of the relaxation time and the "tail" features appear in the TTCs. The origin of these features will be discussed in section 5.2.3. An increase in the size distribution results in a smearing of the modulation (the narrowest part of the modulations along the diagonal is marked with white arrows in Figure 5.3).

The number of the modulations depends on the initial and final sizes of the particles (Figure 5.3 and Figure 5.4); however, the final TTC also depends on their values at each point in time. This can be seen while performing the
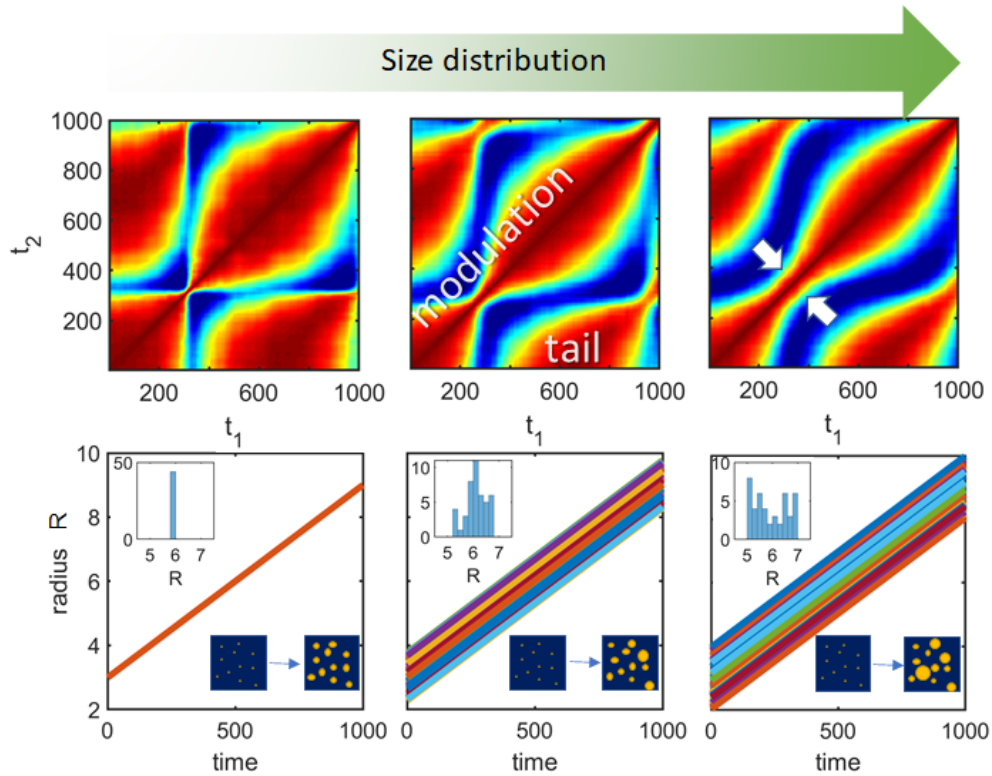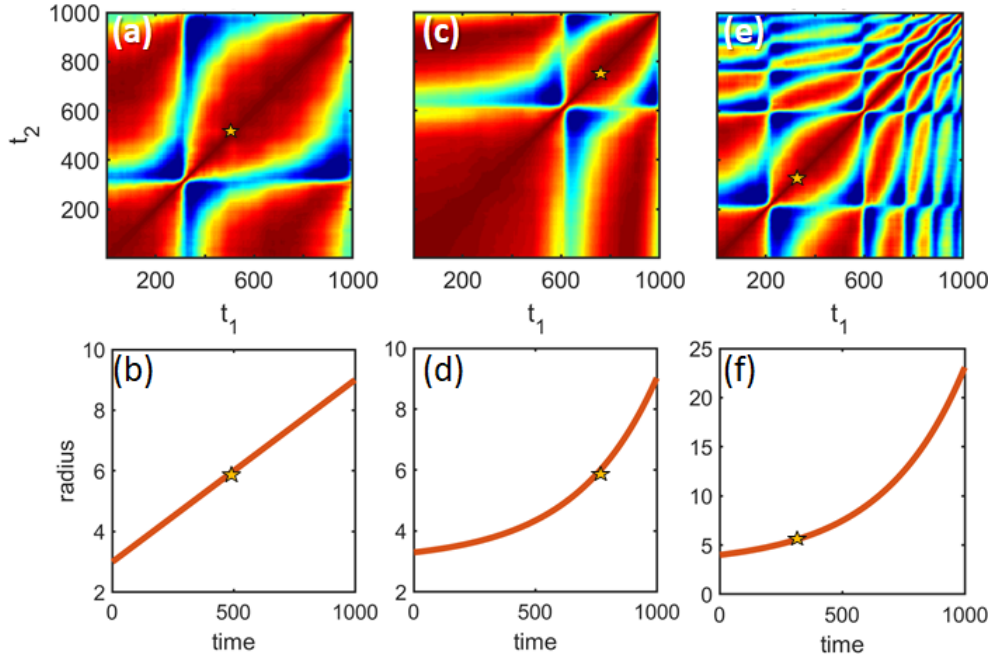
Figure 5.3: Particle-based simulation of linear growth with different radii distribution. The bottom row demonstrates the evolution of the radii of particles with time with the real space schemes in the right bottom insets and the distribution of radii in the left upper insets. Different colors correspond to different particles. The upper row of the figure shows the corresponding calculated TTCs at the same q-value. White arrows point to the "modulation" waist in the TTC. The size distribution increases from the left to the right, while the mean value evolution is the same.

particle-based simulation of growth with different speeds. Figure 5.4 (a) and (c) show TTCs of the particle system with linear (b) and exponential (d) growth of radii, respectively, with the same initial and final values. Both of the TTCs demonstrate 1.5 modulations; however, the shape of the "tail" feature and the period of modulation depends on the function of the rate of growth. The exponential growth with different boundary conditions (Figure 5.4 (c) and (e)) results in the same shapes of TTC features, distinct from linear growth (Figure 5.4 (a)). This result can be easily understood (follow the "star" in Figure 5.4); for instance, a linearly growing system reaches $radius = 6$ at $time \approx 500$ (b), while exponentially growing systems - at $time \approx 800$ (d) and ≈ 350 (f), respectively. These time points result in exactly the same environment in the TTCs: they are located on the first half of the second modulation feature (as indicated in

Figure 5.4: Particle-based simulation of growth with different speeds. The bottom row demonstrates the evolution of the radii of particles with time. The upper row shows the corresponding calculated TTCs for the same q-value. (a-b) show linear growth of particles from $radii$ = 3 to 9 pixels.(c-d) represent exponential growth of particles from $radii$ =3 to 9 pixels. (e-f) show the exponential growth of particles from $radii$ =3 to 23 pixels. The yellow star with a black border shows when the $radii = 6$ for different simulations. These time points result in exactly the same position on a modulation feature while the features are transformed according to the non-linear behavior of the radii of particles with time.

the Figure 5.4 (a), (c) and (e) by the yellow star). A similar procedure can be performed with any value of the size parameter $radius$. Finally, one can find that the TTC in (c) is similar to the non-linear interpolation of the TTC in (a), corresponding to the non-linear behavior of the radii of particles with time. Therefore, if the speed of growth increases with time, then the relaxation time decreases and vice versa. The uniformity of modulations depends on the speed of growth. The TTC is periodic only if the speed is constant, corresponding to the monotonic increase of the size of the particles. The larger the rate of the speed, the smaller the distance between adjacent modulation peaks. Thus, the TTC of the growth process calculated at a specific q-value contains information about the evolution of the mean size and the distribution of particles of the whole system.

5.2.3. Reverse-Engineering approach based on particle–based simulation

Connecting domain size with the "tail" feature

We further demonstrate here that the position/amount of "tail" features are connected with the mean size of domains. We assume that during the growth of domains, intensity fluctuations become narrower, intensity peaks are shifting and at a certain point for a given q-value there can be a correlation between the n_{th} peak at time $t_{age}=t_k$ and the $(n+1)_{th}$ peak at time $t_{age}=t_l$, where $t_l > t_k$ (Figure 5.5 (c)).

In our experiment, we observed the change in the evolution of intensity for fixed q due to a change in interparticle distance, which results in the shift of the peak of $I(q)$ to smaller q-values with time. Similar TTCs with "tail" features were recently obtained during growth on polycrystalline thin-film surfaces [283], where multiple "tail" features were detected at the TTC, and the oscillatory behavior of the g_2 was observed. It was shown that the "tail" structure in [283] appeared once the thickness of the deposited layer was equal to the integer multiple of the monolayer one. Such correlation was interpreted as a memory effect in the arrangement of islands.

Figure 5.5 (b) illustrates a similar effect for our simulations. The contrast profile (defined as a value of TTC next to the diagonal) exhibits a periodic behavior as a function of time. It can be demonstrated that the period of the contrast is determined by the two key spatial parameters of the system. The first parameter is $2\pi/q$ corresponding to the length-scale where the dynamics was investigated. The second one is the time-dependent characteristic length $\xi_{XPCS}(t_{age})$, which for the simulation is the average particle diameter. By trivial recalculation of the contrast profile time dependency into the characteristic length dependency, we show that the "tail" appears approximately once the characteristic length the characteristic length of the system is an integer multiple of $2\pi/q$ (Figure 5.5 (b)). Using this idea, experimental TTC maps with pronounced "tail" features were used for calculating ξ_{XPCS} to follow the microscopic growth kinetics of our BSA-YCl$_3$ sample. The comparison with characteristic length, calculated from the peak position of the USAXS profiles $\xi_{USAXS} = 2\pi/q_{peak}$, agrees well with ξ_{XPCS} obtained from the XPCS data (Figure 5.5 (d)). According to theoretical predictions [112] (see Section 1.3.1), the characteristic length should follow a power-law $\xi \propto t_{age}^{1/3}$ due to coarsening mechanisms based on diffusion or coalescence. However, it was found [46] that the BSA-YCl$_3$ system shows an arrested phase transition at high temperature, and the evolution of ξ cannot be described
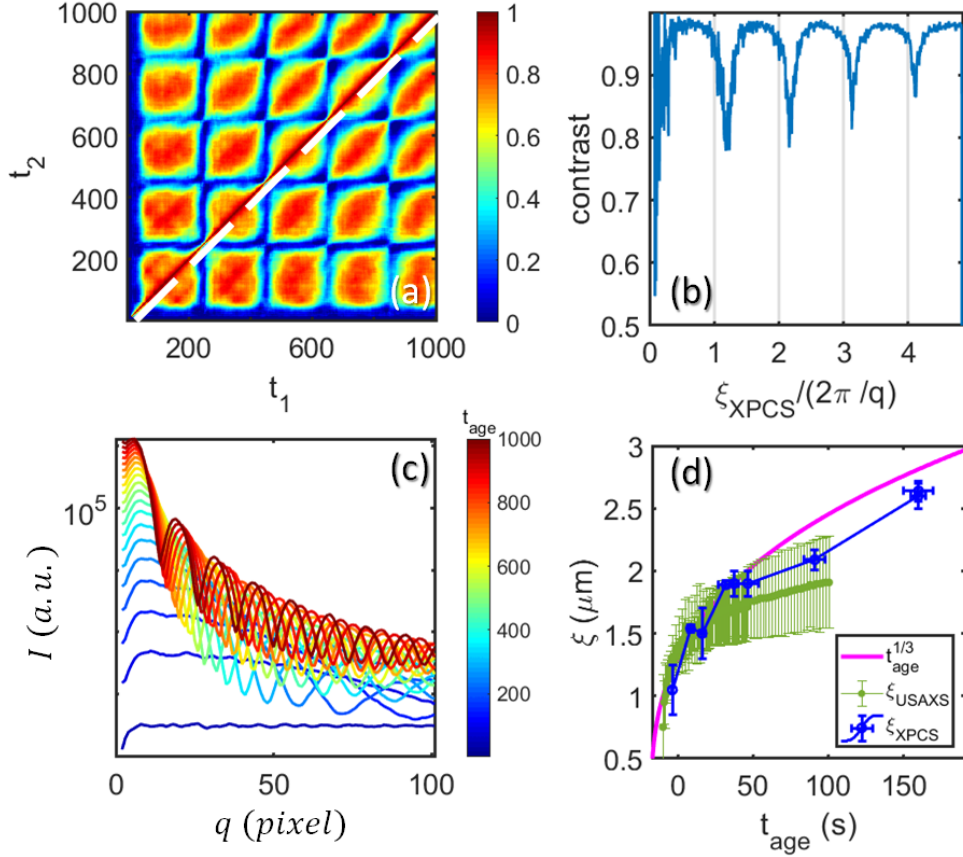
Figure 5.5: Extraction of the mean size for the particle-based simulation (a-c) and experiment (d). **(a)** TTC calculated for the model of identical particles which are growing with constant speed. **(b)** Dependency of contrast taken a pixel away from the diagonal in **(a)** (marked with white dash line) as a function of average system size $\xi(t_{age})$ divided to the size $2\pi/q$ corresponding to the investigated q-region. **(c)** Evolution of the intensity profile during the growth. **(d)** Extraction of sizes from the experiment. The behavior of the characteristic size of the system is calculated with different methods. Characteristic length, obtained from the peak position in the scattering intensity $\xi = 2\pi/q_{peak}$, is plotted for USAXS measurements. The pink line corresponds to the theoretically predicted increase of characteristic length with time following power of $1/3$ due to coarsening mechanisms based on diffusion or coalescence [112]. Blue markers represent the average size of the domains calculated from XPCS measurements, following the appearance of "tail" features at TTC for different q-values.

with classical spinodal decomposition theory. Therefore, the possibility of following the time dependence of ξ is crucial for these types of systems [46, 47, 52]. In Figure 5.5 (d) it is clearly seen that the ξ_{USAXS} plot is more complete, however ξ_{XPCS} can be estimated from XPCS results even if the peak of the intensity profile (required for ξ_{USAXS} determination) moved out of the measurement window and a second-order of $I(q, t_{age})$ profile is not well-pronounced. Such a possibility

to extract sizes from the XPCS experiments may open new prospects for the experiments on growing, coarsening, or evolving systems.

"Square" feature caused by two-step processes

We showed that the growth process results in the modulation and "tail" features in TTCs similar to the ones observed in the experiment. In Chapter 4 ([220, 223]) the correlation between the "square" feature and transition from the density fluctuation stage to the coarsening stage of spinodal decomposition was shown. However, the subphenomena that impact the "square" feature remained unclear. With the use of Reverse-Engineering, we show three possible ways of obtaining the square-like feature in the TTC (see Appendix Section 5.4.2 for details). The first case is a rapid change of the shape of particles: time moments with similar particle shapes result in a substantially higher correlation on TTC compared to the moments with different particle shapes (Appendix Figure 5.20). The second option is the rapid growth of particles followed by dissolution. As demonstrated in Figure 5.6, the rate of growth should be much larger than the rate of dissolution. The third option is the rapid growth of contrast between the concentrations of particles and the background so that the initial and the final states have different standard deviations of the concentration distributions. The early stage of LLPS consists of the density fluctuation stage, and its transition to coarsening stage is characterized by all of the options described above. The system undergoes a change of shape from worm-like structures to sphere-like domains of dilute phase surrounded by dense phase. Also, there is a rapid growth in the domain size (coupled with the change of the concentration), followed by dissolution of the smaller domains during an Ostwald ripening process [110] at the later, coarsening stage. As was shown in Section 5.2.2, the concentration change is not the main process that impacts the "square" feature. Also, the change of shape is not as drastic during the real liquid-liquid phase separation as in the particle-based simulation. Thus, we will focus on the growth-dissolution behavior as the main process during LLPS.

The change of sizes of domains during the LLPS can be simplified as a two-step process. The first step is an overall growth in the early stage. The second is the growth of one fraction of particles and the dissolution of another (Ostwald ripening) in the coarsening stage. Figure 5.6 presents the particle-based simulation investigation of the impact on the TTCs from each of these components
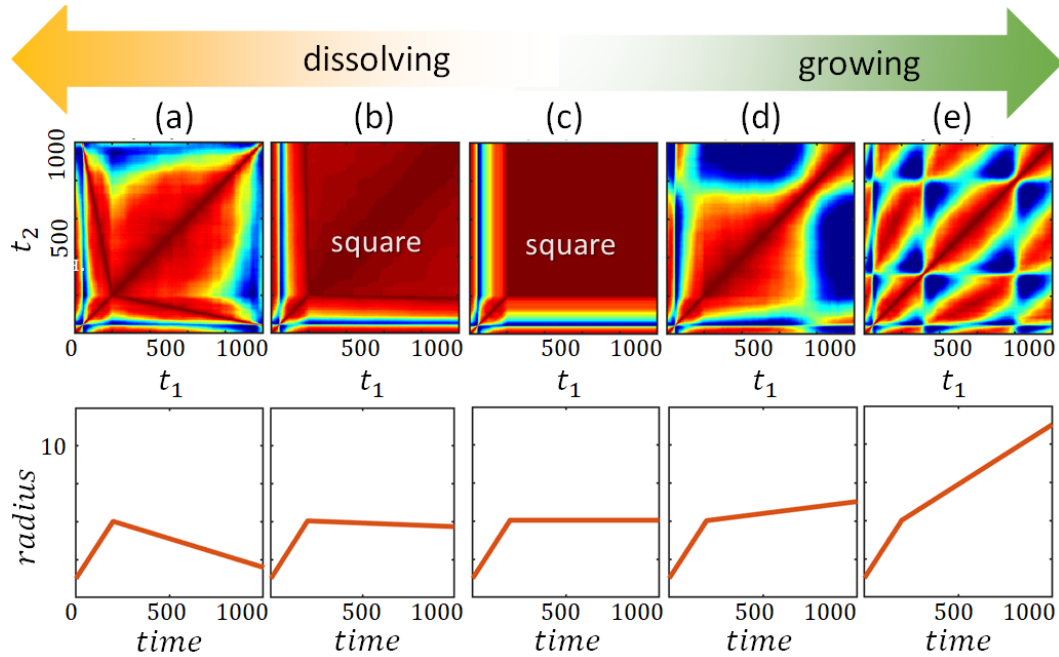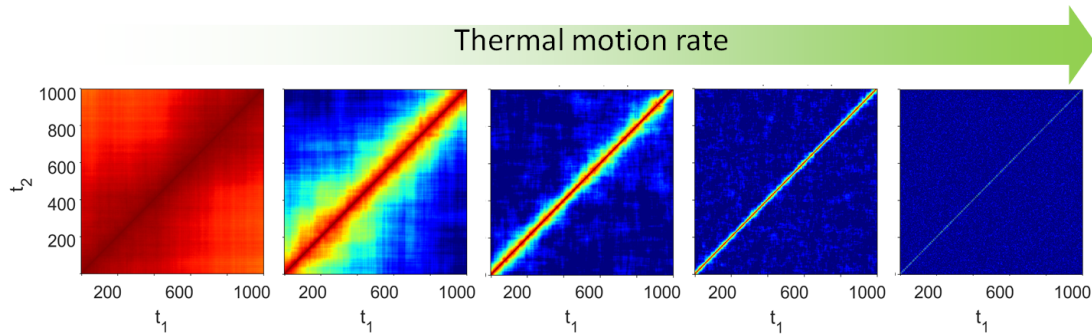
Figure 5.6: Particle-based simulation of a two-stage process. The bottom row demonstrates the evolution of the radii of particles with time. The upper row shows the corresponding calculated TTCs for the same q-value. The speed of growth in the first stage ($time < 200$) is the same, followed by the different rates of the second stage. This stage is dissolution in (a-b), no change in size in (c), and growth in (d-e).

independently is presented. For a better comparison, the first step, representing the growth of the particles, was the same for all processes. Furthermore, we assumed the same growth rate for all particles. If the second step is also growth (Figure 5.6 (d-e)), it results in the modulation and "tail" features on TTC, as described in the previous section. The amount of these features depends on the speed in the second step (compare (e) with (d)). If there is no change of size (c) or there is a slow dissolution in the second step, the "square" feature appears on TTC (b). The strength of this feature (value of the $G(q, t_1, t_2)$) depends on the ratio between the rates of the growth and the subsequent dissolution. The slower the dissolution, the more visible the "square" feature (compare (b) with (c)). Finally, if the rate of dissolution in the second step is similar to the rate of growth in the first step - the "square" feature completely disappears (Figure 5.6 (a)).

The "square" feature detected during the experiment is size-sensitive: it appears earlier for larger q-value (Figure 5.2 (b)). This observation is consistent with the result of the particle-based simulation. Based on these findings, we

5.2.3. Reverse-Engineering approach based on particle–based simulation

Figure 5.7: Particle-based simulation of the Brownian motion effects. The rate of dynamics increases from left to right. Faster is the Brownian dynamics, smaller is the relaxation time in the TTC.

suggest the following explanation of the "square" feature for USAXS-XPCS experiments on LLPS systems. During the Ostwald ripening process, small domains are the first to be dissolved. Since the size is inversely proportional to the value of q: these domains correspond to the high q-values. Thus, the q-dependency of the "square" feature is the result of the earlier transition from the growth stage to dissolution for small domains than for the large ones.

Brownian motion leads to reduction of feature visibility in TTC

So far, we have modeled the influence of kinetic parameters on the resulting TTCs. For these cases the $< I(q) >$ ($<>$ - ensemble average) is not constant. The kinetics found in controlled features in TTCs are different from the speckle dynamics, which comes from $I(q)$ fluctuations with $< I(q) >$ being constant. In the following, we introduce Brownian motion to the RE model and, thus, study the system with both kinetic and dynamic contributions to TTC.

One of the main processes occurring at the early stage of LLPS is the growth of the domains. According to our particle-based simulation, we should expect modulations and a "tail" at the corresponding times on TTCs. These features appear in the CH simulation, however, the experimental behavior at the early stage of LLPS is different: the relaxation time increases exponentially [220, 223] so the dynamics is very fast in the beginning and then quickly slows down; there are neither modulations nor a "tail" at the early stage. This observation is the evidence of some unconsidered dynamics that is not reflected by the CH simulation.

While it is well known that the early stage of the LLPS is sensitive to the
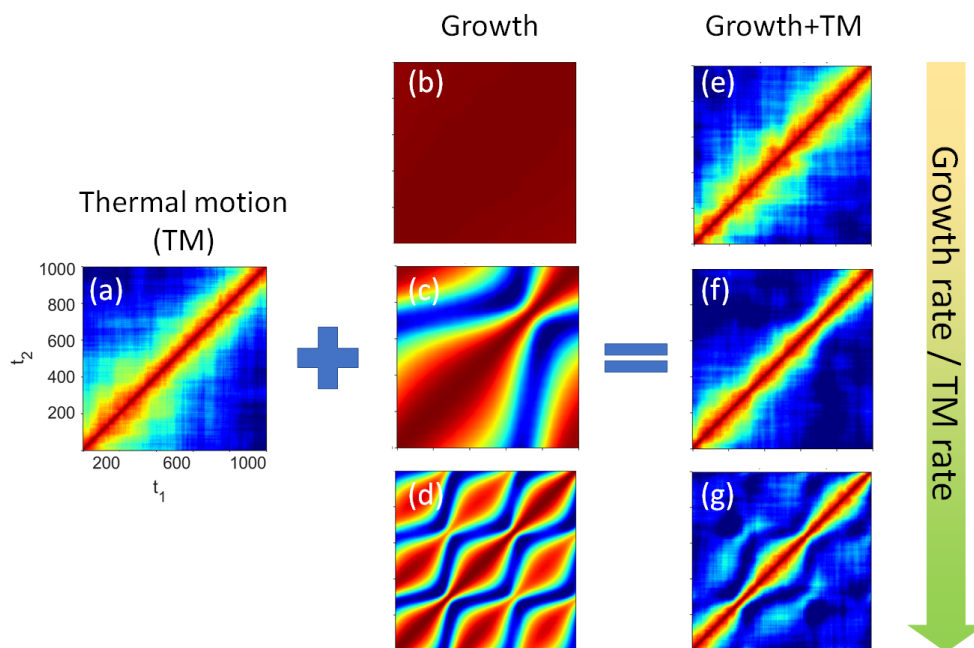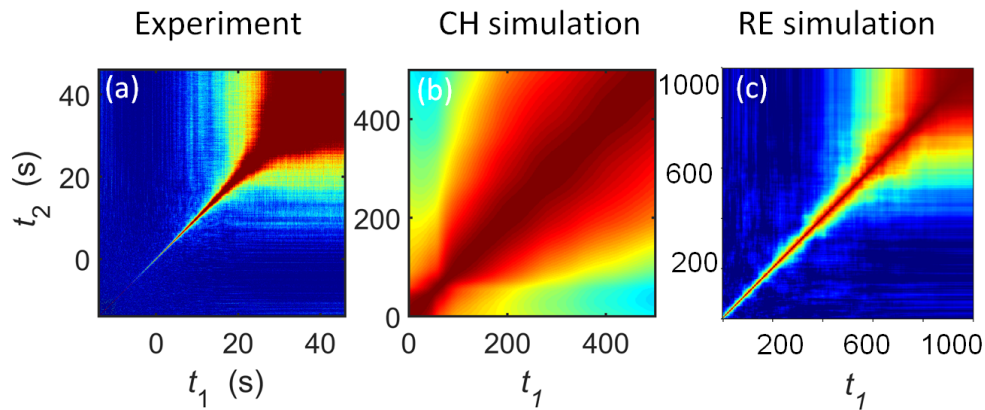
Figure 5.8: Particle-based simulation of the interplay between growth and Brownian motion effects. The TTC of the pure Brownian motion with the constant rate (a). The TTC of the pure growth (b-d) with different rates increased from (b) to (d). The simulation (e-g) of the simultaneous growth (with parameters from (b-d)) and Brownian motion (with parameters from (a)). The ratio between growth and Brownian motion rates increases from (e) to (g). The Brownian motion effects on TTC dominate if the growth is slower (e, f).

thermal motion effects [274], our CH simulation does not include effects of thermal motion, finite heating rate, and viscoelastic properties of real systems, which may be the reason for the difference between simulation and experiment in the early stage of LLPS.

In our particle-based simulation, we model Brownian dynamics as a random-walk motion of the domains. The constant relaxation time in the TTC suggests the equilibrium dynamics, which is consistent with the theory [191, 210]. An increase in the number of particles decreases the degree of heterogeneity. An increase in the rate of motion results in a decrease in the relaxation time (Figure 5.7). The TTC varies from a constant $G(q, t_1, t_2) = 1$, when the Brownian motion is too slow, to a constant $G(q, t_1, t_2) = 0$, when the dynamics is too fast to be caught up within the simulated time scales (Figure 5.7).

As a next step, the interplay between Brownian dynamics and growth is required. We fix the rate of the Brownian motion so that its effect is still visible

### 5.2.3. Reverse-Engineering approach based on particle–based simulation

Figure 5.9: TTCs of the early stage of LLPS: for (a) experiment, (b) CH equation-based simulation, (c) Reverse-Engineering approach. (a) and (b) are initial parts of TTCs in Figure 5.1 (a) and (b) correspondingly. (c) demonstrates the TTC of the particle-based simulation with the significant decrease in the rate of the Brownian motion with time and simultaneous growth of the particles (Appendix Figure 5.22).

in the TTC (Figure 5.8 (a)) and perform a set of the particle-based simulations considering both, Brownian dynamics and growth (e-g), with the variation of the growth rate. It can be seen that if the growth is slower than the Brownian motion (compare (b) and (c) with (a)), the growth features are not visible in the TTC (e-f), and the Brownian motion effects dominate. However, once the growth and Brownian motion rates become comparable, the characteristic features of growth (modulations and "tail") become visible. Thus, the Brownian motion effects may be responsible for reducing the visibility of the growth features.

These results are consistent with our general intuition. When the Brownian motion is much slower than the growth rate, the domain positions remain essentially the same, so TTCs look similar to the pure growth case. When the Brownian motion is much faster than the growth, the particle sizes for each successive moment remain essentially the same, resulting in the TTC similar to the pure Brownian motion. When both rates can be caught within the time scale (simulated or experimental), the center movements of the particles result in the loss of spatial correlations due to the Brownian motion effects. This influences the visibility of the growth features and results in the correlation reduction of all the dynamical processes with the relaxation times higher than the characteristic time of the Brownian motion.

Incorporating Brownian motion into the particle-based simulation leads to TTCs exhibiting similar behavior to what we observe in the experiment (Fig-
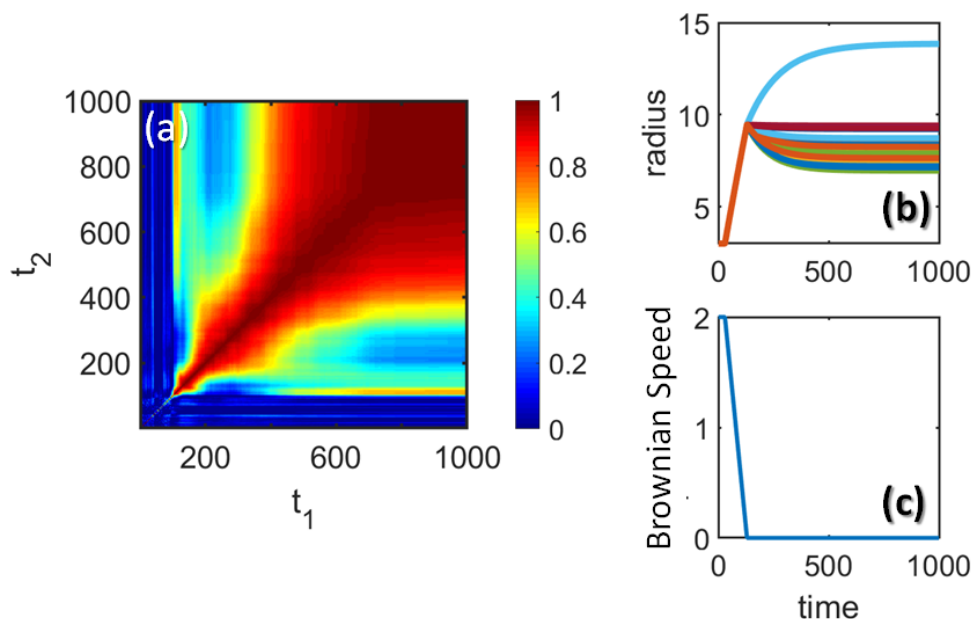
Figure 5.10: Example of TTC, which is possible to obtain by RE with simple models (a). Corresponding evolution of sizes of the particles (b) and Brownian motion speed (c).

ure 5.9 (a, c)). This evidences that the Brownian motion highly influences the real system in the early stage. The rate of the Brownian motion is inversely proportional to the domain sizes, so the influence of Brownian motion on TTC features decreases with time due to the growth of the domains. Moreover, the viscosity of the dense phase is increasing, reducing Brownian motion even more. Therefore, the dynamics of the experimental TTC should be dominated by Brownian motion effects in the early stage with the gradual appearance of the features from other sub-phenomena of LLPS, and, finally, this effect becomes negligible in the coarsening stage. These arguments are in line with Chapter 4 where it was shown that the relaxation rate calculated from the mean intensity changes (reflecting the growth) is not visible in the early stage of TTC. This rate was initially much slower than the rate observed by XPCS (up to 40 times). However, while approaching the coarsening stage, the difference gradually reduces, resulting in the appearance of this rate in the TTC. Thus, these results significantly expand our understanding of the dynamics we measure at the chosen length and time scales in the early stage of LLPS.

5.2.3. Reverse-Engineering approach based on particle–based simulation

RE simulation reproduces all experimental features

Finally, we decided to investigate the interplay between the processes described above and try to obtain a TTC map that includes all of the features seen in the experiment. To mimic the LLPS, we created a simple three-stage model. In the first, very short stage, there were no changes in the sizes of the simulated randomly distributed set of particles. In the second stage, the rapid growth of the particles started. During the last stage, one part of the particles continued to grow (with a slower speed than in stage two) while another one started to slowly dissolve (Figure 5.10 (b)). This model represented the Cahn-Hilliard simulation but also had problems with the fast mode at the early stage of the experiment, e.g., the exponent increase was not observed. As shown in the previous section, a random walk may be added to reproduce the Brownian motion to overcome this issue. For the described model, the Brownian speed had a constant amplitude in the first stage, then it was gradually decreasing to 0 during the second stage, and there was no random walk included in the last stage (Figure 5.10 (c)). Thus, the first stage of the model represents sample dynamics during heat before reaching a two-phase regime ($T < 21°C$). Then there is a high-speed transition from the density fluctuation stage to the coarsening one, resulting in the square-like feature in the TTC. And the last modeled stage corresponds to the coarsening stage of LLPS inside our sample when some particles are growing, and others are dissolving due to Ostwald ripening process. The relaxation time of growth has modulation and increases with t_{age} due to a decrease in the speed of growth of particles. Correlation between different harmonics of scattered intensity results in the "tail" features in the TTC.

The comparison between the experiment and different methods of simulation is summarized in Figure 5.11. It can be seen that the final TTC simulated by RE (Figure 5.10 (a) and Figure 5.11 (c)) reproduces all features found in the experiment. Furthermore, comparison of TTC maps, simulated based on Cahn-Hilliard (CH) (Figure 5.11 (b)) theory and Reverse-Engineering approach (RE) (Figure 5.11 (c)), shows that the second one reproduces experimental features better. The "square" feature is hardly visible for CH, and there is no change in contrast along the diagonal (compare Figure 5.11 (b) and (a)). This demonstrates
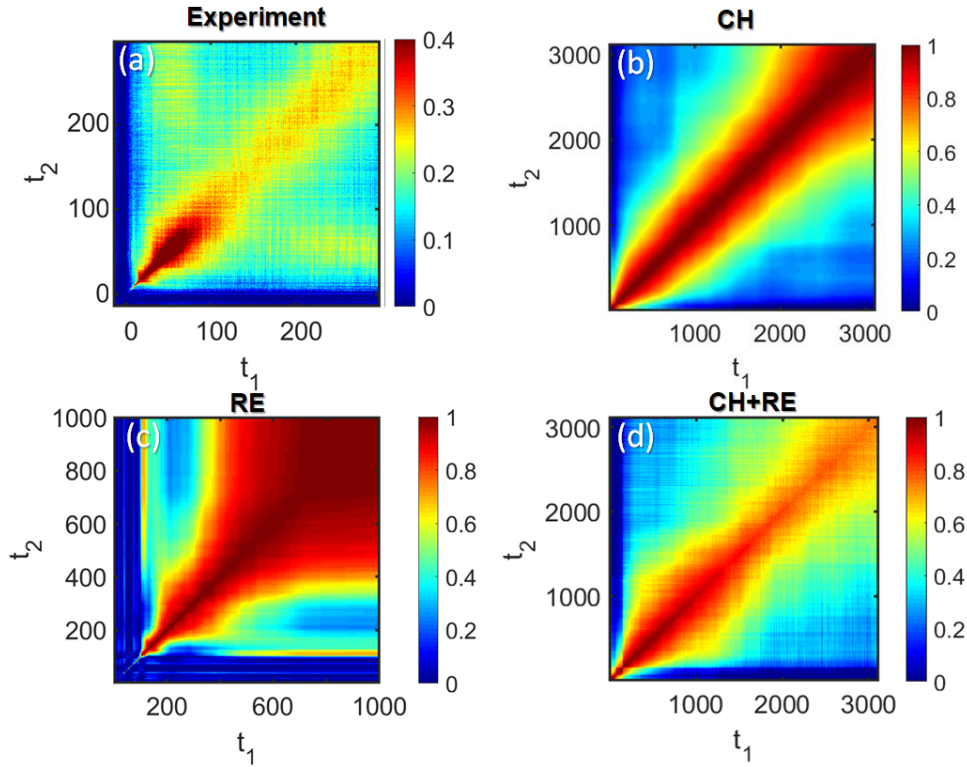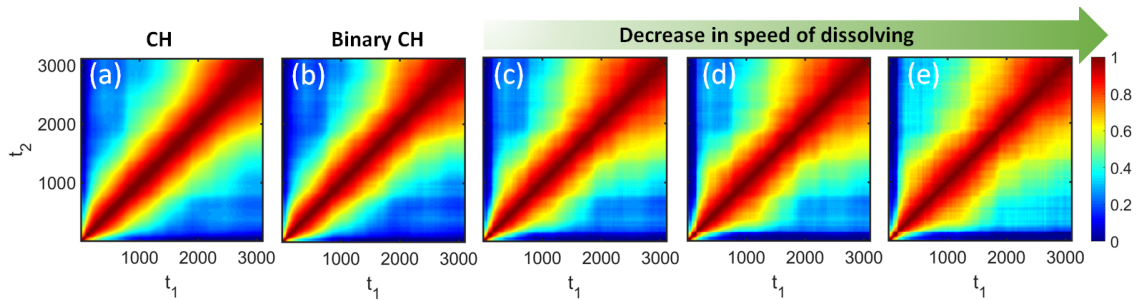
Figure 5.11: (a) Experimental TTC (presented in Figure 5.1 (a)). **(b)** TTC obtained from the CH simulation (presented in Figure 5.1 (b)). **(c)** Example of TTC, which is possible to obtain by RE with simple models (details in Figure 5.10). **(d)** TTC, obtained by modification of the evolution of the system by CH equation with ideas (CH+RE), revealed from the Reverse-Engineering (details in Section 5.2.4). The ratio of speeds of growth in the early stage and dissolution in the coarsening stage correspondingly was increased, which made the "square" feature more pronounced. Furthermore, the noise of 4% was added which resulted in the change of the contrast along with diagonal similar to the experimental TTC.

the limit of the use of classical Cahn-Hilliard simulation to predict and explain experimental results for the system under investigation.

In summary, in Section 5.2.3, we demonstrated that particle-based simulations allow to successfully reverse-engineer the dynamics of the studied system and gain insights into nontrivial connections between the dynamical phenomena and the frequently observed TTC features. Using this, it is possible to successfully reproduce the main features of the experimental TTC by RE without the use of the equation-based theoretical models. This demonstration is helpful for the experiments, which cannot be fully described by equation-based theoretical models or if there is no theoretical formalism for the investigated phenomenon. Thus, the particle-based simulation itself is a significant addition to the regular

Figure 5.12: Two-time correlation maps obtained by modifying of CH simulation with the particle-based simulation. (a) Classical CH (same to Figure 5.1 (b)). (b) The binary modification of 2D concentration field. (c-e) Modifying the binary CH by manually increasing the domain boundaries resulted in a decrease in dissolution speed. The dissolution speed decreases from (c) to (e).

XPCS study. The results obtained here based on 2D simulations are conceptually consistent with 3D simulations (see Appendix Section 5.4.1), which are, of course, computationally much more expensive. The following section connects this novel RE-based simulation with the established equation-based CH modeling of LLPS.

5.2.4 Application of Reverse-Engineering to Cahn-Hilliard simulations

In this section, we extend the RE approach and demonstrate the possibility of combining it with regular theoretical equation-based simulations by modifying the simulated real space accordingly to better understand the studied system. In the following, we apply some very basic changes to overcome the discrepancies between the experiment and the classical CH simulations based on the RE analysis. As mentioned earlier, in comparison to the experiment, CH simulations exhibit a different early stage, pronunciation of the "square" feature, and no contrast variation along the diagonal. The first issue, as demonstrated above, is related to thermal motion. Here, we discuss the other two problems.

Brightness of "square" feature on Cahn-Hilliard simulation - characteristics of gelation

The RE-method showed that the brightness of the "square" feature is mostly dependent on the value of the ratio between the growth rate of the early stage
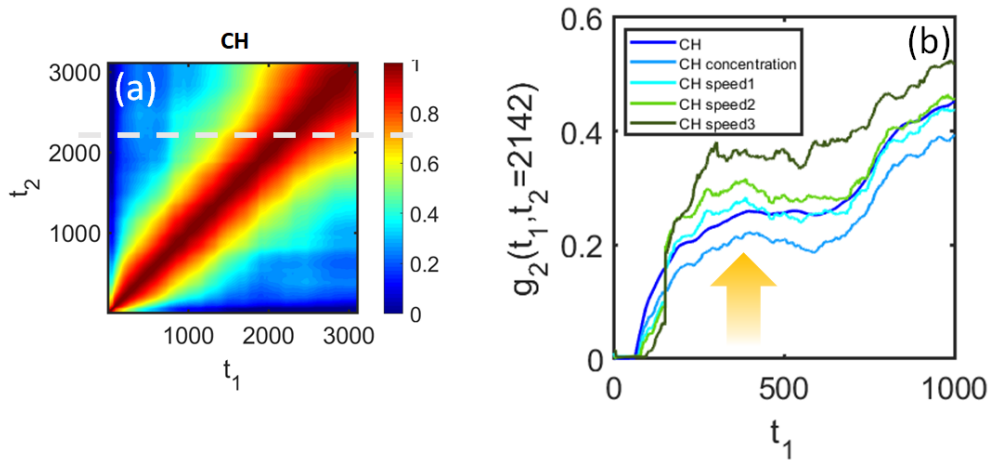
Figure 5.13: Investigation of the impact of different parameters on the "square" feature pronunciation. For each set of the parameters, TTC was calculated, then the cut at $t_2 = 2142$ was made to quantify the "square" feature (**a**). The "square" feature results in the raise jump in the $g_2(t_1, t = 2142)$ curves (pointed by arrow on (**b**)). The bigger this jump, the more pronounced the "square" feature is. The absence of the evolution (e.g., putting domain concentration as -1 and background concentration as 1 for all times) is labeled as "CH concentration" on (**b**) and results in a minor change of the "square" pronunciation (compare "CH concentration" curve with the results of the classical Cahn-Hilliard "CH"). Other curves correspond to the manual modification of the velocity ratio of growth in the early stage and dissolution in the coarsening stage with the absence of the concentration dependency for the real-space maps calculated by the classical CH. The higher the number on labels ("CH speed 1", "CH speed 2", "CH speed 3"), the higher the ratio introduced. It is clearly seen that the increase of this ratio results in the more pronounced "square" feature (follow "CH concentration" with no change in ratio in comparison to the classical CH, "CH speed 1", "CH speed 2" and "CH speed 3").

to the dissolution rate in the coarsening stage. This idea can be checked now with the classical CH simulation. As a first step, the binary modification of the 2D concentration field was performed to simplify the later modifications and interpretations (Figure 5.1, Figure 5.12 (b)). Later, the change in growth to dissolution rates ratio was modified by adding additional pixels at each step of simulation to the calculated boundaries of domains (Figure 5.12). It can be seen that the bigger this ratio of rates is, the more pronounced is the "square" feature (Figure 5.13).

The increase in the ratio of the speed of growth in the early stage to the speed of dissolution in the coarsening stage compared to the classical CH is a signature of the gel/glass transition. It shows that the dissolution of the particles during

the Ostwald ripening process is slower than it was supposed to be in the classical system with constant mobility. Thus, for a more precise theory-based simulation of the chosen experimental system, the classical CH should be replaced with the CH with the change of the mobility corresponding to the gelation process [102]. Having a closer look at such types of simulations (e.g., [223]), one may notice that the closer a system is to the gel state, the more pronounced is the "square" feature for both - experiment and simulation.

The question of the gel transition has already been raised in the Section 4.3.1. Then it was shown that there are experimental prerequisites in the form of a two-step behavior of the relaxation time of the main component. However, we pointed out that the main component does not show a characteristic dynamic arrest, and, accordingly, additional evidence of gelation is needed. We have now demonstrated that the degree of visibility of a "square" feature is related to gelation. And since the "square" feature is much brighter on the experimental TTCs than in the case of classical simulations, the experimental data indicate gelation of the system.

Contrast along the diagonal: low-intensity noise

Another remarkable difference between CH and the experimental TTC is that there are no fluctuations in contrast near the diagonal. One of the typical explanations of such behavior is an additional fast motion, the contribution of which is changing with time, and that is beyond the time resolution of the XPCS measurement. The following data procedure demands the extraction of the localization length [294, 295]. However, it is not expected on the time scale of the measurement for this sample and does not appear in the CH simulation. So, there should be another explanation.

The behavior of the contrast is reflected in the evolution of the distribution of speckles (Appendix Figure 5.23). We found that adding randomly distributed low-intensity noise with a constant amplitude to the scattering pattern of the CH simulations results in the same behavior of contrast as for the experiment. The impact of the noise level on the classical CH simulated maps is presented in Figure 5.14. The change in the contrast is accompanied by a change in the scattering intensity (Figure 4.9 (b)), so with the constant level of noise, there is a change in the signal-to-noise ratio, resulting in contrast fluctuations. According to the simulation around 4% from I_{max} of noise is required to mimic
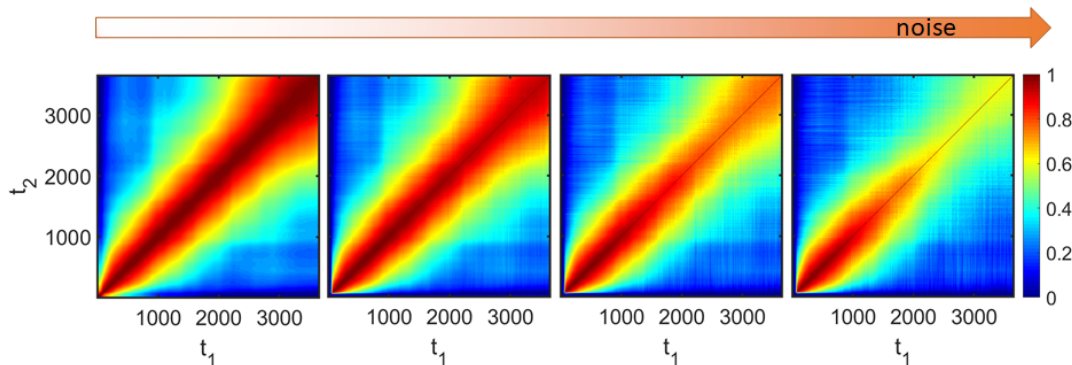
Figure 5.14: The impact of the noise level on the classical CH simulated TTC maps. The randomly distributed noise was added to the scattering intensity calculated by the Fourier Transform of the real space simulated image. The maximum noise level amplitude ($max(I_{noise})/max(I) * 100\%$) varies from 0% on the left till around 8% on the right. The most prominent noise source in the experiment is the scattering background by all incoherently scattering objects (air, water), which change so fast that they are completely incoherent in the time range of single image acquisition.

the experimental results at the investigated q-value. This value was compared to the experimentally measured data to validate the process. The most prominent source of noise in the experiment is the scattering background by all incoherently scattering objects (air, water), which change so fast that they are completely incoherent in the time range of a single image acquisition [296]. Its value can be estimated by the initial scattering of the sample before the LLPS started and is in line with the simulation results.

Finally, as the demonstration of Section 5.2.4, we present the CH simulation modified by Reverse-Engineering and noise in scattering pattern (Figure 5.11 (d)). All of the independent influences are summarized in Appendix Figure 5.24. It can be seen that this cumulative modification of CH by RE is closer to the experimental TTC than pure CH simulation (compare Figure 5.11 (d) and (b) with (a)). Thus, the modification provides a better understanding of the investigated system.

5.3 Conclusions

In this work, we propose a Reverse-Engineering (RE) approach to predict and understand the kinetics and dynamics of systems undergoing non-equilibrium processes. As an example, we studied the liquid-liquid phase separation in BSA-

YCl$_3$ system by XPCS in the USAXS mode. TTCs for the investigated q-values show three characteristic features: "modulation", "square" and "tail". Based on the Reverse-Engineering approach, we reveal the following connections: The "modulation", which is usually the main component for studying dynamics with XPCS, corresponds to the growth of the domains, where the growth rate decreases with time (increasing the relaxation time).

For "square" feature, we found that rapid change of shape and concentration distribution and also a change from the rapid growth of domains at the early stage with subsequent slow dissolution result in the square-like feature of TTC. All of these sub-phenomena are characteristic of the LLPS systems going from the density fluctuation stage to the coarsening stage of spinodal decomposition. However, the RE-modified CH simulations revealed that in the real system the ratio of growth rate in the early stage to the speed of dissolution in the coarsening stage during Ostwald ripening has the most significant impact on the "square" feature. We showed that this rate should be higher than predicted by the classical CH theory, which is a signature of the gelation process. However, this claim was impossible to make based on the established analysis of the main TTC feature, presented in the Section 4.3.1.

The "tail" feature raises from the correlation of the system between different distant times and has a strong q-dependence, appearing earlier for higher q-values. This phenomenon may be caused by the shift of scattering intensity $I(q)$ due to a change in size and mean interparticle distance as a result of the correlation between different harmonics and appears once the characteristic length of the domains is a multiple of the investigation box size ($2\pi/q$). Based on this result, we calculated the characteristic length of the experimental system from XPCS. We showed that it follows the temporal evolution of the characteristic length, calculated from USAXS, which demonstrates that microscopic dynamics and kinetics are intimately intertwined. Furthermore, we demonstrated that the fluctuation of the contrast along diagonal is mainly a result of the incoherent low-intensity noise rather than a feature of the LLPS process.

These results demonstrate that the observed side features in TTCs are not experimental artifacts, but rather a rich source of dynamic information of the system. The Reverse-Engineering approach can go beyond CH theory and build the connection between these features in TTC and the key parameters, such as relaxation time, concentration distribution, the size distribution of domains,

viscosity, and mobility. The RE approach also showed the importance of taking into account thermal motion effects in the early stage of the LLPS. Finally, the framework established in this work can be employed for various systems and processes such as growth, coarsening, or evolving systems, and many other phenomena that are essential for understanding the fundamentals of materials synthesis, processing, and phase transformation. One of the primary benefits of this algorithm is the ability to go beyond the existing theory if the experiment cannot be fully described by it or if there is no theoretical formalism for the investigated phenomenon.

5.4 Appendix

### 5.4.1 On the use of 2D simulations to describe dynamics in a volume

The simulation strategy presented in this thesis is 2D, while the experiment probes dynamics in a volume. Thus, one may raise the question if the obtained results remain relevant for 3D.

As discussed in the Chapter 1, the evolution of liquid-liquid phase separation is usually described in terms of the time dependency of the characteristic size of the system, ξ. For the quiescent system, $\xi \propto t^{\frac{1}{3}}$ is expected [106]. The Cahn-Hilliard (CH) theory assumes that the bulk behavior of the system remains even in 2D (Section 1.3.1). It has been shown that the $1/3$ power-law could be observed for both 2D and 3D CH simulations [293]. Furthermore, simulations confirm the dynamic scaling of the time-dependent structure factor $S(q,t) = \xi(t)^d S_o(q\xi(t))$, where d is the dimensionality of the system. The dynamically scaled correlation function is also independent of the system dimensionality [291]. Therefore, drawing qualitative conclusions for 3D based on 2D simulations is not uncommon in the literature.

To support the conclusions of Chapter 5, the 3D CH simulations for the representative parameters are shown in Figure 5.15. It can be seen that the characteristic features of the TTC are the same. While there is qualitative consistency, there is, of course, a quantitative difference between 2D and 3D simulations [291, 292]. Thus, the employed 2D Cahn-Hilliard model is considered to be a minimal model that captures the essential physics and is sufficient for the presented study of a qualitative comparison between simulation and XPCS experiment.

It is important to point out that the main idea of the Chapter 5 is to disentangle specific features observed in two-time correlation functions in a Reverse-Engineering (RE) approach. Specifically, it is shown that often-observed features in the TTCs such as "square", "tails", and other modulations can be connected to physical processes typically present in systems out of equilibrium. A complete quantitative analysis and comparison of simulations with the data could indeed require, in some (not all) instances, a 3D simulation. However, the aim of Chapter 5 is to show that for identifying the processes at hand (for example, particle
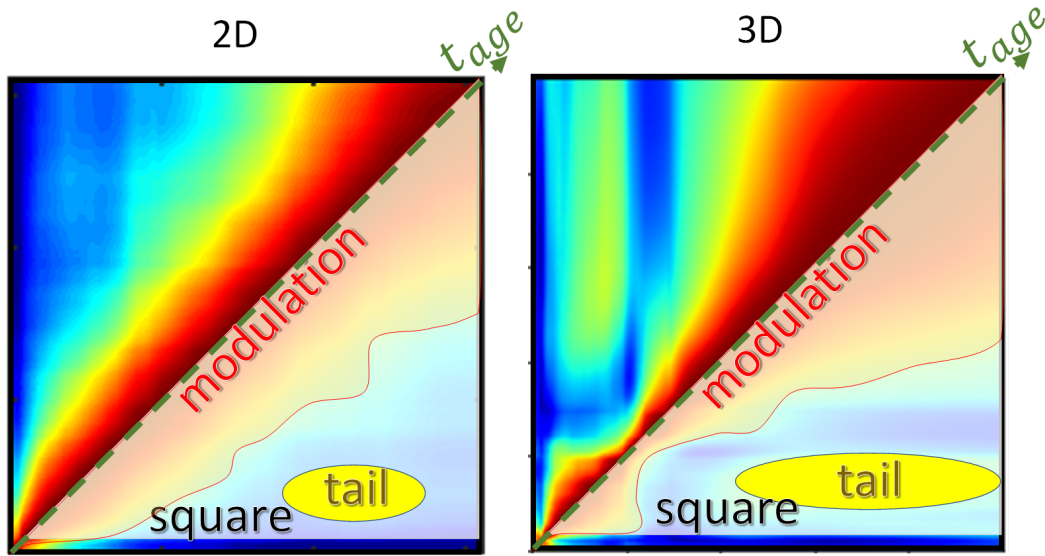
Figure 5.15: Cahn-Hilliard simulation in 2D (presented in Figure 5.1 (b)) and in 3D for representative parameters ($u_0 = 0.5$).
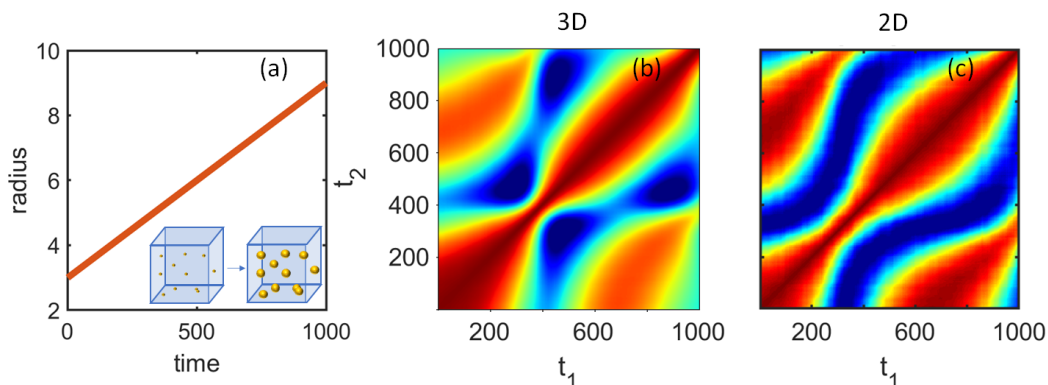
growth or Brownian motion), 2D simulations yield the minimum information needed to interpret the TTCs while being still computational cost-effective and thus easy to handle. Having identified the mechanism at hand – based on our approach - additional 3D simulations would allow refining the results, which is, however, out of the scope of the thesis.

The conclusions about the connections of the physical processes simulated via RE to TTC features hold for 3D simulations. These features originated from the dynamical properties, which can be directly controlled in RE simulations. It is illustrated by an exemplary 3D RE simulation of particle growth (Figure 5.16) which results in the TTC similar to the 2D case. For reasons of transparency, the code used for RE simulations and TTC calculations with arbitrary dimensionality ($d > 1$) is published in GitHub [297].

5.4.2 Possible phenomena underlying the "square" feature

In Section 4.3.1 we have shown that the "square" feature appears as a result of the transition from the early stage to the later stage of LLPS. Nevertheless, the underlying phenomenon remained unknown. Since the "square" feature is visible in the simulated TTC, one may conclude that the corresponding dynamics are already present in the Cahn-Hilliard simulation. Taking a closer look at the
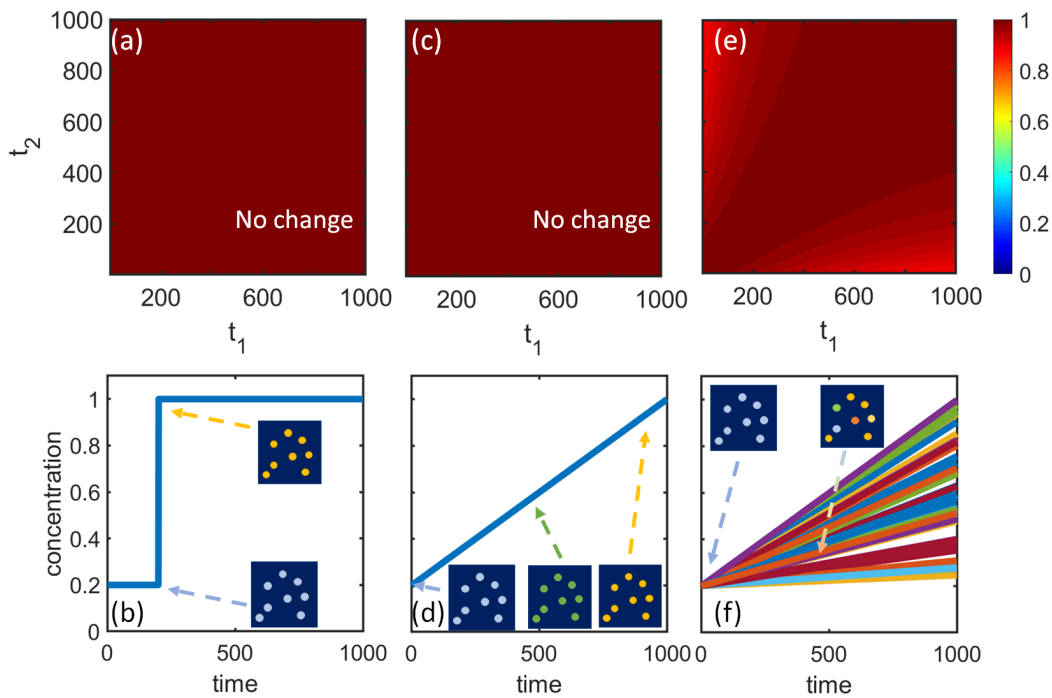
Figure 5.16: Particle-based simulation of linear growth of particles. The TTC for 3D is presented in (b) with corresponding radii evolution in (a). The TTC for 2D (c) is taken from Figure 5.3.

real-space evolution of the simulated concentration map, one notices three major processes taking place while the system transits from the early stage to the coarsening stage of LLPS: concentration, size, and shape changes. In this part of the Appendix, we show the influence of the concentration distribution and shape evolution on the TTC maps. The size evolution is discussed in the main text in Section 5.2.3.

Influence of concentration distribution on TTC maps

First hints on the influence of the concentration parameter on the TTC maps were obtained during the binarization process of Cahn-Hilliard simulations in Section 5.2.2. There it was shown that even such a drastic change in the concentration distribution leads only to a slight change in the "square" feature visibility. Thus, the concentration is not the main parameter influencing this feature. Nevertheless, does any change in the concentration parameter lead to the "square" feature, or should there be some specific behavior? To answer these questions, a particle-based simulation was performed. It is important to note that the scattering is possible only if the concentration (related to density) of the particle is different from the background matter concentration. Therefore, the concentration parameter which is discussed in this section is, in reality, the difference between the concentrations of the particles and the matter.

In Figure 5.17 the particle-based simulation of the systems with different evolution of the concentration parameter are presented. It can be seen that the change in the concentration does not always impact the TTC. When the
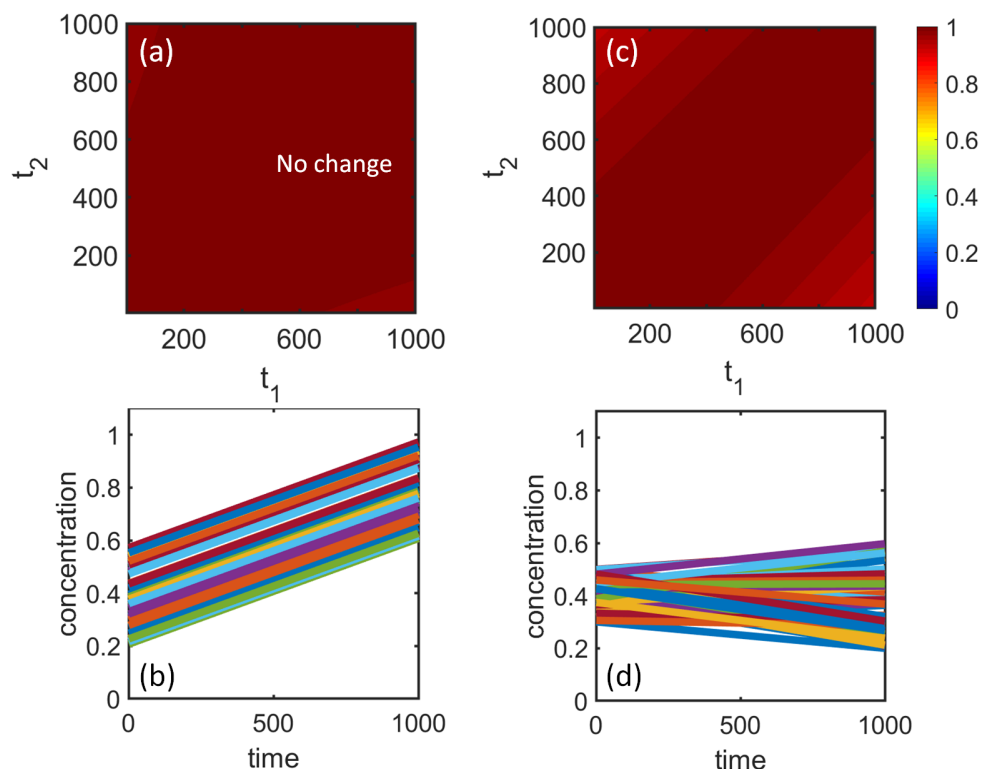
Figure 5.17: Particle-based simulation of the system with the evolution of the concentration parameter. The bottom row demonstrates the evolution of the concentrations of particles with time with the real space schemes in the inset, where the same colors of particles mean the same concentration. The upper row shows the corresponding calculated TTCs for the same q-value. (a-b) relate to the immediate jump in the concentration parameter, which is the same for all particles. For (c-d), all particles also have the same concentration evolution; however, the concentration parameter linearly changes with time. These conditions do not lead to any change in the TTCs. (e-f) relate to the evolution of the concentration distribution.

concentration parameter is the same for all particles, regardless of its evolution over time (Figure 5.17 (a-d)), the corresponding TTC map is similar to the one of a static sample. Nevertheless, the simulation of particles of various concentrations with different linear evolution over time (f) ends up in the non-constant TTC map (e). Thus, the evolution of the concentration distribution may result in a change in the relaxation time in the TTC.

A change in the distribution of concentration can be formalized through a change in two parameters: the mean and the variance. In Figure 5.18 (a-b), the RE simulation for the particles with the change in the mean, but the constant variance is presented. While (c-d) corresponds to the system, which evolves with the constant mean, accompanied by the change in the variance. It can be seen that the variance modification leads to significant changes in TTC, while
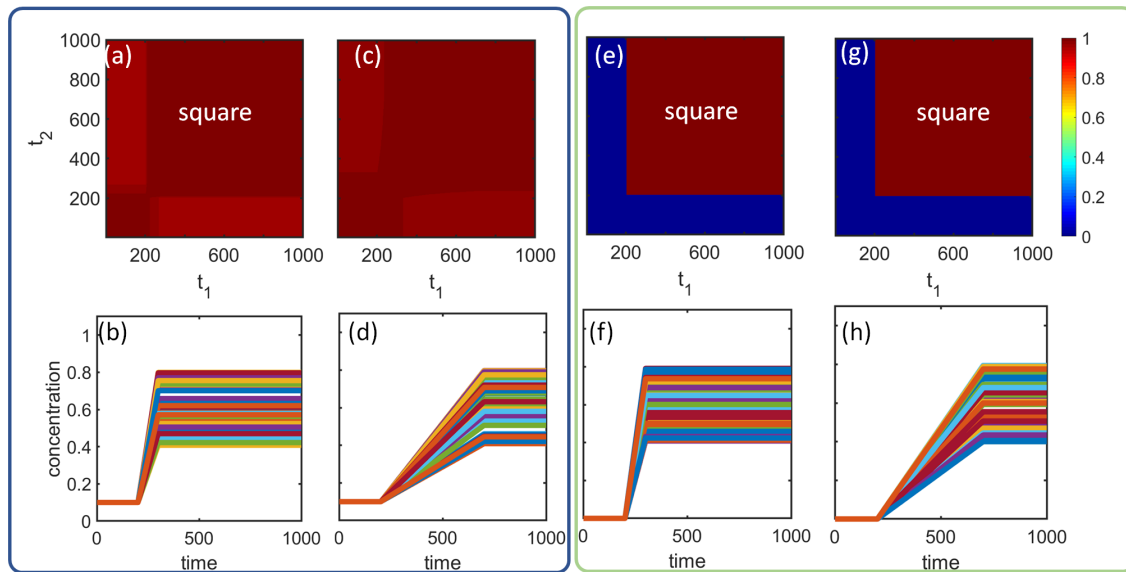
Figure 5.18: Particle-based simulation of the system with the evolution of the concentration distribution. The bottom row demonstrates the evolution of the concentrations of particles with time. The upper row shows the corresponding calculated TTCs for the same q-value. (a-b) relate to the system with the change in the mean concentration but constant variance. These conditions lead to the "frozen" TTC. (c-d) relate to the system with the constant mean but linear evolution of variance. It can be seen that changes in the variance have a more significant impact than the change in mean concentration.

the change in the mean concentration relates to the "frozen" TTC.

If the gradual evolution of concentration (more precisely, its distribution) results in the smooth change in the relaxation time in the TTC, one may assume that the rapid change could lead to the "square" feature.

To check this idea, another set of particle-based simulations was performed Figure 5.19. To mimic the LLPS, the concentration evolution was divided into three stages. At first, the concentration of particles was set to the same value and remained constant. This stage relates to the initial density fluctuations of the matter in the early stage of SD when there is no significant concentration distribution. The second stage in the RE simulation was the growth with the change of the concentration distribution. The length of this period was varied to check its influence on the TTC. This stage relates to the transition from the
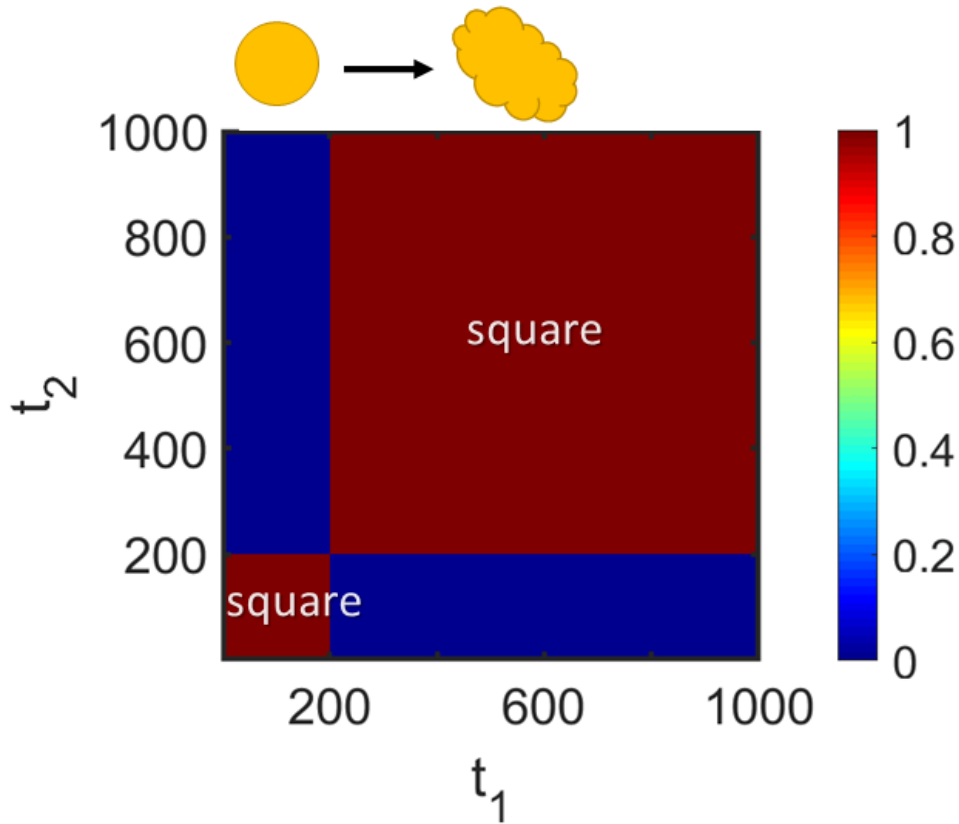
Figure 5.19: Particle-based simulation of the system with the three-step evolution of the concentration parameter: constant, increase with the change in distribution, and constant again. The bottom row demonstrates the evolution of the concentrations of particles with time. The upper row shows the corresponding calculated TTCs for the same q-value. Figures in the blue frame (a-d) relate to the non-zero starting value of concentration, while figures in the green frame (e-h) describe the evolution of the concentration parameter with the zero initial value. (a-b) and (e-f) illustrate the rapid middle step, while (c-d) and (g-h) represent a more gradual middle step. It can be seen that the "square" feature appears as a result of the rapid change in the distribution of the concentration parameter.

density fluctuation to domain growth, accompanied by significant changes in the concentration parameters (see Figure 4.7). In the domain growth stage, the concentration changes are much slower than previously; thus, for simplicity, the concentration distribution is fixed at the final stage of the RE simulation.

These simulations led to the following conclusions. If there is no change in the distribution (which corresponds to the first and third stages), the TTC is constant. Interestingly, the final value of the G (thus, the degree of correlation) does not depend on the concentration value and is $G = 1$ for any $concentration = constant > 0$. In case of zero initial concentration (Figure 5.19 (e,g)): $G = 0$. Figure 5.19 (a) and (e) confirm the hypothesis that the "square" feature appears if there is a rapid change in the concentration distribution. While the smooth change (c,g) demonstrates some gradual change in the corresponding relaxation time (c).

It is worth noting that the simulation with the zero initial concentration is

Figure 5.20: Particle-based simulation of the rapid change of shape. Moments with similar shape of particles correlate much better than with different ones: $t_1, t_2 = [0, 200]$ and $t_1, t_2 = [200, 1000]$.

closer to the real LLPS because at its initial stage, there are only small-amplitude, noisy fluctuations in density difference (Figure 4.7). The concentration of scatters is similar to the concentration of the surrounding matter, and, thus, there is almost no scattering. However, in this case, moments with zero concentration and non-zero one are completely uncorrelated (e-h), which leads to the appearance of a square as soon as the concentration parameter ceases to be zero. This time corresponds to the transition from the first stage to the second, which is not the case for the experimental and CH simulated TTCs. Together with the binarization results, this gives grounds to believe that concentration changes are not the main reason for the appearance of a "square" feature in the TTCs of LLPS.

Rapid change of shape

Another process that can be seen in the CH-based simulations of the evolution of real space of the sample (Figure 4.7) is the change in the shape of the scattering objects. During the transition from the early stage to the coarsening stage of spinodal decomposition, the system undergoes a change of shape from warm-like structures to sphere-like domains of dilute phase surrounded by dense phase. To investigate the effect of this process on the TTC, we performed the particle-based simulation of the change in the shape (Figure 5.20). It was found that moments with similar shapes of particles correlate much better than with different ones. Thus, to obtain the "square" feature, the transition should be immediate, followed by the final period of the constant shape. This process is not as drastic and simplified during the real LLPS, so its effect will not be as pronounced. Therefore, the change in the shape is also not the primary process influencing the "square" feature in TTC.

5.4.3 Additional figures
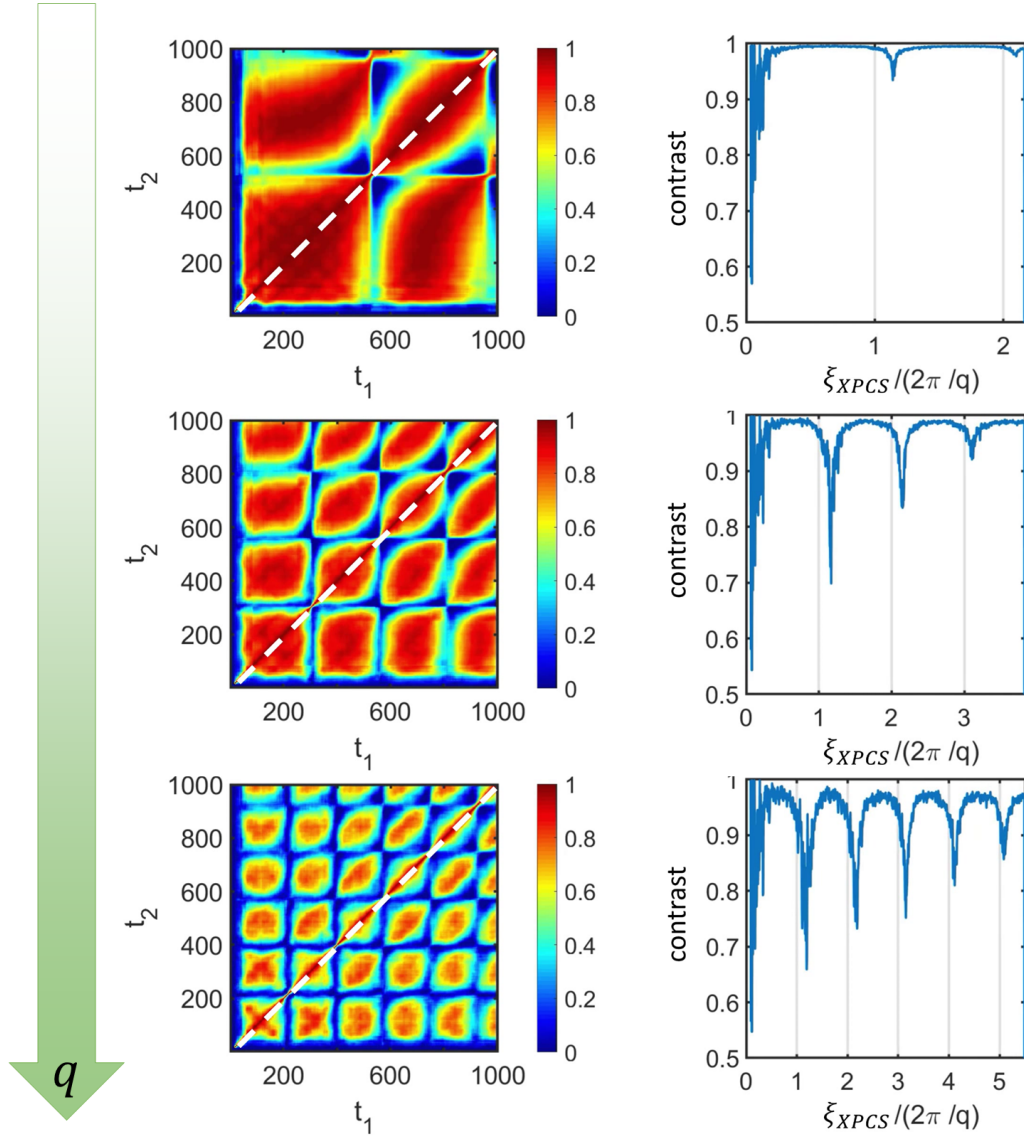
Figure 5.21: Extraction of the mean size for the particle-based simulation. Left row: two-time correlation function calculated for the model of identical particles which are growing with constant speed. Right row: dependency of contrast taken a pixel away from the diagonal in TTC on the left (marked with white dash line) as a function of an average size of the system $\xi(t_{age})$ divided to the size $2\pi/q$ corresponding to the investigated q-region. The q increases from top to bottom (follow the green arrow) in the range $q = [26, 66]$ pixels.
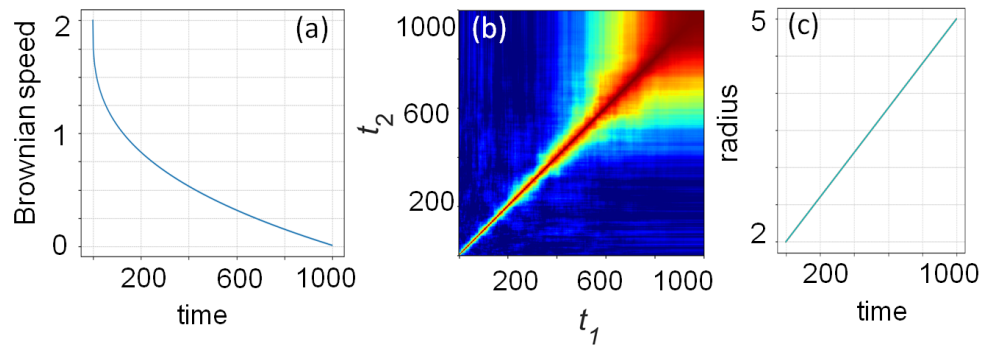
Figure 5.22: Particle-based simulation of the Brownian motion with the change in the Brownian motion rate with time and simultaneous growth. (a) Evolution of the Brownian motion rate. (c) Evolution of the radii of particles. (b) Corresponding TTC (also presented in Figure 5.9 (c)).
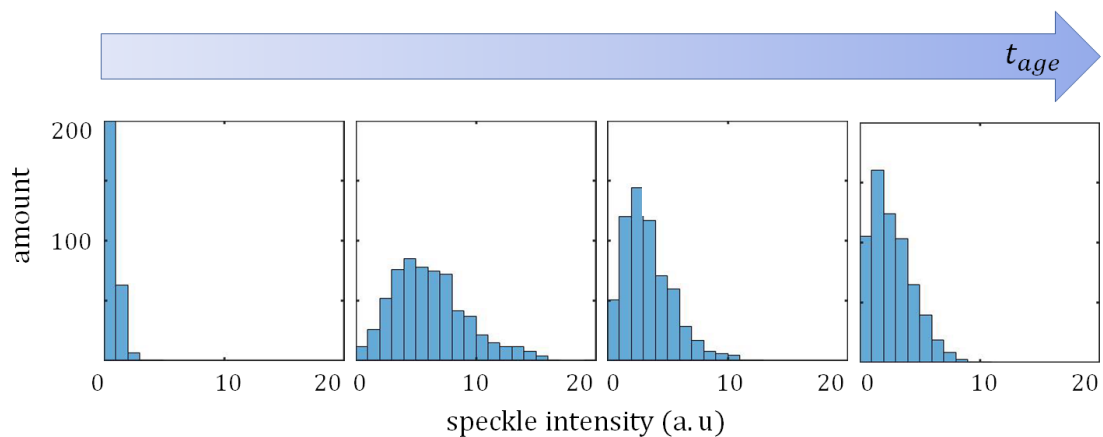
Figure 5.23: Evolution of distribution of speckles for 312 s experiment with time t_{age}. It can be seen that this distribution is not constant, which affects the fluctuation of contrast along the diagonal (see Section 5.2.4)

.
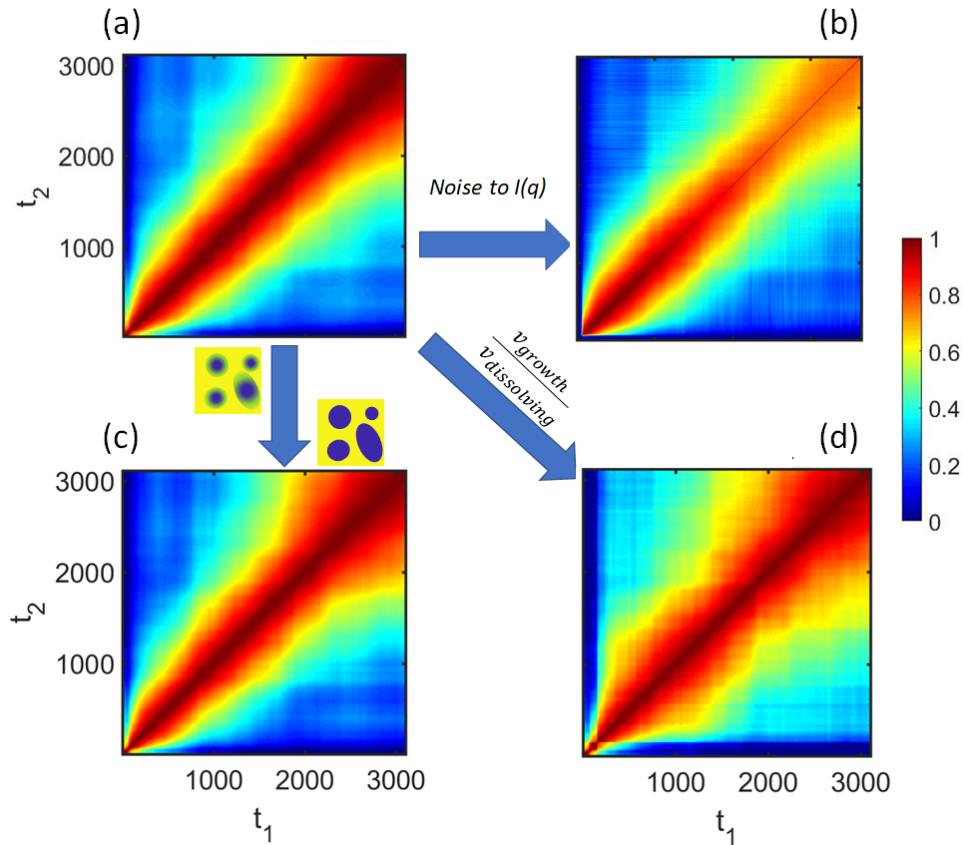
Figure 5.24: Summarizing of possible modifications of Cahn-Hilliard simulation pre-
sented in Section 5.2.4. **(a)** TTC for Cahn-Hilliard simulation (presented in Figure 5.1
(b)). Then we modified it with Reverse-Engineering **(c)-(d)** and by adding noise **(b)**. **(b)**
Adding the randomly distributed low-intensity noise to the scattering pattern of the
CH simulations results in the change of the contrast along the diagonal similar to the
experiment. Here is the example of adding noise of $max(I_{noise})/max(I) * 100\% = 4\%$,
which is similar to the experimental values of the background noise. It can be estimated
from the ratio of the I_{age} in Figure 4.9 at the initial stage when the sample was still
in a one-phase regime and the only scattering is coming from the background to the
intensity at the later stages. **(c)** TTC with the change of the concentration distribution.
All points with $u >= u_0 = 0.4$ were set to 1 and $u < u_0$ to 0 for all t_{age}. Such a dramatic
change results only in a slightly less visible "square", which means that changes in
concentration distribution are not the primary process resulting in the "square" for the
theoretical system. **(d)** TTC with increasing of the velocity ratio $v_{growth}/v_{dissolving}$ of
growing in the early stage and dissolving in the coarsening stage correspondingly. The
more the ratio, the better pronunciation of the "square" feature.

Chapter 6

Dynamics under complex flow evolution studied by XPCS

The following chapter summarizes the investigation of the flow effects on the dynamics studied by XPCS and connects the "wing" feature in the TTC with the flow retraction. The results presented in this chapter form the basis for an article of the same title, which is currently in progress. The experiment was conducted in collaboration with the group of Prof. Dr. Christian Gutt of Siegen University as well as the beamline scientist of ID02, ESRF, Thomas Zinn, who carried out the remote experiment on-site.

6.1 Introduction

THE high brilliance of the third and fourth-generation synchrotron light sources have made X-ray photon correlation spectroscopy studies (XPCS) [225] a powerful tool in studying the dynamics of materials. XPCS is used in various areas of soft condensed matter research: aging of colloidal gels and the colloidal glass transition [192], polymerization and gelation of polymers [218], phase transitions and phase separations [219, 220], diffusion [221] and many others. It enables to investigate mesoscale dynamics with a time scale range from minutes to picoseconds [172], which contains the important length/scale window for soft-matter studies [54, 64, 179, 219, 221, 298]. Furthermore, the advances of new XPCS methods can reduce the radiation damage efficiently, allowing to study biological systems [220, 222, 223, 299].

In a typical XPCS experiment of a liquid system undergoing a phase transition, the solution is often filled in a thin capillary. A challenge in studying the

dynamics of such a fluid system is the effect of flow, which can be generated by volume change, or introduced flow to re-fresh a sample to avoid radiation damage, and so forth. A large number of the studied samples are fluids, and therefore the investigation of the effect of flow is essential.

The investigated dynamics is reflected in the so-called two-time correlation maps (TTCs) [233], which are calculated from the scattering pattern of the sample. Among various influencing parameters, there are many XPCS studies of the flow impact on the obtained TTCs [61, 281, 300]. However, due to the complexity of the TTCs, the physical mechanism of many features remain elusive. So far, the literature is mainly focused on the investigation of the deliberately induced well-controlled shear flow with the flow used to reduce the X-ray beam-induced damage and to derive the experimental conditions under which it is possible to describe the diffusive dynamics of the colloidal particles [61, 300]. The only well-established feature in the TTC indicating the flow is the oscillation of the correlation function with time [61], which corresponds to the rate of the flow. This feature is visible only in the specific q and time window. Nevertheless, there are many phenomena where flow may appear as a side effect. However, when a liquid (soft-matter) system is exposed to a rapid isothermal change of pressure or isobaric change of temperature, it undergoes a volume adjustment or the volume change during the solid-liquid phase transition. This may cause a complex, uncontrolled flow. The resulting TTCs and the corresponding dynamic properties of the systems can not be understood with the current understanding of the impact of the flow on the TTC [61, 300].

Here we focus on the liquid-liquid phase separation (LLPS) in a protein system. The system undergoes a transition from one single-phase regime to two phases by rapid change of the environmental conditions (temperature or pressure) accompanied by the non-constant flow. In Chapter 4 the kinetics and dynamics of such a system was followed, and it was found that the dynamics can be decoupled with the kinetics relaxation [220]. Another study discusses the impact of the interplay between LLPS and glass formation on the microscopic dynamics [223]. Importantly, to avoid the flow effects, the experiments were performed near the end of the capillaries, where the volume expansion is the smallest. In the middle of capillaries, with great regularity, the resulting TTCs demonstrate "wing"-features (Figure 6.1). This type of TTC is not unique to LLPS processes and may also appear for other soft-matter systems. To the best
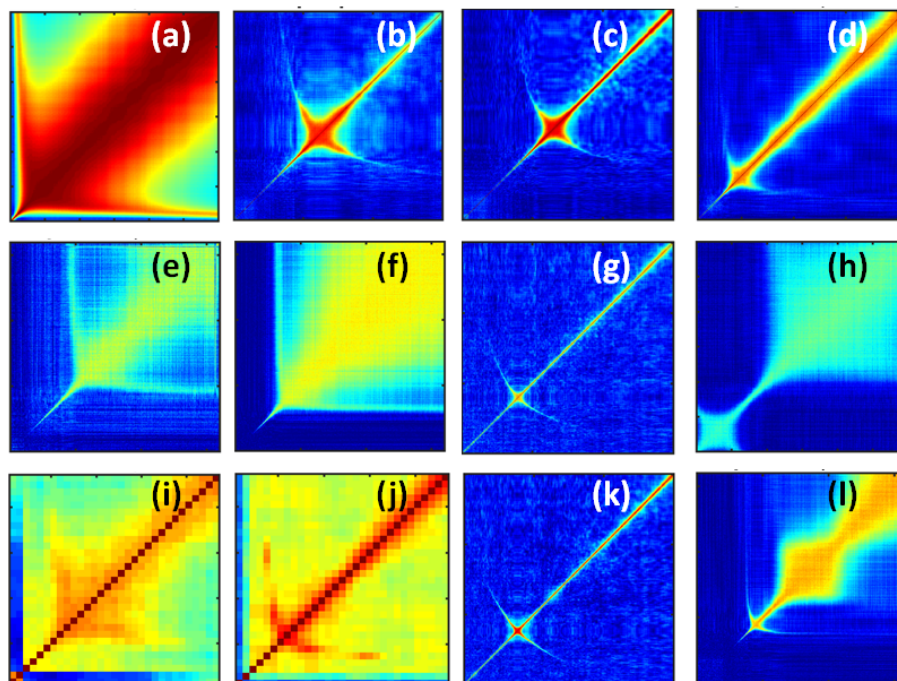
Figure 6.1: Examples of TTC maps with "wing" features which with enviable regularity appears for phase/state transition XPCS experiments on different soft-matter systems: (a) - melting of chocolate, (b, c, g, k) - LLPS of BSA–YCl$_3$, (d, e, f) - LLPS of IgG–PEG, (h,l) - gelation of egg-white with NaCl, (i,j) - LLPS of BSA–HoCl$_3$-LaCl$_3$. The experiments were performed on a micrometer length-scale on different synchrotron sources with different exposure, delay, and waiting times and under different temperatures. For specific details, please, contact the author. The colormap is jet; the colors correspond to the value of $G(q, t_1, t_2)$ from 0 to 1.

of our knowledge, the interpretation remained elusive. This chapter correlates the "wing"-feature with the flow-induced retraction and supports this statement with simulations. Our findings broaden the knowledge of the impact of flow on the dynamics and also demonstrate the possibility of revealing flux information based on TTCs.

6.2 Experimental parameters

The XPCS experiments were performed with the model system of the globular protein bovine serum albumin (BSA) in the presence of trivalent salt YCl$_3$ [44]. The phase behavior of this system is discussed in Section 1.4.2, while the sample preparation is described in Section 3.1.

The XPCS experiments were performed in the USAXS mode at the ESRF,

beamline ID02 in Grenoble, France (see Section 3.2). The incident X-ray energy was varied around 12.3 keV (Table 6.1). The sample-to-detector distance was 30.7 m. A q range of $2\ \mu\mathrm{m}^{-1}$ to $16\ \mu\mathrm{m}^{-1}$ was investigated, where $q = 4\pi/\lambda \cdot \sin\theta$ and 2θ is the scattering angle.The data were collected by a Eiger 500K detector (see Table 3.1). The dense phase of the protein solution was filled into quartz capillaries of 1 mm diameter and stabilized at 10°C before the XPCS measurements. The LLPS was started by a rapid temperature jump from 10°C to different temperatures (T=[32, 52] °C) using a Linkam stage [45, 220]. The measurements were started simultaneously with the temeprature jump. Further details about the experiment (e.g. beam size, exact energy, flux) can be found in the Table 6.1.

Table 6.1: Experimental parameters for Dataset 1 (Figure 6.3) and Dataset 2 (Figure 6.4).

Parameters	Dataset 1	Dataset 2
Energy (keV)	12.28	12.46
Beam size ($\mu m \times \mu m$)	22×25	35×35
Flux (ph/s)	1.2×10^9	3.2×10^{10}
Heating rate (°C/min)	80	100
Number of frames	1000	600
Exposure (s)	0.1	0.005
Delay (s)	0.29	0.095

Series of 2D speckle patterns were collected with different frames, exposure, and delay times (see Table 6.1), which contains the dynamic and kinetic information of the investigated sample. The analysis of the kinetics consisted of obtaining the scattering intensity profile and the evolution of its peak position (spinodal peak [46, 47]). The azimuthal average of the scattering intensity for different radii was used to obtain the profile $I(q)$ for each frame (time). During the analysis of the kinetics, the USAXS profile collected at 10°C before heating was used as the background.

The microscope experiment was performed on the model system of the concentrated BSA (328 mg/ml) with the addition of the glitter from the Dior Diorshow 5 Couleurs Designer Eyeshadow Palette 208 Navy Design [301]. The liquid glitter sample was filled into a 1.5 mm capillary and heated with the Linkam stage with 150 °C/min rate from 30°C till 45°C. The AxioScope A1 from Carl Zeiss Microscope (Oberkochen, Germany), which was used, allows automatized time-dependent picture series by the software Zen 2012.

6.3 Results and discussions

6.3.1 Experiment

For the analysis of the dynamics, the 2D speckle patterns obtained from XPCS-USAXS experiments were used to calculate two-time correlation function (TTC) $G(q, t_1, t_2)$ [225]:

$$G(q, t_1, t_2) = \frac{\overline{I(t_1)I(t_2)} - \overline{I(t_1)} \cdot \overline{I(t_2)}}{[\overline{I^2(t_1)} - \overline{I(t_1)}^2]^{\frac{1}{2}} \cdot [\overline{I^2(t_2)} - \overline{I(t_2)}^2]^{\frac{1}{2}}}, \tag{6.1}$$

where the average is over pixels with the same momentum transfer $q \pm \Delta q$. Here t_1 and t_2 are the times at which the intensity correlation is calculated.

The correlation function, $g_2(q, t_{age})$, can be determined by both horizontal and diagonal cuts from the TTC [232]. Here we used the diagonal ones which will be discussed later in the text. Using the Kohlrausch-Williams-Watts relation, the characteristic relaxation time, τ, and the Kohlrausch exponent (KWW), γ, $g_2(q, t_{age})$ can be expressed as functions of q and the absolute experimental time t_{age} [267]:

$$g_2(q, t_{age}, \bar{t}) = \beta(q) * exp(-2[\bar{t}/\tau(q, t_{age})]^{\gamma(q, t_{age})}), \tag{6.2}$$

with $\bar{t} = t_2 - t_1$ as a delay time and $t_{age} = (t_1 + t_2)/2$. The speckle contrast is β and it depends on the incident beam properties and the experimental setup and for ergodic processes can vary from 0 (incoherent scattering) to 1 (fully coherent scattering).

For the typical LLPS scattering experiment, a liquid sample is filled into the capillary that is placed horizontally to exclude the influence of gravity (Figure 6.2 (a)). Usually, the scattering is collected from any point in the capillary center, excluding ones close to the open top. There is a well-known modification of the spinodal decomposition due to the shear stress, which results in the anisotropic scattering [302, 303]. Measuring away from the walls of the capillary allows to avoid those modifications in the best way (Figure 6.2 (b)) since the shear stress is zero at the center of a capillary. It should be noted that all of the experiments discussed in the current chapter were performed at positions with stable
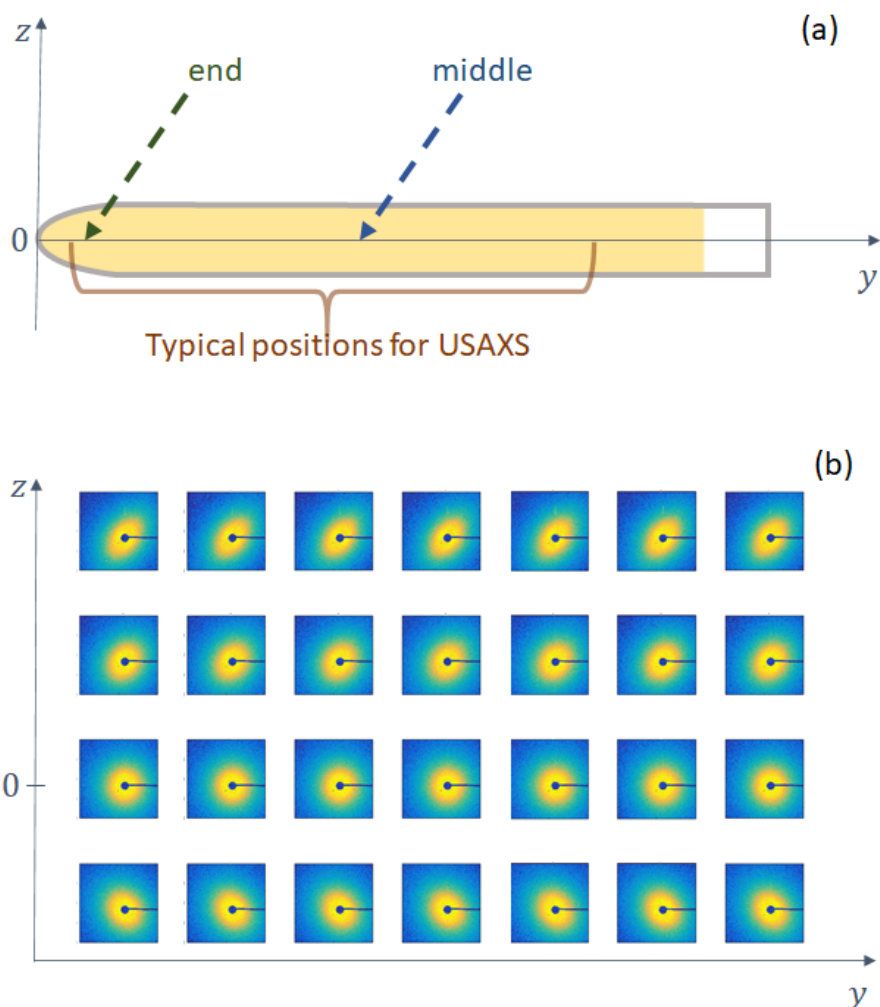
Figure 6.2: (a) The sketch of the capillary in XPCS-USAXS experiments. y-axis marks the horizontal direction, and the z-axis marks the vertical direction. The beam is perpendicular to the figure plane. A dark-orange squiggly bracket shows the typical position range for USAXS experiments. The green and blue dash lines inside this range mark the "end" and "middle" positions inside of the capillary, which are discussed in the main text ($z = 0$, different y). (b) The 2D scattering patterns as functions of y and z. When approaching the capillary walls (moving away from the $z = 0$ point), the spinodal decomposition modifications occur, which leads to the anisotropic scattering. The bigger the distance from $z = 0$, the more anisotropy is there. The experiments discussed in the current paper were performed with stable symmetrical 2D scattering patterns ($z = 0$).

isotropic 2D scattering patterns.

A typical TTC with a "wing" feature for the USAXS-XPCS experiment of LLPS is shown in Figure 6.3. This feature is visible as a rapid increase in the
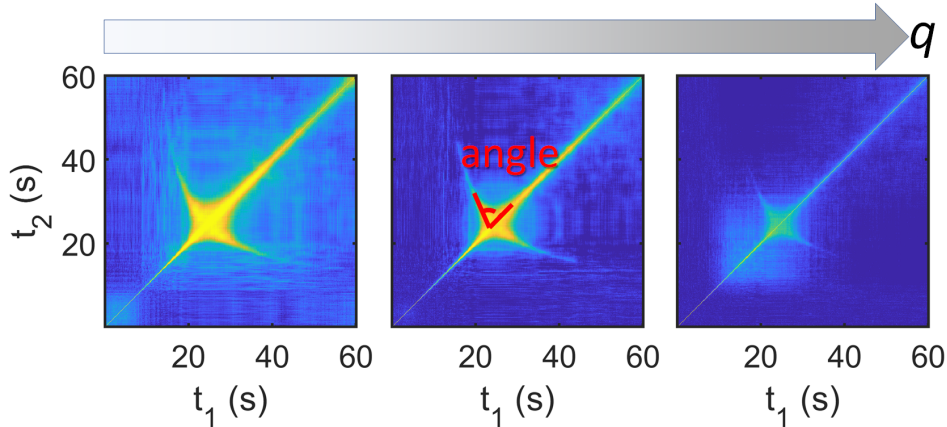
Figure 6.3: TTC maps with a "wing" feature for BSA–YCl$_3$ system after LLPS due to a temperature jump from 10 °C to 47.5 °C for different q-values: $3.7\mu m^{-1}$, $5.6\mu m^{-1}$ and $8\mu m^{-1}$ (from left to right). It is clearly seen that the "wing" feature becomes narrower with the increase of q. The "wing" angle is marked with red. The colormap is parula, the colors correspond to the value of $G(q, t_1, t_2)$ from 0 to 0.8.

relaxation time followed by a rapid decrease. One of the main characteristics of the "wing" feature is that it appears at the same time t_{age} for all q-values. For the experiments on BSA–YCl$_3$ system, the visibility of the "wing" decreases with the increase of the q (follow Figure 6.3). Another characteristic of the "wing" is its shape: the main angle between the feature and the diagonal (marked with red in Figure 6.3) and the curvature. For the example, in Figure 6.3 the "wing" is curved, and the main angle is around 60 degrees. The shape is independent of the q-value.

However, when the measurements were performed near the sealed end of the capillary (a few mm away), this "wing" feature in the TTC disappeared (Figure 6.2 (a)). The comparison of two 300s XPCS-USAXS experiments in the end and the middle of the capillary is presented in Figure 6.4. It can be seen that the TTC from the middle of the capillary shows two "wing" features (Figure 6.4 (a)) with the first one in the early time consistent with the previous observation in Figure 6.3. In contrast, the one from the end of the capillary shows a smooth change in the relaxation time with time (Figure 6.4 (b)). The dynamics of the latter is characterized by clear two-stage behavior. The relaxation time increases quickly initially, then enter into a steady stage with the relaxation time slowly varying with time. This behavior is in good agreement with the previous studies in Chapter 4 and [220, 223].

For a quantitative comparison, the $g_2(q, t_{age})$ functions along the diagonal of
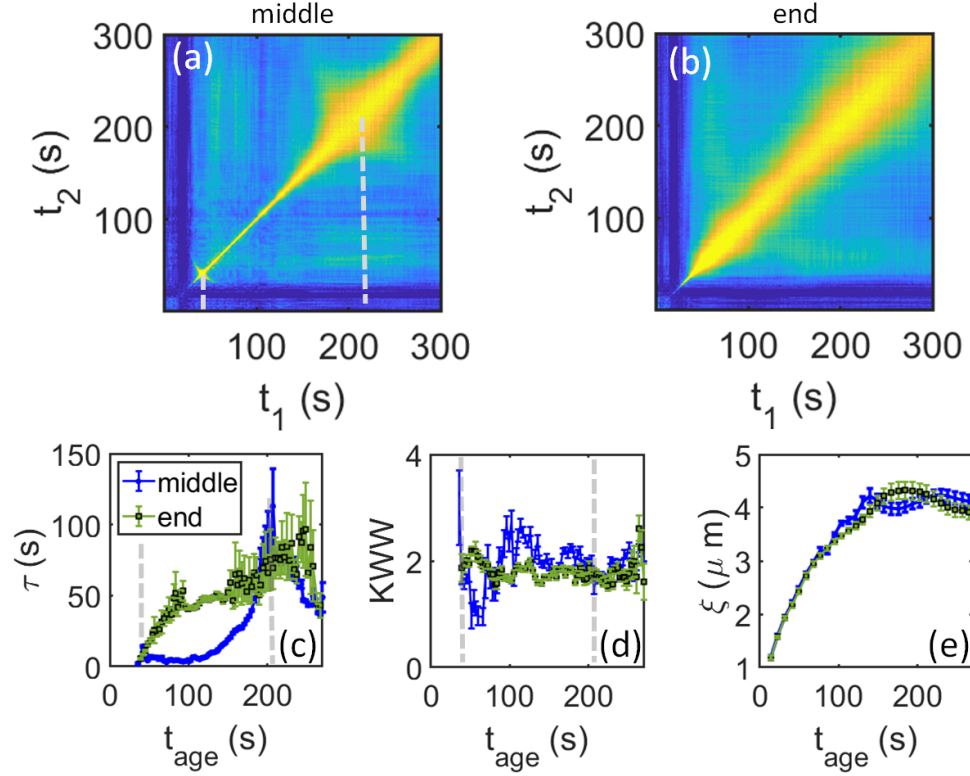
Figure 6.4: Comparison of the kinetics and dynamics of the sample undergoing LLPS in the end and the middle of the capillary. (a) The experimental TTC map for the middle of the capillary demonstrates two "wing" features, pointed with the grey dash line. (b) The experimental TTC map for the end of the capillary does not include the "wing" feature. Relaxation time (c) and KWW exponent (d) for the middle (blue) and end (green) of the capillary. The values at the time t_{age} when the "wing" appears (grey dash lines) are independent of the measurement position. Characteristic length evolution on (e) shows similar behavior for different positions.

TTC were fitted using Equation (6.2), and the resulting evolution of relaxation time and KWW exponent were plotted also in Figure 6.4 (c) and (d), respectively. Furthermore, the characteristic length, ξ, determined from the peak position in the corresponding static $I(q)$ [46, 47] was plotted as a function of time in Figure 6.4 (e). Interestingly, although the relaxation time between the wings measured in the middle of the capillary is much shorter than that measured near the end of the capillary, by the time the "wing" appears, the values are rather similar (marked by a grey dash line in Figure 6.4). In both cases, the KWW exponent, γ, is around 2 indicating the dominating of driven dynamics. Despite the dramatic change in the dynamic maps, the static structure development of the system (i.e., the characteristic length as a function of time) nearly fully

overlaps. This indicates that the dynamic change does not influence the static property (Figure 6.4 (e)). The results are reproducible at different q-values. Thus, there is a strong position dependency of the measured dynamics with or without the "wing" features in the TTCs, rendering an interpretation of the dynamic property difficult.

The "wing" feature may appear during USAXS-XPCS experiments on many other soft-matter systems (Figure 6.1), which undergo different dynamical processes (e.g., gelation, LLPS, melting). Nevertheless, they have in common the requirement for a rapid change in the environmental conditions (e.g., temperature). Thus, one possible reason for the "wing" feature is that these experiments are accompanied by changes in the volume, which may result in the flow of liquid samples. The temperature overshot, and subsequent equilibration may lead to a temporal flow and even a retraction. To demonstrate this hypothesis, we performed a modified Cahn-Hilliard simulation by introducing a tunable laminar flow.

6.3.2 Simulation of laminar flow

Similar to Section 4.3.2 and Section 5.2.2, the Cahn-Hilliard equation was used to describe a system undergoing spinodal decomposition (SD). Equation 4.4 was solved numerically on a 2D rectangular grid $N_x \times N_y = 200 \times 512$ pixels for 30400 time steps with $\Delta t = 0.09$. The initial concentration for each point in the space was defined as random noise fluctuations with an amplitude of 0.05 around $u_0 = 0.4$, which corresponds to the dense phase (similar to the experiment) so that these noise fluctuations have a uniform distribution. The temperature parameter T was set to $0.05T_c$. Thus, the total simulation time is $30400 \times 0.09 = 2736$ arb. units, which is long enough to include both the early and coarsening stage of the SD and can be compared with several hundred seconds of the real experiment [220, 223] (see Section 4.3.2 for details). Since experimental 2D scattering patterns do not show any asymmetry, it is possible to conclude that there is no change in the spinodal decomposition process due to the flow and, thus, the use of the classical Cahn-Hilliard equation at this stage of simulation is reasonable.

The rectangular shape for the 2D grid was chosen to imitate the flow of the sample. The scheme of this imitation is presented in Figure 6.5 and includes the
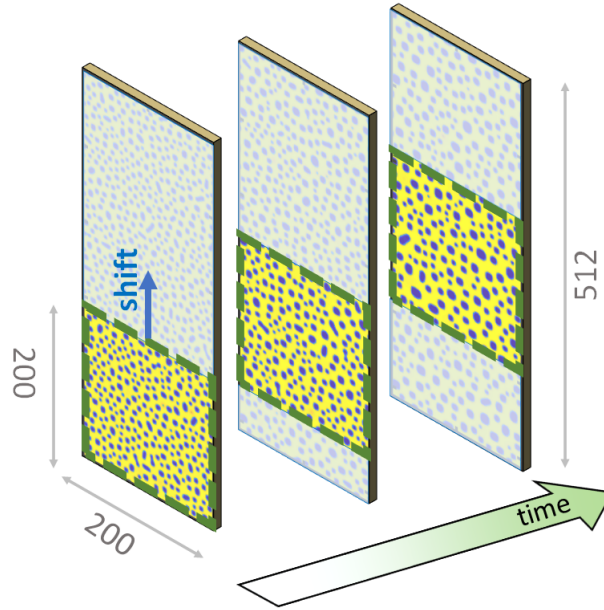
Figure 6.5: Scheme of the modification of the results of CH simulation to imitate the flow. The calculation of the concentration map by the CH simulation is performed on the 2D grid of size 200×512 pixels. Here, the evolution of this map is presented for three different moments in time. The area of interest is limited to 200×200 pixels and marked with a green dash square and brighter colors of the inside part. Shifting the particles during the flow is the same as moving the area of scattering (blue arrow). The time-dependency of this area of interest represents the evolution of the domains during LLPS with the imitation of flow. The scattering was calculated only for this chosen part of the 2D grid.

following. The shift of the particles during the flow can be considered as the shift of the scattering area. After completing the CH simulation, the scattering was calculated only from the chosen part of the 2D grid. The area of interest was limited to 200×200 pixels at each moment. This area shifted with time with the given speed along the N_y. The shift imitates the flow and can be manipulated by changing the speed and direction. The grid was interpolated at each time step to overcome the limitation of the shift step to be multiple of the pixel size. Thus, the shift step of less than a pixel was possible. After such a modification of the CH simulation, the area of interest includes both - the classical CH and the controlled laminar flow at the desired direction/directions.

First, the evolution of the 2D field of concentration is calculated. Then it is possible to calculate the scattered image (i.e., an image in reciprocal space) $I(\mathbf{q}, t_{age})$ of the system for each time step, which is the square of the magnitude of the 2D fast Fourier transform of the fluctuations of the concentration [101].

The obtained 2D scattering pattern can be treated similarly to the raw data for the XPCS-USAXS experiment (Section 6.3.1 and Equation (6.2)).

In Section 5.2.3 we have already investigated the interplay between the effects of different simultaneous dynamics on the TTC. There it was shown that the visibility of features on the TTC depends on the values of the characteristic relaxation times and their comparison for different dynamical phenomena (Figure 5.8). Using this as a starting point, it would be logical to assume that the relative importance of the flow-induced effects on the TTCs compared with the dynamics of LLPS should correlate with the ratio between the relaxation time of the flow, τ_{flow}, and the relaxation time of the system, τ [61]. The relaxation time of the flow can be estimated as [300]:

$$\tau_{flow} \propto 1/(q \cdot v_{flow}) = 1/(q \cdot dshift/dt_{age}). \tag{6.3}$$

Thus, the final TTC features will depend on q and the behavior of the $shift$ variable.

As the first step, we investigated the impact of different flow rate values on the q-dependency of TTC maps. To begin with, we will work with a simplified model in which the τ_{flow} does not change with time. Thus, $dshift/dt_{age} = const$. That is a linear change in the $shift$ parameter. Further, for qualitative analysis, instead of studying the behavior for each specific $shift$ value, we will divide all possible cases into three groups based on the comparison of the total shift, $shift_{total} = \int shift \, dt_{age}$, with the investigated area ($N_x = 200 pixel$). The first group is called the large-scaled flow and relates to the case when $shift_{total} > N_x$ or comparable, which leads to a renewal of the scattering volume due to the flow. For the second group – $shift_{total} << N_x$ and, thus, the majority of the scattering volume remains the same. The last group describes the situations when there is an absence of flow. The simulations of the LLPS with a short-scale flow, large-scale flow, and the absence of the flow are presented in Figure 6.6. Since the flow rate is proportional to the $shift$ variable, the retraction of the flow can be detected in the sign change of the $dshift/dt_{age}$, which for Figure 6.6 was set to $t_{age} = 1485$.
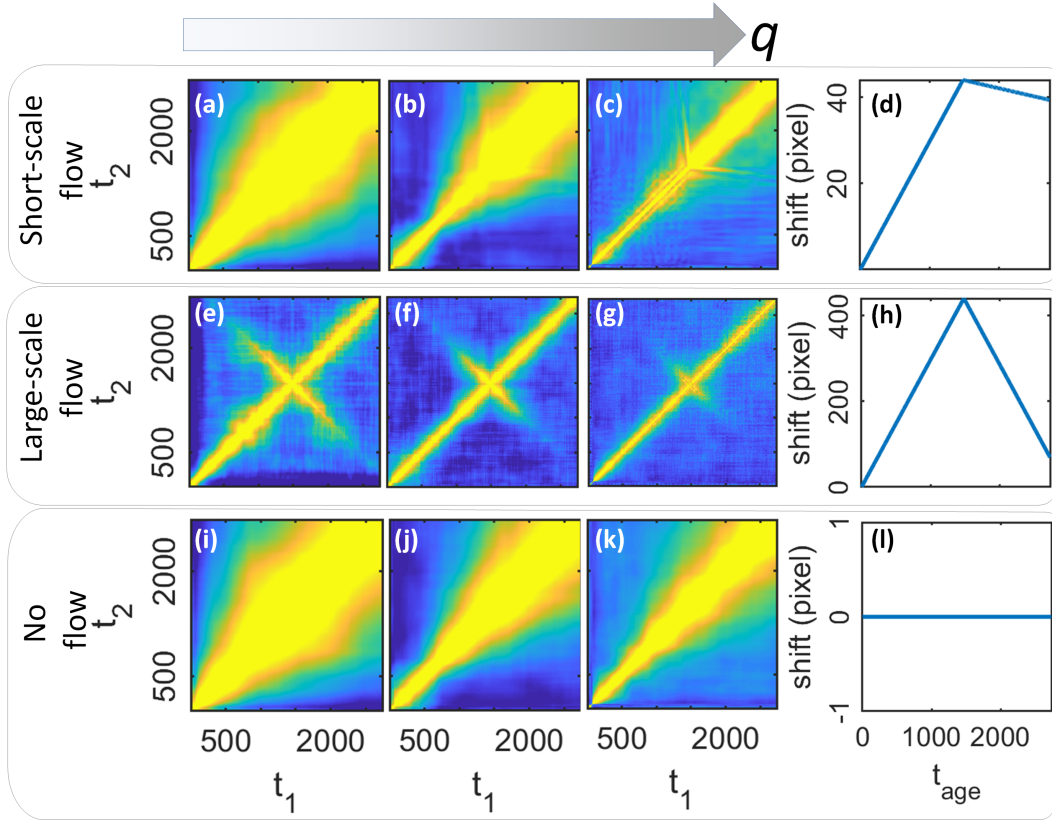
Figure 6.6: Impact of the flow of different scales on the simulated TTC maps for different q-values simulated by the modified Cahn-Hilliard: short-scale flow (a-c), large-scale flow (e-g), and no flow (i-k). The q-values increase from left to right (marked with the grey arrow on the top) within the row and corresponds to 12, 8 and 3 pixels sizes in the real space. Within the column the q-value is the same: (a,e,i), (b,f,j) and (c,g,k). The value of shift of the area of interest is presented on (d,h,l) for short-scale, large-scale flow and the absence of flow correspondingly.The retraction time is set to $t_{age} = 1485$. The colormap is parula, the colors correspond to the value of $G(q, t_1, t_2)$ from 0 to 0.8. The "wing" feature appears at the time of the change in the flow rate.

It can be seen that the system without the flow (classical CH) does not show any "wing" features (Figure 6.6 (i-k)) and only demonstrates the acceleration of the dynamics (shorter relaxation times) with the increase of the q. The addition of the laminar flow to the simulation leads to three situations (Figure 6.6 only for $t_{age} < 1485$): no change in TTC (a-b), acceleration of the dynamics (c-g), or appearance of the oscillatory correlations (c). All of these effects are consistent with the literature [61, 179, 281]. Meanwhile, the retraction of this flow leads to the appearance of the "wing" feature in the TTCs at the time of the retraction (Figure 6.6 at $t_{age} = 1485$), which, as far as we know, has not been investigated previously. For the slow flow, which leads to the short-scale movement of the
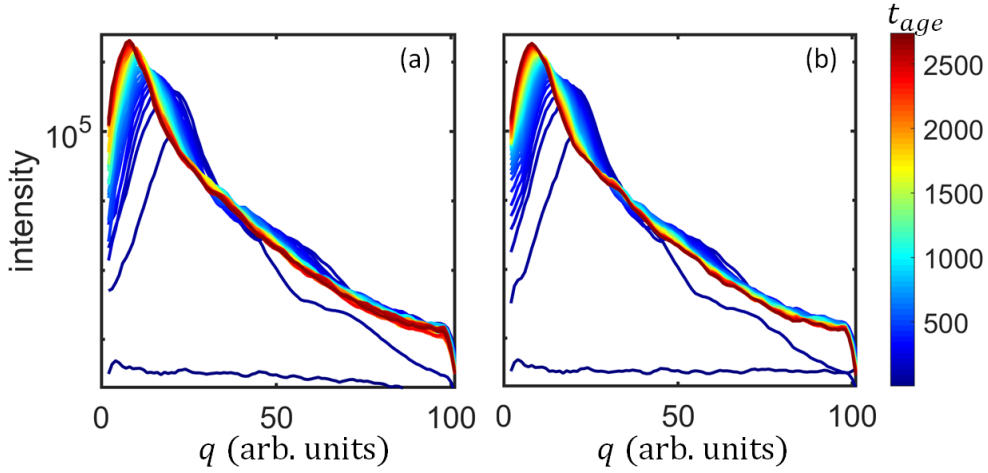
Figure 6.7: Simulated intensity profiles were obtained from the Fourier transform of the real space image with modification by the large-scale flow (a) and without (b). The $I(q)$ demonstrates independence from the flow.

sample, the low q-values are not affected by the flow, and the visibility of the "wing" feature increases with an increase of q (follow (a-c) in Figure 6.6). This is caused by a higher sensitivity of smaller domains to the shift. In contrast, for the fast flow, which leads to the large-scale movement, the visibility of the "wing" is higher for a lower q-value which is similar to the experimental results. Thus, estimating τ_{flow} value with Equation (6.3), it can be concluded that the system dynamics is enhanced when $\tau_{flow} \ll \tau$. In other cases, the changes are not significant. It is important to note that despite significant changes in dynamics, the kinetics remains similar to the system without the flow (Figure 6.7).

The TTCs obtained for the large-scale flow are similar to the experimental ones, so for further research, we will conduct simulations with this order of flow. Therefore, applying the flow classification used for the simulations to the experiment, it turns out that in order to obtain such experimental TTCs having a beam size of 20-100 micrometers (typically used in our experiments), we expect that the shift due to thermal expansion should be of the similar range.

The "wing" feature in Figure 6.6 (e-g) has a symmetrical shape with a main angle of 90 degrees to the diagonal. Similar to the experiment, these properties are independent of the q-value. To further understand the shape of the "wing" feature, we investigated the dependency of the TTCs on the ratio of the flow rate before and after the retraction (Figure 6.8), v_{before} and v_{after} respectively. The "wing" angle is very sensitive to this ratio: for $v_{before}/v_{after} < 1$ the angle is
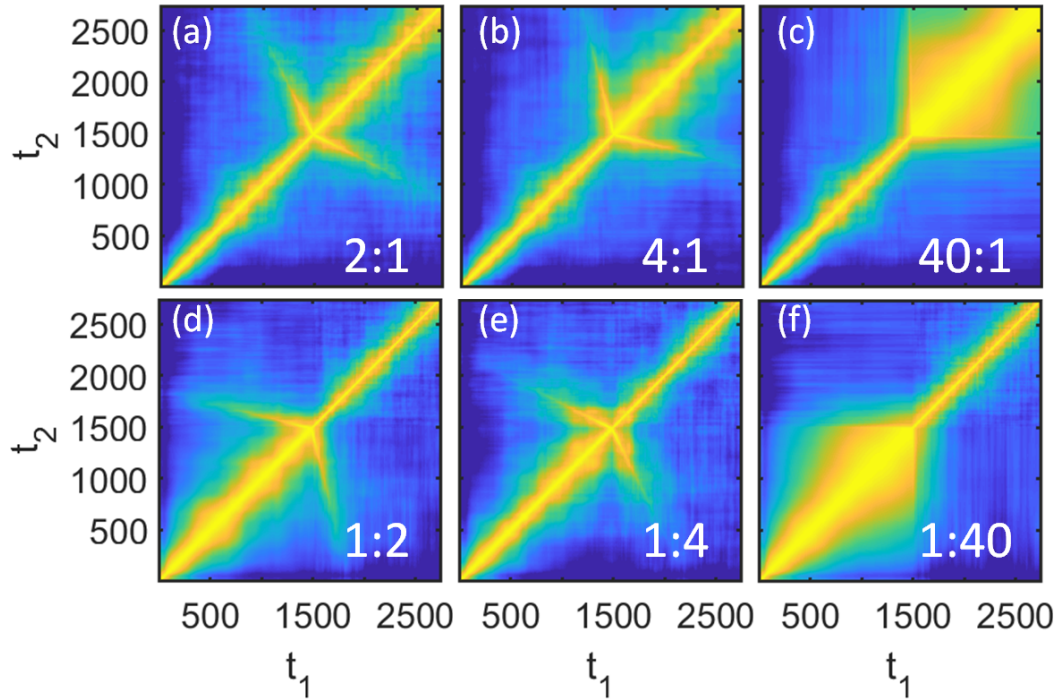
Figure 6.8: The value of the ratio of the flow rates before and after the change in the flow results in different shapes of the "wing" feature. Simulated TTC maps for 2:1 (a), 4:1 (b), 40:1 (c), 1:2 (d), 1:4 (e), 1:40 (f) flow rates ratio. The 1:1 ratio and the absence of the flow were presented in Figure 6.6 (e) and (i) correspondingly. All TTCs are shown for the same q-value. The colormap is parula; the colors correspond to the value of $G(q, t_1, t_2)$ from 0 to 1.

acute and once the ratio is $v_{before}/v_{after} > 1$ the angle becomes obtuse. The larger is the ratio, the smaller is the angle. The angle varies from 45 degrees, when $v_{before} \gg v_{after}$ (Figure 6.8 (c)), to 135 degrees, when $v_{before} \ll v_{after}$ (Figure 6.8 (f)).

This observation leads to the idea that the shape of the "wing" can be modified by implementing the nonlinear evolution of the flow rates (Figure 6.9). In this case, the ratio v_{before}/v_{after} is not constant anymore. The evolution of the ratio with time leads to the curvature of the "wing". Thus, knowing the "wing" angle and curvature on the experimental TTCs, one can estimate the flow ratio evolution.

As described above, the appearance of a flow can fundamentally change the TTCs, distorting the relaxation time. However, at the moment when the "wing" occurs, the derivative of the flow rate is zero. Thus, the state of the system at the time that the "wing" feature appears corresponds to a steady state
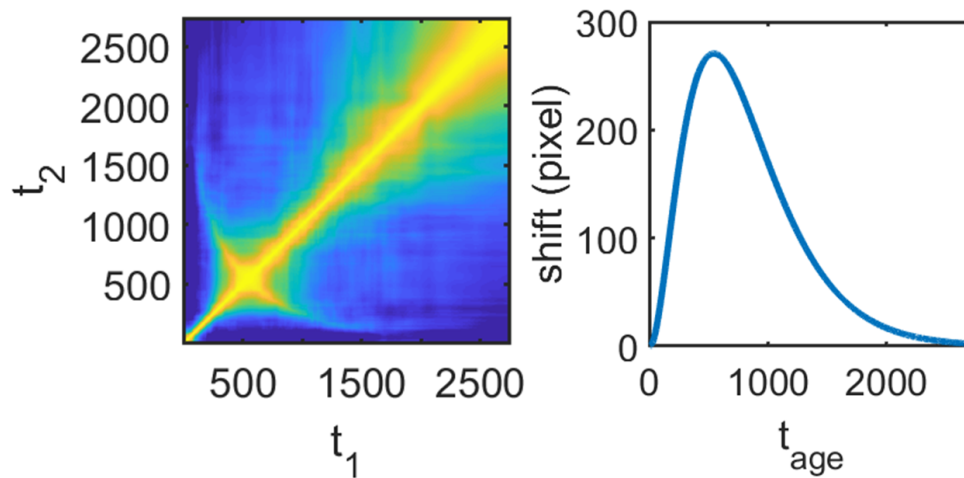
Figure 6.9: Example of the "wing" feature with curvature on simulated TTC (left picture), which is the result of the nonlinear change in the flow rate (right picture).

with the minimum influence of flow. In Figure 6.10 the g_2 function cuts along the "wing" feature for different values of flow rates with the ratio equal to 1 are presented. It can be seen that the obtained g_2-functions are independent of the flow rates. Thus, the relaxation time and KWW exponent calculated from the "wing" feature can be considered a good estimation for the system without the flow. This information is important when a comparison is needed for a system following the same processes under different conditions, such as heating to the different final temperatures. With the current approach, the flow effect can be minimized. This simulation result is consistent with the experimental observation in Figure 6.4, where diagonal cuts were used as a good approximation for the direction along with the "wing" feature.

Similar procedures can be applied to more simple systems, e.g., with Brownian motion, which is typical for colloids. There, retraction of the flow will also lead to the appearance of the "wing" features on TTCs. This is in line with the remark made earlier that such features are common to many systems. Thus, the obtained results for the flow retraction remain valid regardless of the system.

6.3.3 Microscope observations

The assumption about the generality of the phenomenon for different samples leads to the idea that one can try to evaluate the flow retraction effects in real measurements using a microscope, bypassing the technical issues associated

131
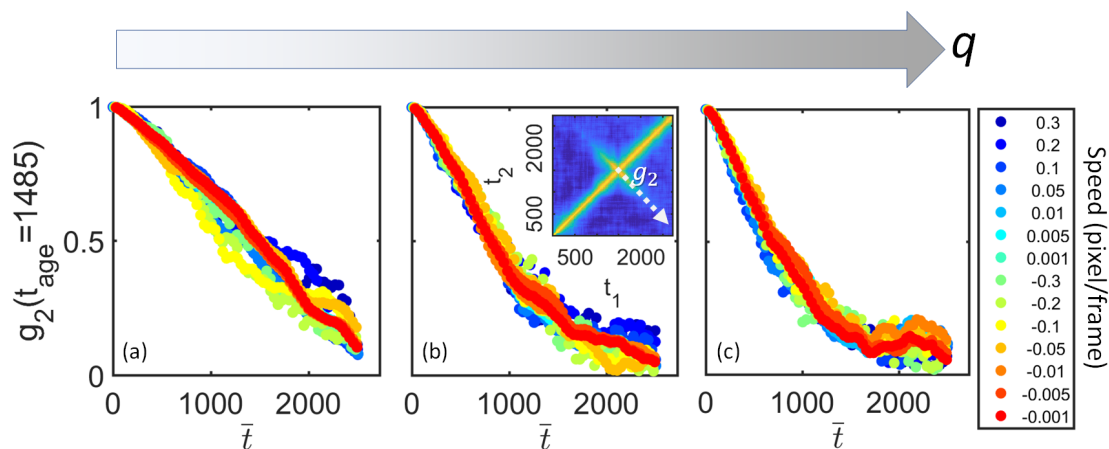
Figure 6.10: Comparison of the diagonal g_2–cuts of the "wing" feature (shown with dot white line in the inset of (b)) for different values of speed of the flow with ratio 1:1 (values shown in the legend) for different q-values ($q = [17, 27, 37]$ pixels).

with the opacity of the measured BSA-YCl$_3$ system. To do this, a transparent sample should be selected with the presence of particles that are clearly visible under a microscope. Here, a concentrated BSA with the addition of glitter from the Dior Diorshow 5 Couleurs Designer Eyeshadow Palette 208 Navy Design was taken as a test sample [301] (see Section 6.2). The resulted glitter liquid has similar order of viscosity to the original sample and is transparent enough to investigate the flow of the glitter particles induced by the rapid heating by the microscope.

The results of this investigation are summarized in Figure 6.11. The microscope images for different times with the detection of particles for further tracking are presented in Figure 6.11 (a). These particles clearly show the shift from their initial positions (Figure 6.11 (d), (e)), which is an indication of the heat-induced flow in the capillary. In the first minute, this shift reaches values in the range from several tens to a hundred micrometers. This order is consistent with the assumptions in Section 6.3.2. However, it turned out that the flow in the real sample was more complicated. Despite the overall similar motion, the reaction of the particle on the retraction is not simultaneous (Figure 6.11 (d), (e) and Appendix Figure 6.12). Thus, the real flow is heterogeneous. Furthermore, there is a change in the direction of the flow during the retraction.

Finally, the calculation of the TTC based on the microscope images (Figure 6.11 (f)) shows that for the q values of the USAXS range "wing" feature appears at the time of retraction, which supports conclusions of this chapter. Nevertheless,
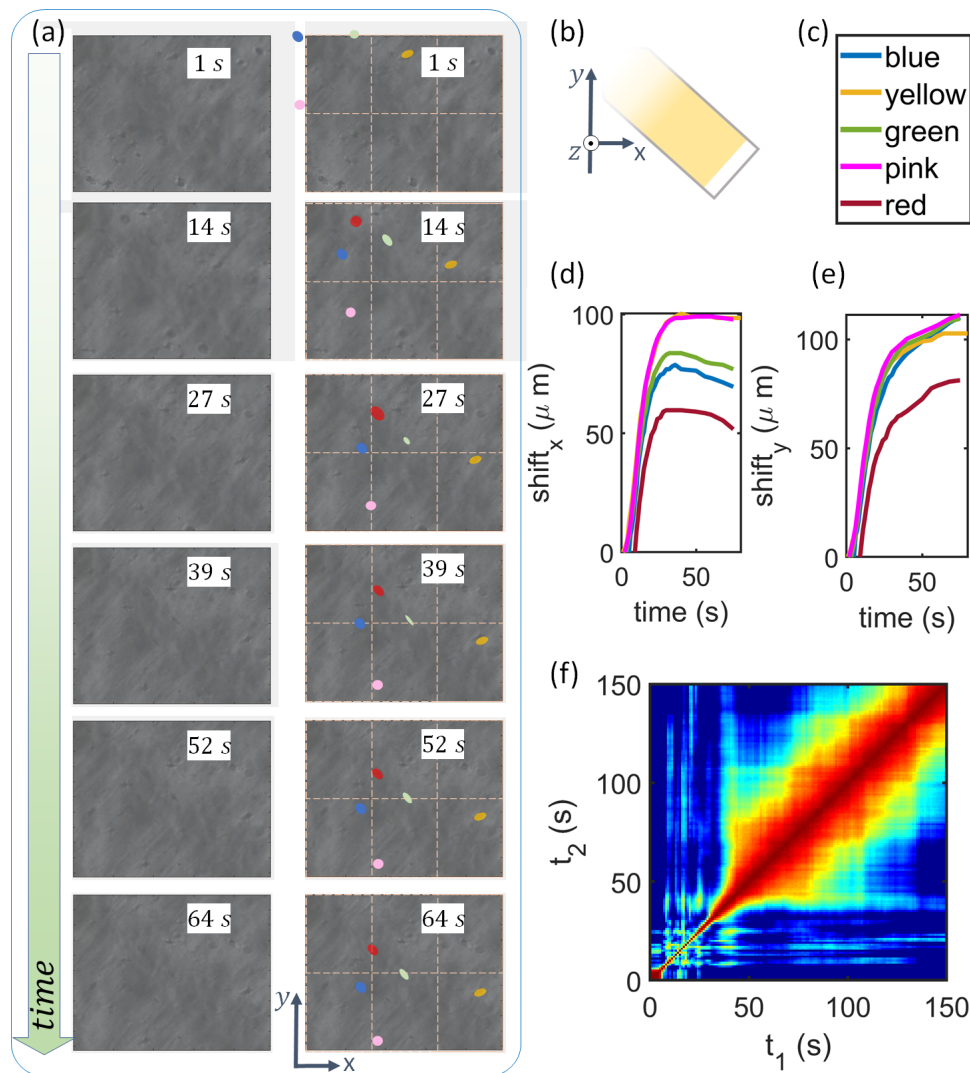
Figure 6.11: Investigation of the flow of the glitter liquid in capillary during heating from 30°C till 45°C with a heating rate 150°C/min by microscope. (a) Original microscope images (left column) and images with the labeling of some of the detected particles by different colors (right column) for different times. (b) The position of the capillary relative to the axes of the microscope. Top view. (c) Labels for (d) and (e) graphs. Colors correlate with the detected particles on (a). Projections of the shift of these particles as a function of time for x-axis (d) and y-axis (e). There is a retraction of the $shift_x$ around 40 s, which, however, is taking place at a bit different times for different particles. (f) TTC map calculated from the microscope images for $q = 0.8 \ \mu m^{-1}$ demonstrates the presence of the "wing" feature at the time of retraction.

it is important to note that for the microscope experiment, only the 2D real space image can be investigated. Furthermore, the sample was filled in 1mm capillary and heated with 150°C/s rate from 30°C till 45°C, while for the experiment presented in Section 6.3.1 the sample was filled in 1mm capillary and heated

with 100 °C/s rate from 10°C till 40-50°C. Thus, the numerical comparisons may be ambiguous.

6.4 Conclusions

In summary, in Chapter 6, it was demonstrated that a flow retraction in liquid systems during XPCS measurements leads to the "wing" features in the two-time correlation functions (TTCs). For the short-scale flow, the visibility of the "wing" feature increases with the q, while for the large-scale flow, it decreases. The shape of the "wing" depends on the ratio of the flow rate before and after the retraction. The curvature of the "wing" is the result of the nonlinear evolution of these flow rates. It was also shown that the state of the system at the time that the "wing" feature appears corresponds to a steady state with the minimum influence of flow. These effects of flow on dynamics do not influence the static structure factor, $S(q)$. The results are supported by the XPCS experiment, microscope observation, and simulations. The described phenomenon remains valid for other soft-matter systems.

Comparison of simulated TTCs with experimental ones, as well as microscope observations, make it possible to estimate the shift of the sample due to the flow. For the dense BSA sample for the parameters under study, the range of this shift is from tens to hundreds of micrometers. However, microscope observations show that the real flow is more complicated than the simulations described since it is heterogeneous. Sample retraction occurs at different amplitudes and at slightly different times for different particles within the sample. Thus, the flow parameters estimated from the experimental TTC will be an average of the real values and will reflect the overall behavior of the material inside the sample. At the same time, measurements with a microscope also cannot be used for detailed quantitative assessment, as they show the behavior of only a 2D slice, while the behavior of the flow in the volume may differ (for example, near the walls). In addition, studies with opaque samples, which are of interest for this work, are not possible, and transparent analogs will give a similar qualitative picture, which, however, may differ quantitatively.

Finally, it was shown that the influence of the induced flow is not uniform within the sample. Measurements in the middle of the capillary demonstrate the presence of "wings" in the TTCs, while they are absent at the end of the

capillary. This observation is useful for the procedure of conducting XPCS experiments for soft-matter systems. Depending on the interest of the study, it is possible to investigate the native sample dynamics or the one induced by the flow. Furthermore, the "wing" feature can be used as a possible indicator of the presence of retraction, and if this effect is undesirable, the position of the exposure of the sample can be adjusted accordingly.

6.5 Appendix
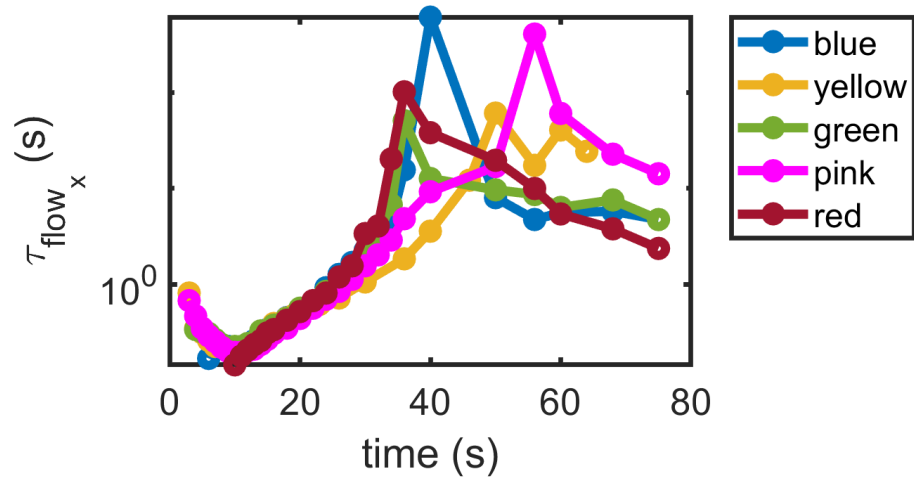
Figure 6.12: Relaxation time for $q = 0.8\mu m^{-1}$, estimated from Figure 6.11 (d) via $\tau_{flow_x} \propto 1/(q \times dshift_x/dt_{age})$ for distinct particles detected in the microscope images in Figure 6.11 (a) and labeled by contrasting colors. It can be seen that the peak in the relaxation time, which corresponds to the time of the retraction of the flow, has a different amplitude and appears at different moments for distinct particles.

Part III

Conclusions and outlook
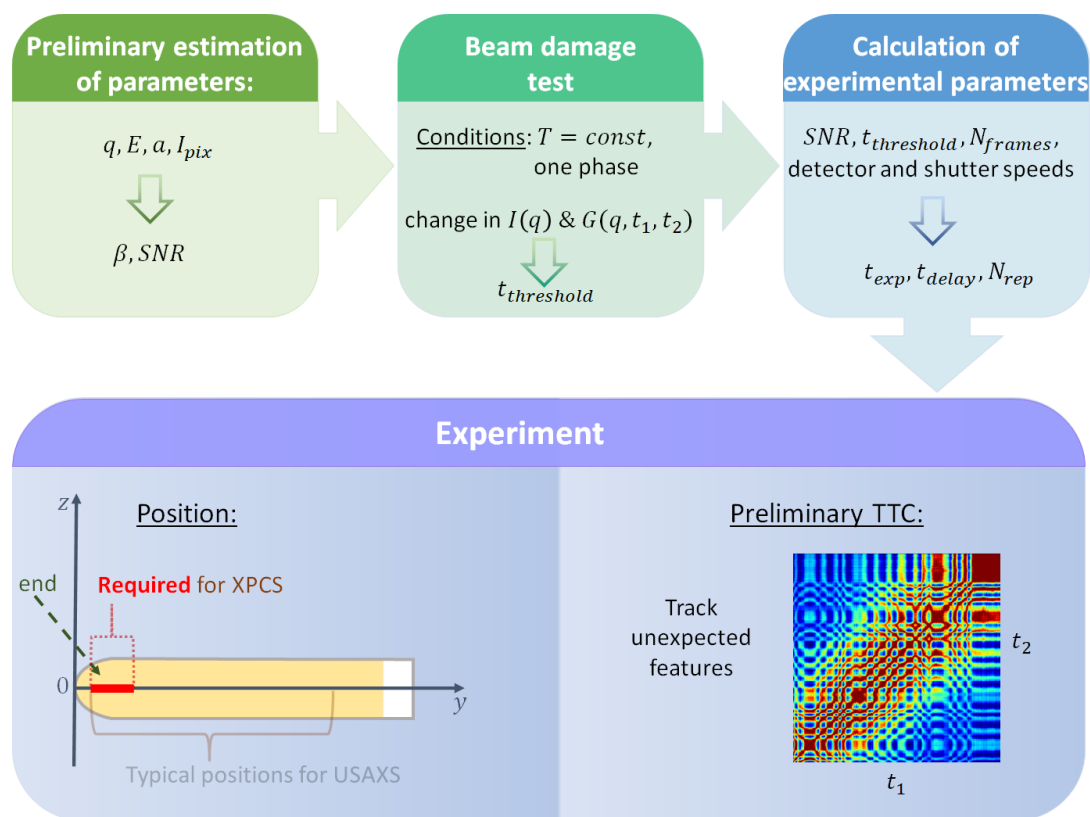
Chapter 7

Conclusions

The primary purpose of this dissertation is the study of the microscopic dynamics of LLPS in protein solutions probed by XPCS. This work is one of the first in the field due to the challenges of conducting XPCS experiments on proteins until recently and followed by the lack of a well-established procedure for such experiments. This chapter highlights the main results of the dissertation, which were individually presented in previous chapters.

The results of the dissertation can be divided into three groups. The first is developing a procedure for conducting experiments on proteins with coherent X-ray beams. The second, which is the predominant group of results, includes new approaches and methods for analyzing data obtained by XPCS, which are applicable to various soft-matter systems. The last group contains the results specific to the BSA-YCl$_3$ system under study, which made it possible to better understand its microscopic dynamics during phase separation.

7.1 Procedure of bio-XPCS experiments

Combining knowledge from the literature with some of the results of this work, one can arrive at the sequence of steps for conducting an XPCS experiment on proteins presented in Figure 7.1. The first step is to create a preliminary estimate of the parameters, as was shown in [63]. At this point, the q-range of interest, the energy, the parameters of the fast detector, the scattering of the sample, and the degree of coherence for these parameters must be taken into account. The second step is to conduct a beam damage test. This part still requires further study (see Chapter 8); however, some conclusions are already possible. The study of the effect of radiation should take place with the simultaneous measurement of kinetics and dynamics. The sample must be exposed continuously at a constant

Figure 7.1: Sequence of steps for conducting a bio-XPCS experiment based on a combination of results from [63], Section 3.2.2, Chapter 5 and Chapter 6.

temperature. Tracking induced changes in kinetics (or dynamics), the beam damage threshold can be estimated (which is a function of the incident flux). Third, taking into account the total experiment time of interest, speeds of the detector and shutter, the desired number of frames, the found beam damage threshold, and the contrast obtained with these parameters, the exposure and delay time are calculated, as well as the number of measurements necessary to obtain a sufficient signal-to-noise ratio (Section 3.2.2). The final stage involves the measurements themselves.

Let us suppose the experiment is performed on solutions in capillaries that may be accompanied by volume changes (e.g., phase transitions). In that case, special attention must be paid to which part of the capillary is being exposed. It is known that the shear stress modifies the spinodal decomposition and thus the kinetics of LLPS [302, 303]. However, this effect is absent at the center of the capillary cross-section, where the stress is zero. Additionally, in Chapter 6 it was shown that the dynamics of the sample in the middle and at the end

of the capillary are markedly different while having the same kinetics. Under the influence of flow, the measured dynamics can be accelerated. Moreover, in the case of flow retraction, often observed in the middle of the capillary, the two-time correlation maps change dramatically compared to the true sample dynamics and exhibit a "wing" feature. Thus, to minimize the effect of flow and measure the native behavior of the sample, the experiments should be carried out at the end and center of the capillary.

Finally, a quick calculation of TTCs must be carried out during measurements. The importance of TTC features has been discussed in Chapter 5 and Chapter 6. They contain information about the intrinsic dynamics of the sample and, in some cases, may also indicate the presence of induced dynamics as a result of an improperly conducted experiment. For example, they may reveal the presence of flow in the sample or vibrations of the sample holder.

The described procedure improves the knowledge of how to conduct XPCS experiments on biological samples. It helps to avoid the influence of many undesirable and unexpected factors and thus increases the probability of successfully measuring the intrinsic dynamics of the sample.

7.2 New approaches and methods for XPCS data analysis

Disentanglement of kinetics and dynamics contributions

Microscopic dynamics of complex fluids in the early stage of spinodal decomposition is strongly intertwined with the kinetics of structural evolution [40], which makes a quantitative characterization challenging. In this thesis, we demonstrated the approach to experimentally distinguish the kinetic and dynamic contributions (Chapter 4). It was suggested to compare the kinetic relaxation rate, calculated through the changes in the scattering intensity $I(q, t_{age})$ [270], with the dynamic relaxation rate obtained through the standard XPCS data analysis. The kinetics and dynamics can be disentangled if the counted rates have different orders. The approach was demonstrated on the example of the BSA-YCl$_3$ system undergoing LLPS. These experimental results were further supported by simulations based on the Cahn-Hilliard equation. The established framework is applicable to other condensed matter and biological
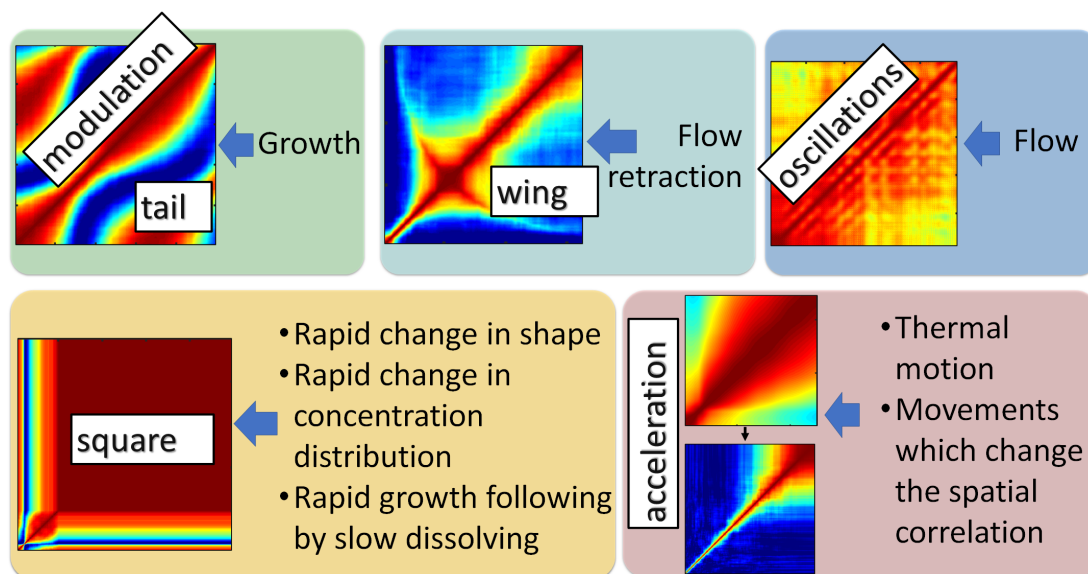
Figure 7.2: Dynamics and corresponding TTC features. Summary of Chapter 5 and Chapter 6.

systems undergoing phase transitions and may also inspire further theoretical work.

On the use of TTC features

Time-dependent dynamics of XPCS studies for non-equilibrium processes are frequently presented using two-time correlation functions (TTCs). These TTCs often contain more exciting features than the component along the diagonal and cannot be easily interpreted via classical analysis and simulation methods. In this thesis, a RE approach based on particle-based heuristic simulations was proposed to predict and understand the kinetics and dynamics of systems undergoing non-equilibrium processes (Chapter 5). As an example, the liquid-liquid phase separation in BSA-YCl$_3$ system was studied by USAXS-XPCS. We demonstrated that the rich features of experimental TTCs contain dynamic information and can be connected to the key control parameters. Thus, based on the combination of the Reverse-Engineering approach and modifications of the classical Cahn-Hilliard (CH) simulations presented in Chapter 5 and Chapter 6, we identified the following connections:

- **"Modulation" and "Tails"**. The "modulation", which is usually the main component for studying LLPS dynamics with XPCS, corresponds to the

growth of the domains, where the growth rate decreases with time (increasing the relaxation time). This feature depends on the evolution of the mean size and size distribution in the system. The "tail" feature raises from a correlation of the system between different distant times and has a substantial q-dependence, appearing earlier for higher q-values. This phenomenon may be caused by the shift of scattering intensity $I(q)$ due to a change in size and mean interparticle distance as a result of the correlation between different harmonics and appears once the characteristic length of the domains is a multiple of the investigation box size $(2\pi/q)$. Based on this result, it is possible to calculate the characteristic length of the experimental system from XPCS data even when the peak of the intensity profile moved out of the measurement window and a second-order of $I(q, t_{age})$ profile is not well-pronounced. This gives it an advantage over the well-established size determination methods from USAXS studies [46, 47]. Such a possibility to extract sizes from the XPCS experiments may open new prospects for the experiments on growing, coarsening or evolving systems.

- **"Square"**. It was found that rapid change of shape and concentration distribution and also a change from the rapid growth of domains at the early stage with subsequent slow dissolution result in the square-like feature of the TTC. All of these sub-phenomena are characteristic of the LLPS systems going from the density fluctuation stage to the coarsening stage of spinodal decomposition. However, the RE-modified CH simulations revealed that in real systems, the ratio of growth rate in the early stage to the speed of dissolution in the coarsening stage during Ostwald ripening has the most significant impact on the "square" feature. This ratio is strongly connected to the state of the system and its mobility. It was demonstrated that the closer a system is to the gel state, the more pronounced is the "square" feature in the simulations. Thus, it can be used to judge the gelation of a sample.

- **"Wing"**. It was shown that a flow retraction in liquid systems during XPCS measurements leads to the "wing" features in the TTCs. It contains information about different parameters of the flow. The shape of the "wing" depends on the flow rate ratio before and after the retraction. The curvature

of the "wing" results from the nonlinear evolution of these flow rates. It was also found that the state of the system at the time that the "wing" feature appears corresponds to a steady state with the least influence of flow and, thus, can be used to extract the native sample dynamics.

- **"Oscillations"**. The oscillations of the correlation function with time also relates to the flow. However, this feature can only be seen when the relaxation time of the flow is much less than the relaxation time of the system. The frequency of the oscillations corresponds to the rate of the flow. These conclusions are consistent with the literature where the "oscillations" were first established and investigated [61, 179, 281].

- **Acceleration of dynamics**. It was demonstrated that the thermal motion, as well as any other movements which change the spatial correlation of particles, may lead to the acceleration of the dynamics calculated via XPCS experiments. A necessary condition is that the relaxation time of this additional dynamics is comparable to or shorter than the relaxation time of the expected dynamics of the sample. In the case of an early stage of LLPS, this knowledge can be critical to interpreting the XPCS data. It has been shown that a possible reason for the difference between classical CH simulations and experiments is the presence of thermal motion, which accelerates the measured dynamics. The influence of the thermal motion decreases with the increase of the domain sizes and viscosity of the dense phase and finally becomes negligible in the coarsening stage.

These results are summarized in Figure 7.2. They demonstrate that the observed side features in the TTCs are not experimental artifacts but rather a rich source of dynamic information of the system. The Reverse-Engineering approach can go beyond CH theory and build the connection between these features in the TTC and the key parameters, such as relaxation time, concentration distribution, the size distribution of domains, viscosity, and mobility. The RE approach also showed the importance of taking into account thermal motion effects in the early stage of the LLPS. Finally, the framework established in this work can be employed for various systems and processes such as growth, coarsening, or evolving systems, and many other phenomena essential for understanding the fundamentals of materials synthesis, processing, and phase transformation. One of the primary benefits of this algorithm is the ability to go

beyond the existing theory if the experiment cannot be fully described by it or if there is no theoretical formalism for the investigated phenomenon.

On the use of different time coordinate systems

The classical analysis of TTCs requires the extraction of one-time correlations (g_2 function) at different sample ages. Two main coordinate systems are commonly used, leading to the use of horizontal or diagonal cuts [232]. It is agreed that diagonal cuts are more convenient for comparison to previous XPCS studies, while horizontal cuts give a better numerical convergence with other techniques (DLS). Nevertheless, the use of different time coordinate systems is still under debate. This thesis demonstrates cases when diagonal cuts are preferable over horizontal ones.

In Chapter 4, it was shown that using diagonal cuts under otherwise identical conditions allows one to calculate the relaxation time of the slow dynamics associated with the "square" feature, which is typical for phase separation [220, 223]. Its relaxation time was found to be similar to the kinetic one in both experiments and simulations. In addition, in Chapter 6 it was shown that slicing along a "wing" feature gives a possibility to estimate the relaxation time of the system with minimal flow influence. Since the shape of the "wing" depends on the ratio of the flow rates before and after the retraction, it turns out that different coordinate systems are beneficial in different conditions. For example, in the case of similar rates (as in Figure 6.4), diagonal cuts should be used.

7.3 Microscopic dynamics of LLPS of the BSA-YCl$_3$ system

The described approaches were applied to the BSA-YCl$_3$ system and made it possible to draw the following conclusions about its microscopic dynamics. In Chapter 4 it was shown that in the early stage of spinodal decomposition, the kinetics relaxation of BSA-YCl$_3$ system during LLPS is up to 40 times slower than the dynamics and thus can be decoupled. In the early stage, the microscopic dynamics is not Brownian dynamics of the proteins, which would have required relaxation time $\propto q^{-2}$ and shape parameter $\gamma \sim 1$. Instead, this dynamics can be well described using a hyper-diffusive ballistic motion, i.e., the relaxation

time $\propto q^{-1}$ and shape parameter $\gamma \sim 2$. Furthermore, the relaxation time of the dynamics exponentially increases with time in this early stage. In the late stage, where the domain coarsening is the primary process, the relaxation time increase with time following a power law. Similar two-stage behavior has been reported in XPCS investigations of Wigner glasses [193], glassy ferrofluids [268], and egg-white [222] and has been suggested as a general feature near the glass transition as well as gelation.

The interplay of the glass transition with LLPS is the subject of intense debate. For the BSA-YCl$_3$ system at high temperatures, a kinetically arrested phase transition was previously observed [46]. Therefore, the gelation of the sample was expected [46, 47, 304, 305] due to the glass transition. It is typically characterized by a dynamic arrest [97, 223, 269, 306] which was, however, not observed in the XPCS experiments presented in this thesis. Thus, additional evidence for gelation in the sample was required. In Chapter 5 with the use of the RE approach, it was shown that the degree of visibility of a "square" feature is related to gelation. Since the "square" feature is much brighter on the experimental TTCs than in the case of classical CH simulations and taking into account previous experimental confirmations, it can be concluded that there is gelation of the BSA-YCl$_3$ system at the investigated time scales identifying a nearby glass transition.

All in all, a comprehensive understanding of the procedure and data analysis of XPCS experiments on the protein systems, as well as microscopic dynamics and its interplay with the kinetics of LLPS, is developed in this dissertation. The following chapter discusses possible directions for further work on the topic and open questions.

Chapter 8

Outlook

There are still open questions that need to be addressed. They are summarized in this chapter together with possible further directions of work to answer them.

One of the central issues in conducting XPCS studies on biological samples is how to characterize the radiation damage and reduce it. According to the approach described in this thesis, a beam damage threshold is registered by the occurrence of changes in kinetics or dynamics. The questions remain, how precise this method is, and whether the result is q-dependent. If so, when does the beam damage on the single-protein scale start to affect the microscopic dynamics of the domains? To answer these questions, the q-dependency of the beam damage threshold should be investigated by the suggested method, followed by XPCS beam damage studies at different length scales. In addition, questions arise about the source of such changes in the scattering pattern. Are these changes the result of the denaturation or do we observe some other beam effects on the sample? For example, it is likely that for systems in which the process of liquid-liquid separation depends on charges (like BSA-YCl$_3$), ionization resulting from exposure can start beam-induced LLPS. Consequently, the radiation dose will be yet another parameter of the phase diagram, along with the protein and salt concentrations, temperature, and pressure. To study the effect of the beam on the process of LLPS, further measurements are required at different temperatures (above and below the critical one) and different sample concentrations, including the study of the critical dose for a pure BSA solution. So, it may be worthwhile to compare the effects with other LLPS systems, where the phase separation process depends little or not at all on the charges inside the system. As an example, a comparison can be made with an IgG-PEG system [47, 223], where the liquid separation process is based on the depletion effect. Finally, the reduction of the beam influence can be performed by adding small

molecules such as dithiothreitol (DTT) [60, 307] to the BSA-YCl$_3$ sample. However, this procedure will change the phase diagram and, thus, the dynamics under otherwise identical conditions. Also, since cryogenic cooling is not applicable for LLPS systems, it is necessary to look for other methods to reduce the influence of the beam.

The dissertation discussed the gelation of the system and its impact on microscopic dynamics. Is the intra-domain dynamics (faster dynamics) sensitive to the gel/glass formation, and what is the long-time single-molecule diffusion? To answer these questions, the work needs to be extended to different length and time scales using XPCS in SAXS mode and the fast development of X-ray free-electron laser (XFEL) facilities, so the dynamic behavior ranging from single protein to the domain coarsening could be covered.

In the thesis, it was shown that gelation does not lead to microscopic dynamic arrest of BSA-YCl$_3$. However, such an arrest was observed for the IgG-PEG system in [223]. Is this difference a consequence of phase behavior of low (LCST) and upper critical solution temperature phase behaviors (UCST) for BSA-YCl$_3$ and IgG-PEG, respectively? Another possible reason is a different interplay between the glass line and the binodal [45] or other explanations not previously considered. Perhaps the study of the microscopic dynamics of other LCST and UCST systems, with a known position of the glass line, will answer these questions.

Finally, several improvements related to simulations should be made. The simulations discussed in this thesis were performed in 2D, which is sufficient for a qualitative analysis. However, it is necessary to carry out both Cahn-Hilliard (CH) and Reverse-Engineering (RE) simulations in 3D for a quantitative description. In addition, it would be useful to track information about the evolution of each domain in the CH using various methods from image detection. Thus, RE can be applied not only to the entire CH real space but also to individual domains, which expands the possibilities of this method.

List of own publications

1. **Tracking equilibrium protein dynamics in solution using MHz X-ray photon correlation spectroscopy**

   M. Reiser, A. Girelli, A. Ragulskaya, S. Das, S. Berkowicz, M. Bin, M. Ladd Parada, H. Poggemann, M. S. Akhundzadeh, A. Al-Masoodi, S. Timmermann, L. Randolph, Y. Chushkin, T. Seydel, U. Bösenberg, J. Hallmann, A. Madsen, J. Möller, A. Rodeiguez-Fernandez, R. Rosca, R. Schaffer, M. Scholz, R. Shayduk, A. Zozulya, F. Schreiber, F. Zhang, F. Perakis and C. Gutt.

   Nature Communications, in print, 2022.

2. **Reverse-engineering method for XPCS studies of non-equilibrium dynamics**

   A. Ragulskaya, V. Starostin, N. Begam, A. Girelli, H. Rahmann, M. Reiser, F. Westermeier, M. Sprung, F. Zhang, C. Gutt and F. Schreiber.

   IUCrJ 9, 439-448, 2022.

3. **Automated matching of two-time X-ray photon correlation maps from protein dynamics with Cahn-Hilliard type simulations using autoencoder networks**

   S. Timmermann, V. Starostin, A. Girelli, A. Ragulskaya, H. Rahmann, M. Reiser, N. Begam, L. Randolph, M. Sprung, S. Chandran, F. Zhang, F. Schreiber, C. Gutt.

   Journal of Applied Crystallography, 55, 2022.

4. **Interplay between Kinetics and Dynamics of Liquid-Liquid Phase Separation in a Protein Solution Revealed by Coherent X-ray Spectroscopy**

   A. Ragulskaya, N. Begam, A. Girelli, H. Rahmann, M. Reiser, F. Westermeier, M. Sprung, F. Zhang, C. Gutt and F. Schreiber.

   Journal of Physical Chemistry Letters 12 (30), 7085-7090, 2021.

5. **Microscopic dynamics underlying the arrested phase separation of a protein solution revealed by XPCS**

   A. Girelli, H. Rahmann, N. Begam, A. Ragulskaya, M. Reiser, S. Chandran, F. Westermeier, M. Sprung, F. Zhang, C. Gutt, F. Schreiber.

   Physical Review Letters 126, 138004, 2021.

6. **Kinetics of network formation and heterogeneous dynamics of an egg-white gel revealed by coherent X-ray scattering**

   N. Begam, A. Ragulskaya, A. Girelli, H. Rahmann, S. Chandran, F. Westermeier, M. Sprung, M. Reiser, F. Zhang, C. Gutt and F. Schreiber.

   Physical Review Letters 126, 098001, 2021.

7. **Interplay Between Glass Formation and Liquid-Liquid Phase Separation Revealed by the Scattering Invariant**

   S. Da Vela, N. Begam, D. Dyachok, R. Santiago Schäufele, O. Matsarskaia, M. Braun, A. Girelli, A. Ragulskaya, A. Mariani, F. Zhang, and F. Schreiber.

   Journal of Physical Chemistry Letters 11, 7273-7278, 2020.

8. **The investigation of [Fe/Cr] multilayer by GISAXS**

   A.V. Ragulskaya, M.A. Andreeva, A.V. Rogachev, S.N. Yakunin.

   Superlattices and Microstructures 125, 16-25, 2019.

9. **Supercontinuum generation under filamentation driven by intense femtosecond pulses in supercritical xenon and carbon dioxide**

   V.N. Bagratashvili, V.M. Gordienko, E.I. Mareev, N.V. Minaev, A.V. Ragulskaya, F.V. Potemkin.

   Russian Journal of Physical Chemistry B, Maik Nauka/Interperiodica Publishing (Russian Federation), 10, 8, 1211-1215, 2016.

Acknowledgements

Abbreviations

BS	Binder-Stauffer (mechanism)
BSA	Bovine Serum Albumin
CH	Cahn-Hilliard
DESY	Deutsches Elektronen-Synchrotron
DLS	Dynamic Light Scattering
DLVO	Derjaguin–Landau–Verwey– Overbeck (theory)
ESRF	European Synchrotron Radiation Facility
IgG-PEG	Immunoglobulin G - Polyethylene Glycol system
INS	Inelastic Neutron Scattering
IXS	Inelastic X-ray Scattering
KWW	Kohlrausch-Williams-Watts
LCST/UCST	Lower/Upper Critical Solution Temperature Phase Behaviour
LLPS	Liquid-Liquid Phase Separation
LSW	Liftshitz-Slyozv-Wagner (mechanism)
MLOs	Membraneless Organelles
RE	Reverse-Engineering
SD	Spinodal Decomposition
SNR	Signal-to-noise Ratio

TTC	Two-time Correlation (map)
USAXS/SAXS/WAXS	Ultra-Small/Small/Wide Angle X-ray Scattering
XFEL	X-Ray Free-Electron Laser
XPCS	X-ray Photon Correlation Spectroscopy

Bibliography

[1] S. F. Banani, H. O. Lee, A. A. Hyman, and M. K. Rosen, *Biomolecular condensates: organizers of cellular biochemistry*, Nature Reviews Molecular Cell Biology **18** (2017), 285.

[2] A. A. Hyman, C. A. Weber, and F. Jülicher, *Liquid-liquid phase separation in biology*, Annual Review of Cell and Developmental Biology **30** (2014), 39.

[3] J. R. Friedman and J. Nunnari, *Mitochondrial form and function*, Nature **505** (2014), 335.

[4] J. P. Luzio, P. R. Pryor, and N. A. Bright, *Lysosomes: fusion and function*, Nature Reviews Molecular Cell Biology **8** (2007), 622.

[5] F.-M. Boisvert, S. van Koningsbruggen, J. Navascués, and A. I. Lamond, *The multifunctional nucleolus*, Nature Reviews Molecular Cell Biology **8** (2007), 574.

[6] R. Mahen and A. R. Venkitaraman, *Pattern formation in centrosome assembly*, Current Opinion in Cell Biology **24** (2012), 14.

[7] C. J. Decker and R. Parker, *P-bodies and stress granules: Possible roles in the control of translation and mRNA degradation*, Cold Spring Harbor Perspectives in Biology **4** (2012), a012286.

[8] J. R. Buchan and R. Parker, *Eukaryotic stress granules: The ins and outs of translation*, Molecular Cell **36** (2009), 932.

[9] J. Weidner, C. Wang, C. Prescianotto-Baschong, A. F. Estrada, and A. Spang, *The polysome-associated proteins Scp160 and Bfr1 prevent P body formation under normal growth conditions*, Journal of Cell Science **127** (2014), 1992.

[10] N. N. Noda, Z. Wang, and H. Zhang, *Liquid–liquid phase separation in autophagy*, Journal of Cell Biology **219** (2020), e202004062.

[11] C. P. Brangwynne, C. R. Eckmann, D. S. Courson, A. Rybarska, C. Hoege, J. Gharakhani, F. Jülicher, and A. A. Hyman, *Germline P granules are liquid droplets that localize by controlled dissolution/condensation*, Science **324** (2009), 1729.

[12] Y. Shin and C. P. Brangwynne, *Liquid phase condensation in cell physiology and disease*, Science **357** (2017), eaaf4382.

[13] L.-P. Bergeron-Sandoval, N. Safaee, and S. W. Michnick, *Mechanisms and consequences of macromolecular phase separation*, Cell **165** (2016), 1067.

[14] W. T. Snead and A. S. Gladfelter, *The control centers of biomolecular phase separation: How membrane surfaces, PTMs, and active processes regulate condensation*, Molecular Cell **76** (2019), 295.

[15] S. Boeynaems, S. Alberti, N. L. Fawzi, T. Mittag, M. Polymenidou, F. Rousseau, J. Schymkowitz, J. Shorter, B. Wolozin, L. V. D. Bosch, P. Tompa, and M. Fuxreiter, *Protein phase separation: A new phase in cell biology*, Trends in Cell Biology **28** (2018), 420.

[16] S. Brocca, R. Grandori, S. Longhi, and V. Uversky, *Liquid–liquid phase separation by intrinsically disordered protein regions of viruses: Roles in viral life cycle and control of virus–host interactions*, International Journal of Molecular Sciences **21** (2020), 9045.

[17] V. N. Uversky, *Protein intrinsic disorder-based liquid–liquid phase transitions in biological systems: Complex coacervates and membrane-less organelles*, Advances in Colloid and Interface Science **239** (2017), 97.

[18] A. S. Holehouse and R. V. Pappu, *Functional implications of intracellular phase transitions*, Biochemistry **57** (2018), 2415.

[19] H. Zhang, X. Ji, P. Li, C. Liu, J. Lou, Z. Wang, W. Wen, Y. Xiao, M. Zhang, and X. Zhu, *Liquid-liquid phase separation in biology: mechanisms, physiological functions and human diseases*, Science China Life Sciences **63** (2020), 953.

[20] D. Kaganovich, *There is an inclusion for that: Material properties of protein granules provide a platform for building diverse cellular functions*, Trends in Biochemical Sciences **42** (2017), 765.

[21] S. Alberti and S. Carra, *Quality control of membraneless organelles*, Journal of Molecular Biology **430** (2018), 4711.

[22] S. Alberti and D. Dormann, *Liquid–liquid phase separation in disease*, Annual Review of Genetics **53** (2019), 171.

[23] G. B. Benedek, *Cataract as a protein condensation disease: The proctor lecture*, American Journal of Ophthalmology **125** (1998), 279.

[24] W. A. Eaton and J. Hofrichter, *Sickle cell hemoglobin polymerization*, Advances in Protein Chemistry **40** (1990), 63.

[25] I. A. Klein, A. Boija, L. K. Afeyan, S. W. Hawken, M. Fan, A. Dall'Agnese, O. Oksuz, J. E. Henninger, K. Shrinivas, B. R. Sabari, I. Sagi, V. E. Clark, J. M. Platt, M. Kar, P. M. McCall, A. V. Zamudio, J. C. Manteiga, E. L. Coffey, C. H. Li, N. M. Hannett, Y. E. Guo, T.-M. Decker, T. I. Lee, T. Zhang, J.-K. Weng, D. J. Taatjes, A. Chakraborty, P. A. Sharp, Y. T. Chang, A. A. Hyman, N. S. Gray, and R. A. Young, *Partitioning of cancer therapeutics in nuclear condensates*, Science **368** (2020), 1386.

[26] A. Aguzzi and M. Altmeyer, *Phase separation: Linking cellular compartmentalization to disease*, Trends in Cell Biology **26** (2016), 547.

[27] P. Brundin, R. Melki, and R. Kopito, *Prion-like transmission of protein aggregates in neurodegenerative diseases*, Nature Reviews Molecular Cell Biology **11** (2010), 301.

[28] J. M. Shulman, P. L. D. Jager, and M. B. Feany, *Parkinson's disease: Genetics and pathogenesis*, Annual Review of Pathology: Mechanisms of Disease **6** (2011), 193.

[29] W. Robberecht and T. Philips, *The changing scene of amyotrophic lateral sclerosis*, Nature Reviews Neuroscience **14** (2013), 248.

[30] L. K. Davis, I. J. Ford, and B. W. Hoogenboom, *Crowding-induced phase separation of nuclear transport receptors in FG nucleoporin assemblies*, eLife **11** (2022), e72627.

[31] T. Yoshizawa, R.-S. Nozawa, T. Z. Jia, T. Saio, and E. Mori, *Biological phase separation: cell biology meets biophysics*, Biophysical Reviews **12** (2020), 519.

[32] A. Lazcano, *Historical development of origins research*, Cold Spring Harbor Perspectives in Biology **2** (2010), a002089.

[33] T. Hyman and C. Brangwynne, *In retrospect: The origin of life*, Nature **491** (2012), 524.

[34] K. K. Turoverov, I. M. Kuznetsova, A. V. Fonin, A. L. Darling, B. Y. Zaslavsky, and V. N. Uversky, *Stochasticity of biological soft matter: Emerging concepts in intrinsically disordered proteins and biological phase separation*, Trends in Biochemical Sciences **44** (2019), 716.

[35] B. Y. Zaslavsky and V. N. Uversky, *In aqua veritas: The indispensable yet mostly ignored role of water in phase separation and membrane-less organelles*, Biochemistry **57** (2018), 2437.

[36] D. M. Mitrea and R. W. Kriwacki, *Phase separation in biology functional organization of a higher order*, Cell Communication and Signaling **14** (2016), 1.

[37] A. L. Darling, B. Y. Zaslavsky, and V. N. Uversky, *Intrinsic disorder-based emergence in cellular biology: Physiological and pathological liquid-liquid phase transitions in cells*, Polymers **11** (2019), 990.

[38] A. S. Raut and D. S. Kalonia, *Pharmaceutical perspective on opalescence and liquid–liquid phase separation in protein solutions*, Molecular Pharmaceutics **13** (2016), 1431.

[39] T. Gibaud, N. Mahmoudi, J. Oberdisse, P. Lindner, J. S. Pedersen, C. L. P. Oliveira, A. Stradner, and P. Schurtenberger, *New routes to food gels and glasses*, Faraday Discussions **158** (2012), 267.

[40] J. Gunton, A. Shiryayev, and D. Pagan, *Protein condensation: Kinetic pathways to crystallization and disease*, Cambridge University Press, 2007.

[41] S. D. Durbin and G. Feher, *Protein crystallization*, Annual Review of Physical Chemistry **47** (1996), 171.

[42] F. Zhang, F. Roosen-Runge, A. Sauter, M. Wolf, R. M. J. Jacobs, and F. Schreiber, *Reentrant condensation, liquid-liquid phase separation and crystallization in protein solutions induced by multivalent metal ions*, Pure and Applied Chemistry **86** (2014), 191.

[43] F. Zhang, M. W. A. Skoda, R. M. J. Jacobs, S. Zorn, R. A. Martin, C. M. Martin, G. F. Clark, S. Weggler, A. Hildebrandt, O. Kohlbacher, and F. Schreiber, *Reentrant condensation of proteins in solution induced by multivalent counterions*, Physical Review Letters **101** (2008), 148101.

[44] O. Matsarskaia, M. K. Braun, F. Roosen-Runge, M. Wolf, F. Zhang, R. Roth, and F. Schreiber, *Cation-induced hydration effects cause lower critical solution temperature behavior in protein solutions*, The Journal of Physical Chemistry B **120** (2016), 7731.

[45] S. Da Vela, N. Begam, D. Dyachok, R. S. Schäufele, O. Matsarskaia, M. K. Braun, A. Girelli, A. Ragulskaya, A. Mariani, F. Zhang, and F. Schreiber, *Interplay between glass formation and liquid-liquid phase separation revealed by the scattering invariant*, The Journal of Physical Chemistry Letters **11** (2020), 7273.

[46] S. Da Vela, M. K. Braun, A. Dörr, A. Greco, J. Möller, Z. Fu, F. Zhang, and F. Schreiber, *Kinetics of liquid-liquid phase separation in protein solutions exhibiting LCST phase behavior studied by time-resolved USAXS and VSANS*, Soft Matter **12** (2016), 9334.

[47] S. Da Vela, C. Exner, R. S. Schäufele, J. Möller, Z. Fu, F. Zhang, and F. Schreiber, *Arrested and temporarily arrested states in a protein-polymer mixture studied by USAXS and VSANS*, Soft Matter **13** (2017), 8756.

[48] J. V. Lindt, A. Bratek-Skicki, P. N. Nguyen, D. Pakravan, L. F. Durán-Armenta, A. Tantos, R. Pancsa, L. V. D. Bosch, D. Maes, and P. Tompa, *A generic approach to study the kinetics of liquid–liquid phase separation under near-native conditions*, Communications Biology **4** (2021), 77.

[49] O. Matsarskaia, S. D. Vela, A. Mariani, Z. Fu, F. Zhang, and F. Schreiber, *Phase-separation kinetics in protein–salt mixtures with compositionally tuned interactions*, The Journal of Physical Chemistry B **123** (2019), 1913.

[50] T. Gibaud and P. Schurtenberger, *A closer look at arrested spinodal decomposition in protein solutions*, Journal of Physics: Condensed Matter **21** (2009), 322201.

[51] H. Cai, B. Gabryelczyk, M. S. S. Manimekalai, G. Grüber, S. Salentinig, and A. Miserez, *Self-coacervation of modular squid beak proteins – a comparative study*, Soft Matter **13** (2017), 7740.

[52] A. Banc, J. Pincemaille, S. Costanzo, E. Chauveau, M.-S. Appavou, M.-H. Morel, P. Menut, and L. Ramos, *Phase separation dynamics of gluten protein mixtures*, Soft Matter **15** (2019), 6160.

[53] C. Beck, M. Grimaldo, F. Roosen-Runge, R. Maier, O. Matsarskaia, M. Braun, B. Sohmen, O. Czakkel, R. Schweins, F. Zhang, T. Seydel, and F. Schreiber, *Following protein dynamics in real time during crystallization*, Crystal Growth & Design **19** (2019), 7036.

[54] O. G. Shpyrko, *X-ray photon correlation spectroscopy*, Journal of Synchrotron Radiation **21** (2014), 1057.

[55] D. O. Riese, W. L. Vos, G. H. Wegdam, F. J. Poelwijk, D. L. Abernathy, and G. Grübel, *Photon correlation spectroscopy: X-rays versus visible light*, Physical Review E **61** (2000), 1676.

[56] L. B. Lurio, D. Lumma, A. R. Sandy, M. A. Borthwick, P. Falus, S. G. J. Mochrie, J. F. Pelletier, M. Sutton, L. Regan, A. Malik, and G. B. Stephenson, *Absence of scaling for the intermediate scattering function of a hard-sphere suspension: Static and dynamic X-ray scattering from concentrated polystyrene latex spheres*, Physical Review Letters **84** (2000), 785.

[57] T. Seydel, A. Madsen, M. Tolan, G. Grübel, and W. Press, *Capillary waves in slow motion*, Physical Review B **63** (2001), 073409.

[58] D. Lumma, M. A. Borthwick, P. Falus, L. B. Lurio, and S. G. J. Mochrie, *Equilibrium dynamics in the nondiffusive regime of an entangled polymer blend*, Physical Review Letters **86** (2001), 2042.

[59] R. Bandyopadhyay, D. Liang, H. Yardimci, D. A. Sessoms, M. A. Borthwick, S. G. J. Mochrie, J. L. Harden, and R. L. Leheny, *Evolution of particle-scale dynamics in an aging clay suspension*, Physical Review Letters **93** (2004), 228302.

[60] C. M. Jeffries, M. A. Graewert, D. I. Svergun, and C. E. Blanchet, *Limiting radiation damage for high-brilliance biological solution scattering: practical*

experience at the EMBL p12 beamline PETRAIII, Journal of Synchrotron Radiation **22** (2015), 273.

[61] A. Fluerasu, A. Moussaïd, P. Falus, H. Gleyzolle, and A. Madsen, *X-ray photon correlation spectroscopy under flow*, Journal of Synchrotron Radiation **15** (2008), 378.

[62] B. Ruta, F. Zontone, Y. Chushkin, G. Baldi, G. Pintori, G. Monaco, B. Rufflé, and W. Kob, *Hard X-rays as pump and probe of atomic motion in oxide glasses*, Scientific Reports **7** (2017), 3962.

[63] J. Möller, M. Sprung, A. Madsen, and C. Gutt, *X-ray photon correlation spectroscopy of protein dynamics at nearly diffraction-limited storage rings*, IUCrJ **6** (2019), 794.

[64] P. Vodnala, N. Karunaratne, S. Bera, L. Lurio, G. M. Thurston, N. Karonis, J. Winans, A. Sandy, S. Narayanan, L. Yasui, E. Gaillard, and K. Karumanchi, *Radiation damage limits to XPCS studies of protein dynamics*, AIP Conference Proceedings **1741** (2016), 050026.

[65] E. Verwey and J. Overbeek, *Theory of the Stability of Lyophobic Colloids*, Elsevier, Amsterdam, 1948.

[66] B. Ninham, *On progress in forces since the DLVO theory*, Advances in Colloid and Interface Science **83** (1999), 1.

[67] D. Horinek, *DLVO theory*, Springer New York, 2014.

[68] J. D. van der Waals, *Over de continuiteit van den gas- en vloeistoftoestand*, PhD thesis, Hoogeschool Te Leiden, 1873.

[69] B. Smit, *Phase diagrams of Lennard-Jones fluids*, The Journal of Chemical Physics **96** (1992), 8639.

[70] R. Piazza, *Statistical physics: A prelude and fugue for engineers*, Springer Berlin Heidelberg, 2016.

[71] V. J. Anderson and H. N. W. Lekkerkerker, *Insights into phase transition kinetics from colloid science*, Nature **416** (2002), 811.

[72] P. N. Pusey and W. van Megen, *Phase behaviour of concentrated suspensions of nearly hard colloidal spheres*, Nature **320** (1986), 340.

[73] R. A. Curtis, J. M. Prausnitz, and H. W. Blanch, *Protein–protein and protein–salt interactions in aqueous protein solutions containing concentrated electrolytes*, Biotechnology and Bioengineering **57** (1998), 11.

[74] K. Julius, J. Weine, M. Gao, J. Latarius, M. Elbers, M. Paulus, M. Tolan, and R. Winter, *Impact of macromolecular crowding and compression on protein–protein interactions and liquid–liquid phase separation phenomena*, Macromolecules **52** (2019), 1772.

[75] O. Matsarskaia, F. Roosen-Runge, and F. Schreiber, *Multivalent ions and biomolecules: Attempting a comprehensive perspective*, ChemPhysChem **21** (2020), 1742.

[76] J. C. Crocker and D. G. Grier, *When like charges attract: The effects of geometrical confinement on long-range colloidal interactions*, Physical Review Letters **77** (1996), 1897.

[77] J. G. Ibarra-Armenta, A. Martín-Molina, and M. Quesada-Pérez, *Influence of monovalent ion size on colloidal forces probed by Monte Carlo simulations*, Physical Chemistry Chemical Physics **13** (2011), 13349.

[78] P. Papon, S. Schnur, J. Leblond, and P. Meijer, *The physics of phase transitions: Concepts and applications*, Advanced Texts in Physics, Springer Berlin Heidelberg, 2006.

[79] S. Z. D. Cheng, *Phase transitions in polymers: the role of metastable states*, 1st ed., Elsevier North-Holland, 2008.

[80] J. D. van der Waals, *The equation of state for gases and liquids*, Nobel Lectures, Physics (1910).

[81] H. Davis, *Statistical mechanics of phases, interfaces, and thin films*, Advances in interfacial engineering series, VCH New York, 1996.

[82] M. Baus and C. F. Tejero (eds.), *Equilibrium statistical physics*, Springer Berlin Heidelberg, 2008.

[83] B. Linder, *Thermodynamics and introductory statistical mechanics*, Wiley Inter-Science online books, Wiley New Jersey, 2004.

[84] R. A. L. Jones, *Soft condensed matter*, Oxford University Press, 2002.

[85] C. Liu, A. Lomakin, G. M. Thurston, D. Hayden, A. Pande, J. Pande, O. Ogun, N. Asherie, and G. B. Benedek, *Phase separation in multicomponent aqueous-protein solutions*, The Journal of Physical Chemistry **99** (1995), 454.

[86] J. Lee and S. Timasheff, *Partial specific volumes and interactions with solvent components of proteins in guanidine hydrochloride*, Biochemistry **13** (1974), 257.

[87] J. L. Anderson, *Colloid transport by interfacial forces*, Annual Review of Fluid Mechanics **21** (1989), 61.

[88] M. Sleutel, *Growth kinetics and mass transport phenomena during protein crystallization*, PhD thesis, Vrije Universiteit Brussel (Belgium), 2008.

[89] J. Berry, C. P. Brangwynne, and M. Haataja, *Physical principles of intracellular organization via active and passive phase transitions*, Reports on Progress in Physics **81** (2018), 046601.

[90] T. H. Zhang and Y. Liu, *Experimental modelling of single-particle dynamic processes in crystallization by controlled colloidal assembly*, Chemical Society Reviews **43** (2014), 2324.

[91] J. B. Rowe, R. A. Cancel, T. D. Evangelous, R. P. Flynn, S. Pechenov, J. A. Subramony, J. Zhang, and Y. Wang, *Metastability gap in the phase diagram of monoclonal IgG antibody*, Biophysical Journal **113** (2017), 1750.

[92] G. Foffi, G. D. McCullagh, A. Lawlor, E. Zaccarelli, K. A. Dawson, F. Sciortino, P. Tartaglia, D. Pini, and G. Stell, *Phase equilibria and glass transition in colloidal systems with short-ranged attractive interactions: Application to protein crystallization*, Physical Review E **65** (2002), 031407.

[93] M. Shah, O. Galkin, and P. G. Vekilov, *Smooth transition from metastability to instability in phase separating protein solutions*, The Journal of Chemical Physics **121** (2004), 7505.

[94] K. Binder, *Double-well thermodynamic potentials and spinodal curves: how real are they?*, Philosophical Magazine Letters **87** (2007), 799.

[95] F. Cardinaux, T. Gibaud, A. Stradner, and P. Schurtenberger, *Interplay between spinodal decomposition and glass formation in proteins exhibiting short-range attractions*, Physical Review Letters **99** (2007), 118301.

[96] S. Bucciarelli, L. Casal-Dujat, C. De Michele, F. Sciortino, J. Dhont, J. Bergenholtz, B. Farago, P. Schurtenberger, and A. Stradner, *Unusual dynamics of concentration fluctuations in solutions of weakly attractive globular proteins*, The Journal of Physical Chemistry Letters **6** (2015), 4470.

[97] X. Lu, S. G. J. Mochrie, S. Narayanan, A. R. Sandy, and M. Sprung, *How a liquid becomes a glass both on cooling and on heating*, Physical Review Letters **100** (2008), 045701.

[98] J. W. Cahn and J. E. Hilliard, *Free energy of a nonuniform system. I. Interfacial free energy*, The Journal of Chemical Physics **28** (1958), 258.

[99] J. W. Cahn and J. E. Hilliard, *Free energy of a nonuniform system. III. Nucleation in a two-component incompressible fluid*, The Journal of Chemical Physics **31** (1959), 688.

[100] J. W. Cahn, *Phase separation by spinodal decomposition in isotropic systems*, The Journal of Chemical Physics **42** (1965), 93.

[101] B. F. Barton, P. D. Graham, and A. J. McHugh, *Dynamics of spinodal decomposition in polymer solutions near a glass transition*, Macromolecules **31** (1998), 1672.

[102] D. Sappelt and J. Jäckle, *Spinodal decomposition with formation of a glassy phase*, EPL (Europhysics Letters) **37** (1997), 13.

[103] J. D. Gunton, *The dynamics of random interfaces in phase transitions*, Journal of Statistical Physics **34** (1984), 1019.

[104] F. Sciortino, R. Bansil, H. E. Stanley, and P. Alstrøm, *Interference of phase separation and gelation: A zeroth-order kinetic model*, Physical Review E **47** (1993), 4615.

[105] J. Gunton, M. San Miguel, and P. Sahni, *The dynamics of first order phase transitions*, Phase Transitions and Critical Phenomena, Academic Press, London, 1983.

[106] I. Lifshitz and V. Slyozov, *The kinetics of precipitation from supersaturated solid solutions*, Journal of Physics and Chemistry of Solids **19** (1961), 35.

[107] C. Wagner, *Theorie der alterung von niederschlägen durch umlösen (ostwald-reifung)*, Zeitschrift für Elektrochemie, Berichte der Bunsengesellschaft für physikalische Chemie **65** (1961), 581.

[108] K. Binder and D. Stauffer, *Theory for the slowing down of the relaxation and spinodal decomposition of binary mixtures*, Physical Review Letters **33** (1974), 1006.

[109] E. D. Siggia, *Late stages of spinodal decomposition in binary mixtures*, Physical review A **20** (1979), 595.

[110] W. Ostwald, *Studien über die Bildung und Umwandlung fester Körper*, Zeitschrift für physikalische Chemie **22** (1897), 289.

[111] P. W. Voorhees, *Ostwald ripening of two-phase mixtures*, Annual Review of Materials Science **22** (1992), 197.

[112] S. K. Das, S. Roy, and J. Midya, *Coarsening in fluid phase transitions*, Comptes Rendus Physique **16** (2015), 303.

[113] D. Marsal, *Finite differenzen und elemente*, Springer Berlin Heidelberg, 1989.

[114] D. F. Griffiths and D. J. Higham, *Numerical methods for ordinary differential equations*, Springer London, 2010.

[115] K. Hawick and D. Playne, *Modelling, simulating and visualising the cahn-hilliard-cook field equation*, International Journal of Computer Aided Engineering and Technology **2** (2010), 78–93.

[116] G. Brown and A. Chakrabarti, *Monte Carlo study of phase separation in critical polymer blends*, Physical Review E **48** (1993), 3705.

[117] J. He, H. Zhang, and Y. Yang, *Monte Carlo simulation of chain length distribution in radical polymerization with transfer reaction*, Macromolecular Theory and Simulations **4** (1995), 811.

[118] N. Vasishtha and E. Nauman, *Hydrodynamic effects in the phase separation of binary polymer mixtures*, Chemical Engineering Communications **129** (1994), 29.

[119] S. Tremaine, *On the origin of irregular structure in saturn's rings*, The Astronomical Journal **125** (2003), 894.

[120] V. Cristini, X. Li, J. S. Lowengrub, and S. M. Wise, *Nonlinear simulations of solid tumor growth using a mixture model: invasion and branching*, Journal of Mathematical Biology **58** (2008), 723.

[121] M. Herz and P. Knabner, *Modeling and simulation of coagulation according to dlvo-theory in a continuum model for electrolyte solutions*, arXiv (2016).

[122] R. Curtis and L. Lue, *A molecular approach to bioseparations: protein-protein and protein-salt interactions*, Chemical Engineering Science **61** (2006), 907.

[123] P. M. Tessier, S. D. Vandrey, B. W. Berger, R. Pazhianur, S. I. Sandler, and A. M. Lenhoff, *Self-interaction chromatography: a novel screening method for rational protein crystallization*, Acta Crystallographica Section D **58** (2002), 1531.

[124] V. L. Vilker, C. K. Colton, and K. A. Smith, *The osmotic pressure of concentrated protein solutions: Effect of concentration and pH in saline solutions of bovine serum albumin*, Journal of Colloid and Interface Science **79** (1981), 548.

[125] R. Das, T. T. Mills, L. W. Kwok, G. S. Maskel, I. S. Millett, S. Doniach, K. D. Finkelstein, D. Herschlag, and L. Pollack, *Counterion distribution around DNA probed by solution X-ray scattering*, Physical Review Letters **90** (2003), 188103.

[126] R. Glaser, *Biophysics of the cell surface*, Springer Berlin Heidelberg, 2012.

[127] R. Messina, *Electrostatics in soft matter*, Journal of Physics: Condensed Matter **21** (2009), 113102.

[128] D. N. Petsev and P. G. Vekilov, *Evidence for non-DLVO hydration interactions in solutions of the protein apoferritin*, Physical Review Letters **84** (2000), 1339.

[129] M. Boström, D. R. M. Williams, and B. W. Ninham, *Specific ion effects: Why DLVO theory fails for biology and colloid systems*, Physical Review Letters **87** (2001), 168103.

[130] M. R. Fries, *Protein adsorption controlled by multivalent ions*, PhD thesis, Universität Tübingen, 2022.

[131] O. Matsarskaia, *Multivalent ions for tuning the phase behaviour of protein solutions*, PhD thesis, Universität Tübingen, 2020.

[132] F. Zhang, S. Weggler, M. J. Ziller, L. Ianeselli, B. S. Heck, A. Hildebrandt, O. Kohlbacher, M. W. A. Skoda, R. M. J. Jacobs, and F. Schreiber, *Universality of protein reentrant condensation in solution induced by multivalent metal ions*, Proteins **78** (2010), 3450.

[133] F. Zhang, F. Roosen-Runge, A. Sauter, R. Roth, M. W. A. Skoda, R. Jacobs, M. Sztucki, and F. Schreiber, *The role of cluster formation and metastable liquid-liquid phase separation in protein crystallization*, Faraday Discussions **159** (2012), 313.

[134] L. Ianeselli, F. Zhang, M. W. A. Skoda, R. M. J. Jacobs, R. A. Martin, S. Callow, S. Prévost, and F. Schreiber, *Protein-protein interactions in ovalbumin solutions studied by small-angle scattering: effect of ionic strength and the chemical nature of cations*, The Journal of Physical Chemistry B **114** (2010), 3776.

[135] M. K. Braun, A. Sauter, O. Matsarskaia, M. Wolf, F. Roosen-Runge, M. Sztucki, R. Roth, F. Zhang, and F. Schreiber, *Reentrant phase behavior in protein solutions induced by multivalent salts: Strong effect of anions Cl^- versus NO_3^-*, The Journal of Physical Chemistry B **122** (2018), 11978.

[136] M. R. Fries, D. Stopper, M. K. Braun, A. Hinderhofer, F. Zhang, R. M. J. Jacobs, M. W. A. Skoda, H. Hansen-Goos, R. Roth, and F. Schreiber, *Multivalent-ion-activated protein adsorption reflecting bulk reentrant behavior*, Physical Review Letters **119** (2017), 228001.

[137] A. Bujacz, *Structures of bovine, equine and leporine serum albumin*, Acta Crystallographica D **68** (2012), 1278.

[138] K. A. Majorek, P. J. Porebski, A. Dayal, M. D. Zimmerman, K. Jablonska, A. J. Stewart, M. Chruszcz, and W. Minor, *Structural and immunologic characterization of bovine, horse, and rabbit serum albumins*, Molecular Immunology **52** (2012), 174.

[139] E. Mylonas and D. I. Svergun, *Accuracy of molecular mass determination of proteins in solution by small-angle X-ray scattering*, Journal of Applied Crystallography **40** (2007), s245.

[140] D.-M. Smilgies and E. Folta-Stogniew, *Molecular weight–gyration radius relation of globular proteins: a comparison of light scattering, small-angle X-ray scattering and structure-based data*, Journal of Applied Crystallography **48** (2015), 1604.

[141] J. M. Peula-Garcia, R. Hidaldo-Alvarez, and F. J. de las Nieves, *Protein co-adsorption on different polystyrene latexes: electrokinetic characterization and colloidal stability*, Colloid Polym. Sci. **275** (1997), 198.

[142] J. Cruse and R. Lewis, *Illustrated dictionary of immunology*, CRC Press, 2009.

[143] M. C. Linder, *Ceruloplasmin and other copper binding components of blood plasma and their functions: an update*, Metallomics **8** (2016), 887.

[144] F. C. Hay and O. M. Westwood, *Practical immunology*, Blackwell Science Ltd, 2002.

[145] K. Wilson and J. Walker (eds.), *Principles and techniques of biochemistry and molecular biology*, Cambridge University Press, 2009.

[146] M. R. Fries, N. F. Conzelmann, L. Günter, O. Matsarskaia, M. W. A. Skoda, R. M. J. Jacobs, F. Zhang, and F. Schreiber, *Bulk phase behavior vs interface adsorption: Specific multivalent cation and anion effects on BSA interactions*, Langmuir **37** (2021), 139.

[147] N. Begam, O. Matsarskaia, M. Sztucki, F. Zhang, and F. Schreiber, *Unification of lower and upper critical solution temperature phase behavior of globular protein solutions in the presence of multivalent cations*, Soft Matter **16** (2020), 2128.

[148] O. Matsarskaia, F. Roosen-Runge, G. Lotze, J. Möller, A. Mariani, F. Zhang, and F. Schreiber, *Tuning phase transitions of aqueous protein solutions by multivalent cations*, Physical Chemistry Chemical Physics **20** (2018), 27214.

[149] M. K. Braun, M. Wolf, O. Matsarskaia, S. Da Vela, F. Roosen-Runge, M. Sztucki, R. Roth, F. Zhang, and F. Schreiber, *Strong isotope effects on effective interactions and phase behavior in protein solutions in the presence of multivalent ions*, The Journal of Physical Chemistry B **121** (2017), 1731.

[150] F. Zhang, R. Roth, M. Wolf, F. Roosen-Runge, M. W. A. Skoda, R. M. J. Jacobs, M. Sztucki, and F. Schreiber, *Charge-controlled metastable liquid-liquid phase separation in protein solutions as a universal pathway towards crystallization*, Soft Matter **8** (2012), 1313.

[151] F. Roosen-Runge, F. Zhang, F. Schreiber, and R. Roth, *Ion-activated attractive patches as a mechanism for controlled protein interactions*, Scientific Reports **4** (2014), 7016.

[152] R. P. Sear, *Phase behavior of a simple model of globular proteins*, The Journal of Chemical Physics **111** (1999), 4800.

[153] N. Kern and D. Frenkel, *Fluid–fluid coexistence in colloidal systems with short-ranged strongly directional attraction*, The Journal of Chemical Physics **118** (2003), 9882.

[154] C. Gögelein, G. Nägele, R. Tuinier, T. Gibaud, A. Stradner, and P. Schurtenberger, *A simple patchy colloid model for the phase behavior of lysozyme dispersions*, The Journal of Chemical Physics **129** (2008), 085102.

[155] E. Bianchi, R. Blaak, and C. N. Likos, *Patchy colloids: state of the art and perspectives*, Physical Chemistry Chemical Physics **13** (2011), 6397.

[156] J. Als-Nielsen and D. McMorrow, *Elements of modern X-ray physics*, John Wiley & Sons, West Sussex, United Kingdom, 2011.

[157] P. Lindner and T. Zemb, *Neutrons, X-rays, and light: Scattering methods applied to soft condensed matter*, Elsevier North-Holland, 2002.

[158] S.-H. Chen and T.-L. Lin, *Methods of experimental physics*, Academic Press, London, 1987.

[159] D. Sivia, *Elementary scattering theory for X-ray and neutron users*, Oxford University Press, 2011.

[160] J. Rigden and E. Gordon, *The granularity of scattered optical maser light*, Proceedings of the IRE (1962), 2367–2368.

[161] K. F. Ludwig, *Comment on "speckle in the diffraction patterns of hendricks-teller and icosahedral glass models"*, Physical Review Letters **61** (1988), 1526.

[162] M. Sutton, S. G. J. Mochrie, T. Greytak, S. E. Nagler, L. E. Berman, G. A. Held, and G. B. Stephenson, *Observation of speckle by diffraction with coherent X-rays*, Nature **352** (1991), 608.

[163] J. W. Goodman, *Some fundamental properties of speckle*, Journal of the Optical Society of America **66** (1976), 1145.

[164] J. W. Goodman, *Statistical optics*, Wiley-Interscience, New York, 1985.

[165] M. Born, E. Wolf, A. B. Bhatia, P. C. Clemmow, D. Gabor, A. R. Stokes, A. M. Taylor, P. A. Wayman, and W. L. Wilcock, *Principles of optics: Electromagnetic theory of propagation, interference and diffraction of light*, Cambridge University Press, 1999.

[166] K. Pieper, A. Bergmann, R. Dengler, and C. Rockstuhl, *Visualizing and manipulating the spatial and temporal coherence of light with an adjustable light source in an undergraduate experiment*, European Journal of Physics **40** (2019), 055302.

[167] R. Pecora, *Doppler shifts in light scattering from pure liquids and polymer solutions*, The Journal of Chemical Physics **40** (1964), 1604.

[168] C. Phelps, *Dynamic light scattering, with application to chemistry, biology and physics*, Biochemical Education **5** (1977), 22.

[169] D. K. Carpenter, *Dynamic light scattering with applications to chemistry, biology, and physics*, Journal of Chemical Education **54** (1977), A430.

[170] E. R. Pike and J. B. Abbiss (eds.), *Light scattering and photon correlation spectroscopy*, Springer Dordrecht, 1997.

[171] G. Grübel, J. Als-Nielsen, D. Abernathy, D. Vignaud, S. Brauer, G. Stephenson, S. Mochrie, M. Sutton, I. Robinson, R. Fleming, R. Pindak, S. Dierker, and J. Legrand, *Scattering with Coherent X-rays*, ESRF Newsletter **20** (1994), 14.

[172] F. Lehmkühler, W. Roseker, and G. Grübel, *From femtoseconds to hours—measuring dynamics over 18 orders of magnitude with coherent x-rays*, Applied Sciences **11** (2021), 6179.

[173] F. Westermeier, B. Fischer, W. Roseker, G. Grübel, G. Nägele, and M. Heinen, *Structure and short-time dynamics in concentrated suspensions of charged colloids*, The Journal of Chemical Physics **137** (2012), 114504.

[174] S. B. Dierker, R. Pindak, R. M. Fleming, I. K. Robinson, and L. Berman, *X-ray photon correlation spectroscopy study of brownian motion of gold colloids in glycerol*, Physical Review Letters **75** (1995), 449.

[175] T. Thurn-Albrecht, W. Steffen, A. Patkowski, G. Meier, E. W. Fischer, G. Grübel, and D. L. Abernathy, *Photon correlation spectroscopy of colloidal palladium using a coherent X-ray beam*, Physical Review Letters **77** (1996), 5437.

[176] O. K. C. Tsui and S. G. J. Mochrie, *Dynamics of concentrated colloidal suspensions probed by X-raycorrelation spectroscopy*, Physical Review E **57** (1998), 2030.

[177] D. Pontoni, T. Narayanan, J.-M. Petit, G. Grübel, and D. Beysens, *Microstructure and dynamics near an attractive colloidal glass transition*, Physical Review Letters **90** (2003), 188301.

[178] J. Lal, D. Abernathy, L. Auvray, O. Diat, and G. Grübel, *Dynamics and correlations in magnetic colloidal systems studied by X-ray photon correlation spectroscopy*, The European Physical Journal E **4** (2001), 263.

[179] A. Fluerasu, A. Moussaïd, A. Madsen, and A. Schofield, *Slow dynamics and aging in colloidal gels studied by X-ray photon correlation spectroscopy*, Physical Review E **76** (2007), 010401.

[180] A. Robert, J. Wagner, T. Autenrieth, W. Härtl, and G. Grübel, *Coherent X-rays as a new probe for the investigation of the dynamics of opaque colloidal suspensions*, Journal of Magnetism and Magnetic Materials **289** (2005), 47.

[181] E. Wandersman, A. Duri, A. Robert, E. Dubois, V. Dupuis, and R. Perzynski, *Probing heterogeneous dynamics of a repulsive colloidal glass by time resolved X-ray correlation spectroscopy*, Journal of Physics: Condensed Matter **20** (2008), 155104.

[182] C. Caronna, Y. Chushkin, A. Madsen, and A. Cupane, *Dynamics of nanoparticles in a supercooled liquid*, Physical Review Letters **100** (2008), 055702.

[183] A. Robert, J. Wagner, W. Härtl, T. Autenrieth, and G. Grübel, *Dynamics in dense suspensions of charge-stabilized colloidal particles*, The European Physical Journal E **25** (2008), 77.

[184] E. M. Herzig, A. Robert, D. D. van 't Zand, L. Cipelletti, P. N. Pusey, and P. S. Clegg, *Dynamics of a colloid-stabilized cream*, Physical Review E **79** (2009), 011405.

[185] A. Duri, T. Autenrieth, L.-M. Stadler, O. Leupold, Y. Chushkin, G. Grübel, and C. Gutt, *Two-dimensional heterogeneous dynamics at the surface of a colloidal suspension*, Physical Review Letters **102** (2009), 145701.

[186] X. Lu, S. G. J. Mochrie, S. Narayanan, A. R. Sandy, and M. Sprung, *Temperature-dependent structural arrest of silica colloids in a water–lutidine binary mixture*, Soft Matter **6** (2010), 6160.

[187] B. Fischer, J. Wagner, C. Gutt, F. Westermeier, and G. Grübel, *Structure and dynamics of glassy charged colloids studied with coherent small angle X-ray scattering*, Journal of Physics: Conference Series **247** (2010), 012026.

[188] M. Sikorski, A. R. Sandy, and S. Narayanan, *Depletion-induced structure and dynamics in bimodal colloidal suspensions*, Physical Review Letters **106** (2011), 188301.

[189] M. Spannuth, S. G. J. Mochrie, S. S. L. Peppin, and J. S. Wettlaufer, *Dynamics of colloidal particles in ice*, The Journal of Chemical Physics **135** (2011), 224706.

[190] H. Guo, S. Ramakrishnan, J. L. Harden, and R. L. Leheny, *Gel formation and aging in weakly attractive nanocolloid suspensions at intermediate concentrations*, The Journal of Chemical Physics **135** (2011), 154903.

[191] D. Orsi, A. Fluerasu, A. Moussaïd, F. Zontone, L. Cristofolini, and A. Madsen, *Dynamics in dense hard-sphere colloidal suspensions*, Physical Review E **85** (2012), 011402.

[192] P. Kwaśniewski, A. Fluerasu, and A. Madsen, *Anomalous dynamics at the hard-sphere glass transition*, Soft Matter **10** (2014), 8698.

[193] R. Angelini, A. Madsen, A. Fluerasu, G. Ruocco, and B. Ruzicka, *Aging behavior of the localization length in a colloidal glass*, Colloids and Surfaces A: Physicochemical and Engineering Aspects **460** (2014), 118.

[194] R. Angelini and B. Ruzicka, *Non-diffusive dynamics in a colloidal glass: Aging versus rejuvenation*, Colloids and Surfaces A: Physicochemical and Engineering Aspects **483** (2015), 316.

[195] W. Liu, B. Zheng, X. Yin, X. Yu, Y. Zhang, L. Wiegart, A. Fluerasu, B. L. Armstrong, G. M. Veith, and S. R. Bhatia, *XPCS microrheology and rheology of sterically stabilized nanoparticle dispersions in aprotic solvents*, ACS Applied Materials & Interfaces **13** (2021), 14267.

[196] A. Madsen, J. Als-Nielsen, and G. Grübel, *Viscosity of a liquid crystal near the nematic–smectic a phase transition*, Physical Review Letters **90** (2003), 085701.

[197] D. D. van 't Zand, Y. Chushkin, L. Belkoura, C. V. Lobo, R. Strey, K. Lyakhova, and P. S. Clegg, *Anisotropic dynamics of the tenuous gel in a liquid crystal–nanoparticle composite*, Soft Matter **8** (2012), 4062.

[198] Z. H. Cai, B. Lai, W. B. Yun, I. McNulty, K. G. Huang, and T. P. Russell, *Observation of X-ray speckle by coherent scattering at grazing incidence*, Physical Review Letters **73** (1994), 82.

[199] S. G. J. Mochrie, A. M. Mayes, A. R. Sandy, M. Sutton, S. Brauer, G. B. Stephenson, D. L. Abernathy, and G. Grübel, *Dynamics of block copolymer micelles revealed by X-ray intensity fluctuation spectroscopy*, Physical Review Letters **78** (1997), 1275.

[200] H. Kim, A. Rühm, L. B. Lurio, J. K. Basu, J. Lal, D. Lumma, S. G. J. Mochrie, and S. K. Sinha, *Surface dynamics of polymer films*, Physical Review Letters **90** (2003), 068302.

[201] P. Falus, M. A. Borthwick, and S. G. J. Mochrie, *Fluctuation dynamics of block copolymer vesicles*, Physical Review Letters **94** (2005), 016105.

[202] S. Narayanan, D. R. Lee, A. Hagman, X. Li, and J. Wang, *Particle dynamics in polymer-metal nanocomposite thin films on nanometer-length scales*, Physical Review Letters **98** (2007), 185506.

[203] S. Srivastava, A. K. Kandar, J. K. Basu, M. K. Mukhopadhyay, L. B. Lurio, S. Narayanan, and S. K. Sinha, *Complex dynamics in polymer nanocomposites*, Physical Review E **79** (2009), 021408.

[204] A. K. Kandar, S. Srivastava, J. K. Basu, M. K. Mukhopadhyay, S. Seifert, and S. Narayanan, *Unusual dynamical arrest in polymer grafted nanoparticles*, The Journal of Chemical Physics **130** (2009), 121102.

[205] H. Guo, G. Bourret, M. K. Corbierre, S. Rucareanu, R. B. Lennox, K. Laaziri, L. Piche, M. Sutton, J. L. Harden, and R. L. Leheny, *Nanoparticle motion within glassy polymer melts*, Physical Review Letters **102** (2009), 075702.

[206] O. Czakkel and A. Madsen, *Evolution of dynamics and structure during formation of a cross-linked polymer gel*, EPL (Europhysics Letters) **95** (2011), 28001.

[207] H. Guo, G. Bourret, R. B. Lennox, M. Sutton, J. L. Harden, and R. L. Leheny, *Entanglement-controlled subdiffusion of nanoparticles within concentrated polymer solutions*, Physical Review Letters **109** (2012), 055901.

[208] R. Hernández, A. Nogales, M. Sprung, C. Mijangos, and T. A. Ezquerra, *Slow dynamics of nanocomposite polymer aerogels as revealed by X-ray photocorrelation spectroscopy (XPCS)*, The Journal of Chemical Physics **140** (2014), 024909.

[209] H. Conrad, F. Lehmkühler, B. Fischer, F. Westermeier, M. A. Schroer, Y. Chushkin, C. Gutt, M. Sprung, and G. Grübel, *Correlated heterogeneous dynamics in glass-forming polymers*, Physical Review E **91** (2015), 042309.

[210] A. Nogales and A. Fluerasu, *X ray photon correlation spectroscopy for the study of polymer dynamics*, European Polymer Journal **81** (2016), 494.

[211] M. Leitner, B. Sepiol, L.-M. Stadler, and B. Pfau, *Time-resolved study of the crystallization dynamics in a metallic glass*, Physical Review B **86** (2012), 064202.

[212] S. O. Hruszkewycz, M. Sutton, P. H. Fuoss, B. Adams, S. Rosenkranz, K. F. Ludwig, W. Roseker, D. Fritz, M. Cammarata, D. Zhu, S. Lee, H. Lemke, C. Gutt, A. Robert, G. Grübel, and G. B. Stephenson, *High contrast X-ray speckle from atomic-scale order in liquids and glasses*, Physical Review Letters **109** (2012), 185502.

[213] B. Ruta, Y. Chushkin, G. Monaco, L. Cipelletti, E. Pineda, P. Bruna, V. M. Giordano, and M. Gonzalez-Silveira, *Atomic-scale relaxation dynamics and aging in a metallic glass probed by X-ray photon correlation spectroscopy*, Physical Review Letters **109** (2012), 165701.

[214] B. Ruta, G. Baldi, G. Monaco, and Y. Chushkin, *Compressed correlation functions and fast aging dynamics in metallic glasses*, The Journal of Chemical Physics **138** (2013).

[215] O. G. Shpyrko, E. D. Isaacs, J. M. Logan, Y. Feng, G. Aeppli, R. Jaramillo, H. C. Kim, T. F. Rosenbaum, P. Zschack, M. Sprung, S. Narayanan, and A. R. Sandy, *Direct measurement of antiferromagnetic domain fluctuations*, Nature **447** (2007), 68.

[216] S.-W. Chen, H. Guo, K. A. Seu, K. Dumesnil, S. Roy, and S. K. Sinha, *Jamming behavior of domains in a spiral antiferromagnetic system*, Physical Review Letters **110** (2013), 217201.

[217] Q. Zhang, E. M. Dufresne, P. Chen, J. Park, M. P. Cosgriff, M. Yusuf, Y. Dong, D. D. Fong, H. Zhou, Z. Cai, R. J. Harder, S. J. Callori, M. Dawber, P. G. Evans, and A. R. Sandy, *Thermal fluctuations of ferroelectric nanodomains in a ferroelectric-dielectric* $PbTiO_3/SrTiO_3$ *superlattice*, Physical Review Letters **118** (2017), 097601.

[218] E. B. Trigg, L. Wiegart, A. Fluerasu, and H. Koerner, *Dynamics of polymerization and gelation in epoxy nanocomposites via X-ray photon correlation spectroscopy*, Macromolecules **54** (2021), 6575.

[219] F. Perakis, K. Amann-Winkel, F. Lehmkühler, M. Sprung, D. Mariedahl, J. A. Sellberg, H. Pathak, A. Späh, F. Cavalca, D. Schlesinger, A. Ricci, A. Jain, B. Massani, F. Aubree, C. J. Benmore, T. Loerting, G. Grübel, L. G. M. Pettersson, and A. Nilsson, *Diffusive dynamics during the high-to-low density transition in amorphous ice*, Proceedings of the National Academy of Sciences **114** (2017), 8193.

[220] A. Ragulskaya, N. Begam, A. Girelli, H. Rahmann, M. Reiser, F. Westermeier, M. Sprung, F. Zhang, C. Gutt, and F. Schreiber, *Interplay between kinetics and dynamics of liquid-liquid phase separation in a protein solution revealed by coherent X-ray spectroscopy*, The Journal of Physical Chemistry Letters **31** (2021), 7085.

[221] F. Lehmkühler, F. Dallari, A. Jain, M. Sikorski, J. Möller, L. Frenzel, I. Lokteva, G. Mills, M. Walther, H. Sinn, F. Schulz, M. Dartsch, V. Markmann, R. Bean, Y. Kim, P. Vagovic, A. Madsen, A. P. Mancuso, and G. Grübel, *Emergence of anomalous dynamics in soft matter probed at the european XFEL*, Proceedings of the National Academy of Sciences **117** (2020), 24110.

[222] N. Begam, A. Ragulskaya, A. Girelli, H. Rahmann, S. Chandran, F. Westermeier, M. Reiser, M. Sprung, F. Zhang, C. Gutt, and F. Schreiber, *Kinetics of network formation and heterogeneous dynamics of an egg white gel revealed by coherent X-ray scattering*, Physical Review Letters **126** (2021), 098001.

[223] A. Girelli, H. Rahmann, N. Begam, A. Ragulskaya, M. Reiser, S. Chandran, F. Westermeier, M. Sprung, F. Zhang, C. Gutt, and F. Schreiber, *Microscopic dynamics of liquid-liquid phase separation and domain coarsening in a protein solution revealed by X-ray photon correlation spectroscopy*, Physical Review Letters **126** (2021), 138004.

[224] J. Möller, M. Reiser, J. Hallmann, U. Boesenberg, A. Zozulya, H. Rahmann, A.-L. Becker, F. Westermeier, T. Zinn, M. Sprung, T. Narayanan, C. Gutt, and A. Madsen, *Using low dose X-rayspeckle visibility spectroscopy to study dynamics of soft matter samples*, New Journal of Physics **23** (2021), 093041.

[225] G. Grübel, A. Madsen, and A. Robert, *X-ray photon correlation spectroscopy (XPCS)*, Springer Netherlands, Dordrecht, 2008, 953.

[226] M. Sutton, *A review of X-ray intensity fluctuation spectroscopy*, Comptes Rendus Physique **9** (2008), 657.

[227] A. Madsen, A. Fluerasu, and B. Ruta, *Structural dynamics of materials probed by X-ray photon correlation spectroscopy*, Synchrotron Light Sources and Free-Electron Lasers, Springer International Publishing, 2016, 1617.

[228] D. Ferreira, R. Bachelard, W. Guerin, R. Kaiser, and M. Fouché, *Connecting field and intensity correlations: The Siegert relation and how to test it*, American Journal of Physics **88** (2020), 831.

[229] D. Sheyfer, *Structure and dynamics of glass-forming fluids*, PhD thesis, Fakultät für Mathematik, Informatik und Naturwissenschaften Fachbereich Physik der Universität Hamburg (Germany), 2017.

[230] M. D. Ediger, *Spatially heterogeneous dynamics in supercooled liquids*, Annual Review of Physical Chemistry **51** (2000), 99.

[231] A. Madsen, R. L. Leheny, H. Guo, M. Sprung, and O. Czakkel, *Beyond simple exponential correlation functions and equilibrium dynamics in X-ray photon correlation spectroscopy*, New Journal of Physics **12** (2010), 055001.

[232] O. Bikondoa, *On the use of two-time correlation functions for X-ray photon correlation spectroscopy data analysis*, Journal of Applied Crystallography **50** (2017), 357.

[233] M. Sutton, K. Laaziri, F. Livet, and F. Bley, *Using coherence to measure two-time correlation functions*, Optics Express **11** (2003), 2268.

[234] G. Brown, P. A. Rikvold, M. Sutton, and M. Grant, *Speckle from phase-ordering systems*, Physical Review E **56** (1997), 6601.

[235] P. N. Pusey, *Statistical properties of scattered radiation*, Photon Correlation Spectroscopy and Velocimetry, Springer US, 1977, 45–141.

[236] J. W. Goodman, *Speckle phenomena in optics: Theory and applications, second edition*, SPIE, January 2020.

[237] R. Loudon, *The quantum theory of light*, Oxford science publications, Clarendon Press, Oxford University Press, Oxford : New York, 1983.

[238] A. Malik, A. R. Sandy, L. B. Lurio, G. B. Stephenson, S. G. J. Mochrie, I. McNulty, and M. Sutton, *Coherent X-raystudy of fluctuations during domain coarsening*, Physical Review Letters **81** (1998), 5832.

[239] G. Brown, P. A. Rikvold, M. Sutton, and M. Grant, *Evolution of speckle during spinodal decomposition*, Physical Review E **60** (1999), 5151.

[240] F. Livet, F. Bley, R. Caudron, E. Geissler, D. Abernathy, C. Detlefs, G. Grübel, and M. Sutton, *Kinetic evolution of unmixing in an AlLi alloy using X-ray intensity fluctuation spectroscopy*, Physical Review E **63** (2001), 036108.

[241] A. Fluerasu, M. Sutton, and E. M. Dufresne, *X-ray intensity fluctuation spectroscopy studies on phase-ordering systems*, Physical Review Letters **94** (2005), 055501.

[242] L. Müller, M. Waldorf, C. Gutt, G. Grübel, A. Madsen, T. R. Finlayson, and U. Klemradt, *Slow aging dynamics and avalanches in a gold-cadmium alloy investigated by X-ray photon correlation spectroscopy*, Physical Review Letters **107** (2011), 105701.

[243] D. Orsi, L. Cristofolini, M. P. Fontana, E. Pontecorvo, C. Caronna, A. Fluerasu, F. Zontone, and A. Madsen, *Slow dynamics in an azopolymer molecular layer studied by X-ray photon correlation spectroscopy*, Physical Review E **82** (2010), 031804.

[244] O. Bikondoa, D. Carbone, V. Chamard, and T. H. Metzger, *Ion beam sputtered surface dynamics investigated with two-time correlation functions: a model study*, Journal of Physics: Condensed Matter **24** (2012), 445006.

[245] Q. Zhang, E. M. Dufresne, Y. Nakaye, P. R. Jemian, T. Sakumura, Y. Sakuma, J. D. Ferrara, P. Maj, A. Hassan, D. Bahadur, S. Ramakrishnan, F. Khan, S. Veseli, A. R. Sandy, N. Schwarz, and S. Narayanan, *20μs-resolved high-throughput X-ray Photon correlation spectroscopy on a 500k pixel detector enabled by data-management workflow*, Journal of Synchrotron Radiation **28** (2021), 259.

[246] P. Falus, L. Lurio, and S. Mochrie, *Optimizing the signal-to-noise ratio for X-ray Photon correlation spectroscopy*, Journal of Synchrotron Radiation **13** (2006), 253.

[247] J. H. Hubbell, *Photon cross sections, attenuation coefficients, and energy absorption coefficients from 10 keV to 100 GeV*, Tech. report, 1969.

[248] S. Seltzer, *XCOM-photon cross sections database, NIST standard reference database 8*, http://www.nist.gov/pml/data/xcom/index.cfm, 1987.

[249] R. Henderson, *The potential and limitations of neutrons, electrons and x-rays for atomic resolution microscopy of unstained biological molecules*, Quarterly Reviews of Biophysics **28** (1995), 171.

[250] J. M. Holton, *A beginner's guide to radiation damage*, Journal of Synchrotron Radiation **16** (2009), 133.

[251] H. Liu and W. Lee, *The XFEL protein crystallography: Developments and perspectives*, International Journal of Molecular Sciences **20** (2019), 3421.

[252] H. N. Chapman, A. Barty, M. J. Bogan, S. Boutet, M. Frank, S. P. Hau-Riege, S. Marchesini, B. W. Woods, S. Bajt, W. H. Benner, R. A. London, E. Plönjes, M. Kuhlmann, R. Treusch, S. Düsterer, T. Tschentscher, J. R. Schneider, E. Spiller, T. Möller, C. Bostedt, M. Hoener, D. A. Shapiro, K. O. Hodgson, D. van der Spoel, F. Burmeister, M. Bergh, C. Caleman, G. Huldt, M. M. Seibert, F. R. N. C. Maia, R. W. Lee, A. Szöke, N. Timneanu, and J. Hajdu, *Femtosecond diffractive imaging with a soft-x-ray free-electron laser*, Nature Physics **2** (2006), 839.

[253] S. P. Meisburger, M. Warkentin, H. Chen, J. B. Hopkins, R. E. Gillilan, L. Pollack, and R. E. Thorne, *Breaking the radiation damage limit with cryo-SAXS*, Biophysical Journal **104** (2013), 227.

[254] T. Peters, *All about albumin: biochemistry, genetics, and medical applications*, Academic Press San Diego, CA, 1996.

[255] Y. Zhang and P. S. Cremer, *Interactions between macromolecules and ions: the hofmeister series*, Current Opinion in Chemical Biology **10** (2006), 658.

[256] M. L. Ferrer, R. Duchowicz, B. Carrasco, J. G. de la Torre, and A. U. Acuna, *The conformation of serum albumin in solution: A combined phosphorescence depolarization-hydrodynamic modeling study*, Biophys. J. **80** (2001), 2422.

[257] V. Lin and J. Koenig, *Raman studies of bovine serum albumin*, Biopolymers: Original Research on Biomolecules **15** (1976), 203.

[258] M. Grimaldo, F. Roosen-Runge, M. Hennig, F. Zanini, F. Zhang, N. Jalarvo, M. Zamponi, F. Schreiber, and T. Seydel, *Hierarchical molecular dynamics of bovine serum albumin in concentrated aqueous solution below and above thermal denaturation*, Physical Chemistry Chemical Physics **17** (2015), 4645.

[259] M. Grimaldo, F. Roosen-Runge, M. Hennig, F. Zanini, F. Zhang, M. Zamponi, N. Jalarvo, F. Schreiber, and T. Seydel, *Salt-induced universal slowing down of the short-time self-diffusion of a globular protein in aqueous solution*, The Journal of Physical Chemistry Letters **6** (2015), 2577.

[260] DESY, *P10 - Coherence Applications Beamline*, `https://photon-science.desy.de/facilities/petra_iii/beamlines/p10_coherence_applications/index_eng.html`.

[261] ESRF, *Id02 - time-resolved ultra small-angle X-ray scattering beamline*, `https://www.esrf.fr/home/UsersAndScience/Experiments/CBS/ID02.html`.

[262] T. Zinn, A. Homs, L. Sharpnack, G. Tinti, E. Fröjdh, P.-A. Douissard, M. Kocsis, J. Möller, Y. Chushkin, and T. Narayanan, *Ultra-small-angle X-ray photon correlation spectroscopy using the Eiger detector*, Journal of Synchrotron Radiation **25** (2018), 1753.

[263] M. Hondele, S. Heinrich, P. De Los Rios, and K. Weis, *Membraneless organelles: phasing out of equilibrium*, Emerging Topics in Life Sciences **4** (2020), 343.

[264] H. Furukawa, *Dynamics-scaling theory for phase-separating unmixing mixtures: Growth rates of droplets and scaling properties of autocorrelation functions*, Physica A: Statistical Mechanics and its Applications **123** (1984), 497.

[265] A. Cumming, P. Wiltzius, F. S. Bates, and J. H. Rosedale, *Light-scattering experiments on phase-separation dynamics in binary fluid mixtures*, Physical Review A **45** (1992), 885.

[266] M. Grimaldo, F. Roosen-Runge, F. Zhang, F. Schreiber, and T. Seydel, *Dynamics of proteins in solution*, Quarterly Reviews of Biophysics **52** (2019), e7.

[267] S. K. Sinha, M. Tolan, and A. Gibaud, *Effects of partial coherence on the scattering of X-rays by matter*, Physical Review B **57** (1998), 2740.

[268] A. Robert, E. Wandersman, E. Dubois, V. Dupuis, and R. Perzynski, *Glassy dynamics and aging in a dense ferrofluid*, Europhysics Letters **75** (2006), 764.

[269] S. Manley, H. M. Wyss, K. Miyazaki, J. C. Conrad, V. Trappe, L. J. Kaufman, D. R. Reichman, and D. A. Weitz, *Glasslike arrest in spinodal decomposition as a route to colloidal gelation*, Physical Review Letters **95** (2005), 238302.

[270] K. Binder, *Spinodal decomposition*, Systems Far from Equilibrium, Springer Berlin Heidelberg, 1980, 76.

[271] S. Schramm, T. Blochowicz, E. Gouirand, R. Wipf, B. Stühn, and Y. Chushkin, *Concentration fluctuations in a binary glass former investigated by X-ray photon correlation spectroscopy*, The Journal of Chemical Physics **132** (2010), 224505.

[272] D. Sappelt and J. Jäckle, *Computer simulation study of phase separation in a binary mixture with a glass-forming component*, Physica A: Statistical Mechanics and its Applications **240** (1997), 453.

[273] F. Wang, P. Altschuh, L. Ratke, H. Zhang, M. Selzer, and B. Nestler, *Progress report on phase separation in polymer solutions*, Advanced Materials **31** (2019), 1806733.

[274] H. Cook, *Brownian motion in spinodal decomposition*, Acta Metallurgica **18** (1970), 297.

[275] A. Ragulskaya, V. Starostin, N. Begam, A. Girelli, H. Rahmann, M. Reiser, F. Westermeier, M. Sprung, F. Zhang, C. Gutt, and F. Schreiber, *Reverse-engineering method for XPCS studies of non-equilibrium dynamics*, IUCrJ **(accepted)** (2022).

[276] M. Riedel, F. Wolf, D. Kranzlmüller, A. Streit, and T. Lippert, *Research advances by using interoperable e-science infrastructures*, Cluster Computing **12** (2009), 357.

[277] N. H. Sabelli, *Complexity, technology, science, and education*, Journal of the Learning Sciences **15** (2006), 5.

[278] Y. Wang, A. Lomakin, R. F. Latypov, J. P. Laubach, T. Hideshima, P. G. Richardson, N. C. Munshi, K. C. Anderson, and G. B. Benedek, *Phase transitions in human IgG solutions*, The Journal of Chemical Physics **139** (2013), 121904.

[279] J. Verwohlt, M. Reiser, L. Randolph, A. Matic, L. A. Medina, A. Madsen, M. Sprung, A. Zozulya, and C. Gutt, *Low dose X-ray speckle visibility spectroscopy reveals nanoscale dynamics in radiation sensitive ionic liquids*, Physical Review Letters **120** (2018), 168001.

[280] L. B. Lurio, G. M. Thurston, Q. Zhang, S. Narayanan, and E. M. Dufresne, *Use of continuous sample translation to reduce radiation damage for XPCS studies of protein diffusion*, Journal of Synchrotron Radiation **28** (2021), 490.

[281] R. L. Headrick, J. G. Ulbrandt, P. Myint, J. Wan, Y. Li, A. Fluerasu, Y. Zhang, L. Wiegart, and K. F. Ludwig, *Coherent X-ray measurement of step-flow propagation during growth on polycrystalline thin film surfaces*, Nature Communications **10** (2019), 2638.

[282] F. Ehrburger-Dolle, I. Morfin, F. Bley, F. Livet, G. Heinrich, Y. Chushkin, and M. Sutton, *Anisotropic and heterogeneous dynamics in stretched elastomer nanocomposites*, Soft Matter **15** (2019), 3796.

[283] G. Ju, D. Xu, M. J. Highland, C. Thompson, H. Zhou, J. A. Eastman, P. H. Fuoss, P. Zapol, H. Kim, and G. B. Stephenson, *Coherent X-ray spectroscopy reveals the persistence of island arrangements during layer-by-layer growth*, Nature Physics **15** (2019), 589.

[284] E. Eilam, *Reversing: Secrets of reverse engineering*, John Wiley & Sons, Inc., USA, 2005.

[285] F. Buonamici, M. Carfagni, R. Furferi, L. Governi, A. Lapini, and Y. Volpe, *Reverse engineering of mechanical parts: A template-based approach*, Journal of Computational Design and Engineering **5** (2018), 145.

[286] N. Asadizanjani, M. Tehranipoor, and D. Forte, *PCB reverse engineering using nondestructive X-raytomography and advanced image processing*, IEEE Transactions on Components, Packaging and Manufacturing Technology **99** (2017), 1.

[287] M. Dijkstra and E. Luijten, *From predictive modelling to machine learning and reverse engineering of colloidal self-assembly*, Nature Materials **20** (2021), 762.

[288] Z. M. Sherman, M. P. Howard, B. A. Lindquist, R. B. Jadrich, and T. M. Truskett, *Inverse methods for design of soft materials*, The Journal of Chemical Physics **152** (2020), 140902.

[289] A. L. Ferguson, *Machine learning and data science in soft materials engineering*, Journal of Physics: Condensed Matter **30** (2017), 043002.

[290] S. Alberti and D. Dormann, *Liquid–liquid phase separation in disease*, Annual Review of Genetics **53** (2019), 171.

[291] R. C. Desai and R. Kapral, *Dynamics of self-organized and self-assembled structures*, Cambridge University Press, 2010.

[292] J. Midya, S. Majumder, and S. K. Das, *Dimensionality dependence of aging in kinetics of diffusive phase separation: Behavior of order-parameter autocorrelation*, Physical Review E **92** (2015), 022124.

[293] R. Toral, A. Chakrabarti, and J. D. Gunton, *Large scale simulations of the two-dimensional cahn-hilliard model*, Physica A: Statistical Mechanics and its Applications **213** (1995), 41.

[294] H. Guo, S. Ramakrishnan, J. L. Harden, and R. L. Leheny, *Connecting nanoscale motion and rheology of gel-forming colloidal suspensions*, Physical Review E **81** (2010), 050401.

[295] A. Madsen, A. Fluerasu, and B. Ruta, *Structural dynamics of materials probed by X-ray photon correlation spectroscopy*, Springer International Publishing, 2018, 1.

[296] I. Robinson, C. Kenney-Benson, and I. Vartanyants, *Sources of decoherence in beamline optics*, Physica B: Condensed Matter **336** (2003), 56.

[297] V. Starostin and A. Ragulskaya, *Particle simulation with correlation maps for reverse engineering*, https://github.com/StarostinV/particle_simulations.

[298] W. Jo, F. Westermeier, R. Rysov, O. Leupold, F. Schulz, S. Tober, V. Markmann, M. Sprung, A. Ricci, T. Laurus, A. Aschkan, A. Klyuev, U. Trunk,

H. Graafsma, G. Grübel, and W. Roseker, *Nanosecond X-ray Photon correlation spectroscopy using pulse time structure of a storage-ring source*, IUCrJ **8** (2021), 124.

[299] F. Perakis and C. Gutt, *Towards molecular movies with X-ray photon correlation spectroscopy*, Physical Chemistry Chemical Physics **22** (2020), 19443.

[300] A. Fluerasu, P. Kwasniewski, C. Caronna, F. Destremaut, J.-B. Salmon, and A. Madsen, *Dynamics and rheology under continuous shear flow studied by X-ray photon correlation spectroscopy*, New Journal of Physics **12** (2010), 035023.

[301] Dior, *Dior diorshow 5 couleurs designer eyeshadow palette 208 navy design*, https://www.dior.com/en_hr/products/beauty-Y0148140-5-couleurs-designer-the-makeup-artist-tutorial-palette.

[302] Y. Wu, H. Skrdla, T. Lookman, and S. Chen, *Spinodal decomposition in binary fluids under shear flow*, Physica A: Statistical Mechanics and its Applications **239** (1997), 428.

[303] J. K. Dhont, *Chapter 9 - phase separation kinetics*, An Introduction to Dynamics of Colloids, Studies in Interface Science, Elsevier, 1996, 559.

[304] I. Zhang, C. P. Royall, M. A. Faers, and P. Bartlett, *Phase separation dynamics in colloid–polymer mixtures: the effect of interaction range*, Soft Matter **9** (2013), 2076.

[305] J. Sabin, A. E. Bailey, and B. J. Frisken, *Exploring the dynamics of phase separation in colloid–polymer mixtures with long range attraction*, Soft matter **12** (2016), 5325.

[306] J. Conrad, H. Wyss, V. Trappe, S. Manley, K. Miyazaki, L. Kaufman, A. Schofield, D. Reichman, and D. Weitz, *Arrested fluid-fluid phase separation in depletion systems: Implications of the characteristic length on gel formation and rheology*, Journal of Rheology **54** (2010), 421.

[307] A. Grishaev, *Sample preparation, data collection, and preliminary data analysis in biomolecular solution X-ray scattering*, Current Protocols in Protein Science **70** (2012), 17.14.1.